uc3m | Universidad Carlos III de Madrid

University Degree in Aerospace Engineering

2024-2025

Bachelor Thesis

"Fluid Model Analysis of Plasma Flows in Magnetic Arch for Electrodeless Plasma Propulsion Systems"

Manuel Cortés Hernán

Mario Merino Martínez

Madrid, June 2025

SUMMARY

Electrodeless Plasma Thrusters (EPTs) promise long-lived propulsion for deep space missions, yet their current design still requires of further advancements to optimize operational parameters. Magnetic Arch (MA) field topologies, generated by clustering EPTs in pairs, offer an opportunity to reduce plume divergence and cancel dipole moment, thus contributing to increased thrust and efficiency values. This work delivers a two-fluid simulation of plasma expansion in MAs relying on finite volume methods in a FEniCS based code POSETS-v2, an update from the existing POSETS. POSETS-v2 enables full thermodynamic modeling of ions and improved convergence properties by incorporating Discontinuous Galerkin numerical integration procedures.

An initial cold-ion approximation is simulated to outline arising variations from previous literature neglecting ions thermal energy, hence properly managing energetic discontinuities in the downstream expansion. POSETS-v2 is then used to perform targeted parametric studies. Firstly, the influence of the electron polytropic index, $\gamma_e = 1.01, 1.2, 5/3$, revealing a collimation mechanism over larger γ_e values, which result in detrimental magnetic drag in the far region. Secondly, a sweep of the initial ion temperature $T_{i0} = 0.1, 1, 3, 10$ under initial force balance of the ambipolar electric field ϕ, which show a rise in M_i accompanied by an overall effective thrust decrease due to magnetic drag. Lastly, a series of simulations compare open and closed MA topologies, quantifying plume collimation, M_i and effective thrust generation.

Overall, the project advances the physical understanding of MA-based EPTs, paving the way for efficient plasma-based space propulsion systems that enable deep space exploration.

Keywords: Electric Propulsion, Electrodeless Plasma Thrusters, Magnetic Arch, Ion Thermodynamics, Deep Space Propulsion

DEDICATION

I could not finish this project without thanking all those who have accompanied me along the way. And despite being one of the first sections of the work, I intend to use this space of creative freedom to conclude. To conclude not only this Bachelor Thesis in plasma propulsion, but the four years of academic and personal growth that I leave behind. I look back and see an excited child that was eager to start Aerospace Engineering, with the dream of reaching space. And although that excitement was sometimes obscured by the hard challenges I faced, it now shines as in the first day. That emotion and eagerness to learn that pushed me four years ago into this adventure, and that has lifted me up from the falls, encourages me now to start a new stage. But this section is not to talk about me, but about you, those of you who, one way or another, have accompanied me or have passed, even briefly, through my life these four years.

Thank you Guille, Miguel, Guille, Jesús, Pedro and Víctor; Futbolineros, thank you for so much. Thank you Alba, Pablo, Natalia and Juan, for being indispensable travel companions in this career. Thank you Cony, Nacho, María, Elena, Irene, María and Alejandro; Georgia Tech would not have been the same without you.

Thanks to all I do not mention here but who have accompanied me these years and with whom I have forged essential friendships in my life. I remember all of you, thank you.

Thank you Prof. Mario Merino, you have been a fundamental guide and leader towards the success of this work. You are a true a reference of what a researcher should be: helpful, sincere and professional. I could not be more grateful to have you as a tutor.

I want to close this section by thanking the fundamental pillar of everything I have achieved, not only of this work but also of who I am, my family. I can't help but get emotional when I think of the unconditional support you give me constantly, you are the most important people in my life, thank you for accompanying me in succes and failure, in laughter and tears, for being who you are and for loving me as you do. I also remember abuela Modes, because I know you would be proud of your grandson, and with that I am happy. Thank you Mamá, Papá, María y abuela, because this would not have been the same without you, I dedicate you this project and all the ones that follow.

Thanks, again, to all of you.

CONTENTS

1. INTRODUCTION 1
1.1. Motivation and State of the Art. Electrodeless Plasma Propulsion 1
1.1.1. EPTs Limitations 3
1.1.2. Magnetic Arch (MA) Field Configuration 3
1.1.3. Magnetic Arch Thruster (MAT) 6
1.2. Objectives of this Work 6
1.3. Project Outline 7
1.4. Acknowledgments 8
2. PLASMA MODEL 9
2.1. Plasma Model Assumptions 9
2.2. Magnetic Field Model for MA 11
2.3. General Plasma Equations 12
2.4. Electron Model 13
2.5. Ion Model 16
2.6. Coupled Ion-Electron Plasma Model 17
3. NUMERICAL INTEGRATION 19
3.1. Finite Volume Method 20
3.2. Numerical Discretization. Discontinuous Galerkin 21
3.3. Numerical Flux Function. Local Lax-Friedrichs 22
3.4. Boundary Conditions 23
3.5. Time Integration 23
3.6. POSETS-v2: Plume SOlver for Electrodeless Thruster Systems - Version 2 . . 25
3.7. POSETS-v2 Code Verification 26
4. LOW ION TEMPERATURE MA EXPANSION SIMULATION 28
4.1. Description of the Simulation and Boundary Conditions 28
4.2. Plasma Expansion and Acceleration 32
4.3. Ion Magnetization Strength, Plasma Detachment and in-plane Electron Current 35

4.4. Ion and Electron Thermodynamics 39
4.4.1. Electron Polytropic Index γ_e Influence 43
4.5. Local Thrust and Plume Efficiency 45
5. ION TEMPERATURE PARAMETRIC ANALYSIS ON MA EXPANSION . . . 52
5.1. Description of the Simulation and Boundary Conditions 52
5.2. Results and Discussion 54
6. MAGNETIC FIELD GENERATORS ANALYSIS ON MA EXPANSION 61
6.1. Description of the Simulation and Boundary Conditions 61
6.2. Results and Discussion 62
7. FUTURE WORK AND CONCLUSION 67
7.1. Future Outlook 67
7.2. Conclusions 69
8. LEGAL FRAMEWORK AND SOCIO-ECONOMIC IMPACT 71
8.1. Legal Framework 71
8.2. Socio-Economic Impact 71
8.2.1. Project Budget 72
BIBLIOGRAPHY 73

LIST OF FIGURES

1.1 Helicon Plasma Thruster schematic and prototype. 2

1.2 Magnetic field topology on diverse Magnetic Arch configurations. 5

1.3 Magnetic Arch Thruster (MAT) concept art and dual-source cluster in operation. 6

3.1 Numerical integrals for conserved properties along control volume: mass, momentum and ion energy. 26

4.1 Applied magnetic field (a) and non-uniform simulation mesh (b). 29

4.2 Weakly imposed boundary conditions n (a), j_{zi} (b), j_{zi} (c) and $\hat{E}_i$ (d) . . . 30

4.3 Dimensionless H_e function (a) and $\partial H_e/\partial\psi$ (b). 32

4.4 Dimensionless plasma density n (a), electrostatic potential ϕ (b), in-plane ion macroscopic flow velocity $\tilde{\mathbf{u}}_i$ (c) and in-plane ion Mach number M_i (d). 33

4.5 Dimensionless plasma density n (a), electrostatic potential ϕ (b), in-plane ion macroscopic flow velocity $\tilde{\mathbf{u}}_i$ (c) and in-plane ion Mach number M_i (d) from Merino 2023, [6]. 34

4.6 Dimensionless axial (z-directed) and radial (x-directed) ion flow velocity components, u_{zi} (a) and u_{xi} (b). 35

4.7 Dimensionless n, T_e, ϕ and u_i, respectively for $\Omega_{i0} = 1$ and $\Omega_{i0} = 10$. . . . 37

4.8 Dimensionless in-plane ion-electron current density $\tilde{\mathbf{j}} = n(\tilde{\mathbf{u}}_i - u_{\|e}\mathbf{1}_b)$ . . . 38

4.9 Dimensionless electron temperature $T_e = n^{\gamma_e - 1}$. 39

4.10 Dimensionless total ion energy E_i (a) and internal ion energy (ion-thermal component) percentage contribution e_i/E_i (b). 40

4.11 Dimensionless ion pressure p_i map (a) and evolution along selected streamline (b). 41

4.12 Entropy distribution along selected streamline originating on $x = C_t$. . . . 42

4.13 Dimensionless density n for iothermal case $\gamma_e = 1.01$ (a) and $\gamma_e = 5/3$ (b). 43

4.14 Dimensionless electron temperature T_e, ambipolar electric potential ϕ, out of plane electron velocity $u_{ye}B_{a0}$ and ion in-plane velocity u_i, for $\gamma_e = 1.01$, $\gamma_e = 1.2$ and $\gamma_e = 5/3$. 44

4.15 Magnetic force density in the axial $F_{z,B} = -j_y B_x$ (a) and radial $F_{x,B} = j_y B_z$ (b) directions. 46

4.16 Normalized magnetic thrust $F(z)/F(0)$ as a function of z. 47

4.17 Normalized magnetic thrust $F(z)/F(0)$ for $\Omega_{i0} = 10$. 48

4.18 Dimensionless axial total ion axial power $P_{zi}(z)$ (a), and dimensionless total ion power $P_i(z)$ (b). 49

4.19 Plume efficiency ($\eta_{plume} = P_{zi}/P_i$) along the domain. 50

5.1 Thruster outlet boundary conditions for T_{i0} parametric analysis. 53

5.2 Normalized ambipolar electric potential ϕ/T for T_{i0} parametric analysis. . 54

5.3 Plasma density and ion in-plane flow M_i distribution for T_{i0} parametric analysis. 56

5.4 Ion pressure distribution, $p_i = nT_i$ for T_{i0} parametric analysis. 58

5.5 Ion pressure downstream evolution, p_i. 58

5.6 Axial magnetic force $F_z = -j_y B_x$ for T_{i0} parametric analysis. 59

5.7 Normalized generated thrust $F(z)/F(0)$ for T_{i0} parametric analysis. 60

6.1 Magnetic field distribution B/B_{a0} for $d_w = 1$ and $d_w = 3$. 62

6.2 Separatrix positioning ($x_{\psi=0}$) (a) and boundary magnetic streamfunction profile for selected $d_w = 1, 2, 3, 4$ (b). 62

6.3 Dimensionless ambipolar electric field ϕ (a) and out-of-plane electron velocity u_{ye} (b) for $d_w = 1$ and $d_w = 3$. 63

6.4 Dimensionless plasma density n (a)-(b) and in-plane macroscopic flow ion velocity u_i (c)-(d) for $d_w = 1$ and $d_w = 3$. 64

6.5 Dimensionless z-directed electromagnetic force, $F_z = -j_y B_x$ and thrust distribution $F(z)/F(0)$ for $d_w = 1$ and $d_w = 3$. 65

7.1 Magnetic Field Strength B and Electron Thermal Function H_e in 3D Model from POSETS-v2. 67

7.2 Streamfunction ψ (a) and applied magnetic field in the internal section of the MAT (axial (b), radial (c) and total (d). 68

LIST OF TABLES

4.1 MA Simulation ($T_{i0} = 0.01$) Setup Characteristics 29

5.1 MA Simulation for Parametric Analysis Setup Characteristics 52

6.1 Simulation Cases Geometric Setup 61

8.1 Project Costs (VAT included) 72

1. INTRODUCTION

1.1. Motivation and State of the Art. Electrodeless Plasma Propulsion

Plasma propulsion has emerged as a promising field in advanced propulsion space technologies, leading deep-space transport research and aiming to extend operational capabilities of traditional chemical thrusters [1] [2]. Distinguished by high-specific impulse and improved fuel efficiency, plasma propulsion relies on the acceleration of ionized gases through electromagnetic fields to generate low-thrust sustained over extended periods, reducing the required propellant mass and enabling complex and more ambitious interplanetary missions[3].

Numerous plasma propulsion systems have been developed in recent years, including Hall-effect thrusters and ion engines, which have already presented superior performance in certain applications. Nevertheless, certain issues related to plasma handling arise in these devices, particularly regarding material walls contact, electrodes erosion and thermal degradation, which overall limit their useful life. Electrodeless Plasma Thrusters (EPTs) originate with the objective of mitigating the aforementioned inconveniences [4]. In contrast to their predecessors, EPTs rely on electromagnetic energy provided by radio-frequency or microwave sources to ionize and sustain plasma. This eliminates the problems associated with electrode erosion and wall degradation, thereby promising reduced maintenance needs and longer operational lifetimes.

A fundamental aspect of EPTs is the behavior of the plasma beam as it expands into the surrounding vacuum. This magnetically-guided plasma expansion is commonly controlled by a magnetic nozzle (MN), a device that accelerates the plasma by employing a specific convergent-divergent magnetic field configuration generated by a set of solenoids or permanent magnets [5][6][7][8]. A resemblance could be identified between MNs and de Laval nozzles, as both are constituted by a transition region of minimum area where flow becomes supersonic to then continue accelerating in the diverging region, however, operation of MNs is far more complex [9]. Among diverse plasma thrusters design, two common exemplary devices are the Helicon Plasma Thruster (HPT) and the VAriable Specific Impulse Magnetoplasma Rocket (VASIMR).

The HPT in its basic design is constituted by a cylindrical chamber where plasma is produced, a RF plasma source used to ionize the propellant ans sustain plasma production, and a divergent MN of external solenoids that provide a quasi-uniform axial magnetic field [11] [12]. Additionally, an injector system is used to drive the propellant into the chamber. Among the numerous advantages presented by this device, and adding up to the described improvements inherent to EPTs: it does not require large voltages for its operation, it has reduced manufacturing and operation costs, and it offers the possibility of using virtually any propellant [13].

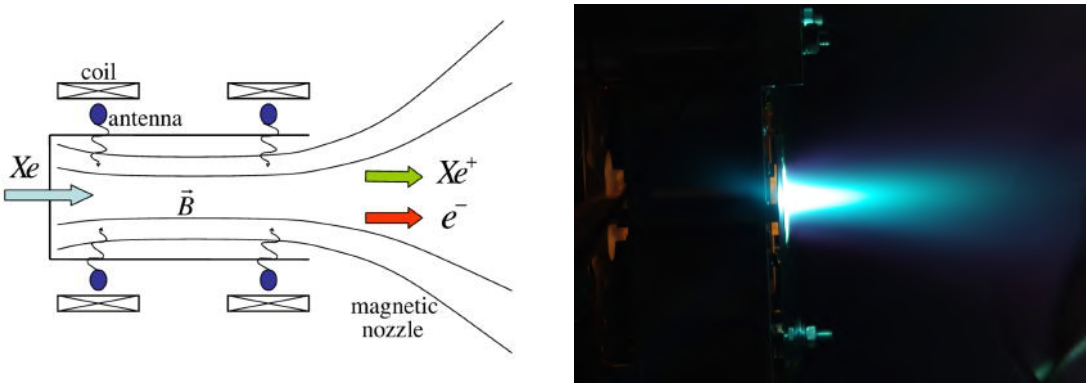

Fig. 1.1. On the left, schematic of Helicon Plasma Thruster (HPT) components, [1]. On the right, HPT prototype operating with Xe in the UC3M vacuum chamber [10].

The VASIMR, on the other hand, could be regarded as a high-power HPT. It is constituted by the same elements as described for the HPT but with an additional intermediate RF heating stage known as Ion Cyclotron Resonance Heater (ICRH) [14][15]. This rapidly transmits cyclotron energy to ions, modifying the plasma expansion and resulting in a notable change in the device operation capabilities. Differently to HPT, internal energy of the generated plasma does not reside solely on electrons, but now ion species account for a non-negligible temperature that could give rise to a significant acceleration mechanism [16][17].

Despite the advances demonstrated by these experimental devices, further research must be performed over EPTs to improve their operational capabilities and compete with conventional platforms such as Hall thrusters or ion gridded engines. Bearing this in mind, the present project intends to explore alternative magnetic nozzle configurations and magnetic field topology models that could possibly result in thrust and efficiency improvements. Particularly, taking as reference the Magnetic Arch Thruster (MAT) [6][18], a novel U-shaped thruster configuration patented by Mario Merino [19], further discussed in Section 1.1.3.

Modeling of the resultant plasma expansion an unveiling the intricate physical mechanisms undergoing in the plume (i.e. plasma detachment and acceleration) remains challenging due to the complex interplay between the diverse species and the applied magnetic field. In this work, advanced numerical simulations implementing finite volume methods (FVMs) are performed using FEniCS library [20] to characterize the distribution of fundamental properties of the fluid plasma model. From the governing fluid partial differential equations, the operational parameters of novel thruster configurations may be studied, to determine optimal plasma collimation, temperature and magnetic field strength characteristics, among others.

This thesis ultimately seeks to deepen the understanding of plasma expansions in magnetic archs, while aiming to optimize EPTs design by redefining conventional configurations. Thereby, contributing to the development of efficient long-lasting propulsion methods for deep-space transport and exploration.

1.1.1. EPTs Limitations

Despite the potential advantages and promising outline of MN-based EPTs, these propulsion devices also present a series of limiting factors that reduce their overall performance and efficiency, positioning them still far behind the more mature technologies like Hall thrusters or gridded ion engines. For reference, mature technologies go up to $50-70\%$ of thrust efficiency, while EPTs values are still low, ranging around 15%, [2] [21].

Performance differences between EPTs and conventional electric thrusters arise from a lack of understanding of a series of physical mechanisms occurring during operation, mainly regarding instabilities and particle-wall interaction. Indeed, when studying the effects of electromagnetic fields over plasma and comparing them with experimental results, these differ widely from theoretical or computational models.

In addition, it has been determined that the current cylindrical design of conventional EPTs presents inherent issues, as stated in [19]; namely:

1. **Large magnetic dipole moment generation**. The applied magnetic field presents a non-zero magnetic dipole, which can interact with the Earth's magnetic field to produce a perturbing magnetic torque on the device and spacecraft, specially at lower orbits.

2. **Large plume divergence**. EPTs typically have a large divergence angle (~ 50) due to far downstream detachment of ions, promoting the appearance of magnetic drag and difficulting vehicle integration.

3. **Efficiency loss in thruster's rear wall**. Approximately a 50% of the generated plasma is unintentionally deviated to the magnetically unshielded rear wall in the plasma source, where a large fraction of the plasma is recombined and lost, thus causing the inefficiency of the thruster [22].

All of the above-mentioned aspects are deleterious and may affect ultimate thruster integration into a spacecraft platform. Consequently, major advancements in the physical understanding of EPTs and breakthroughs in their design are needed to unblock their progress.

1.1.2. Magnetic Arch (MA) Field Configuration

To overcome the limitations of cylindrical EPTs, Mario Merino Martínez, as part of the Zharathrustra project [23], devised a novel thruster configuration based on clustering various EPTs units to conform an arched magnetic field [19] [24] [6], what will be referred to as Magnetic Arch (MA)[18]. This configuration provides the device with a series of notable advantages when compared to conventional cylindrical propellers:

- Firstly, the magnetic dipoles generated by each of the magnetic field portions in the MA EPTs devices are mutually canceled, as these fields present equal direction and intensity with opposite polarity, thus eliminating inconvenience 1).
- Secondly, regarding plume divergence, the configuration of the MA imposes a magnetic field with both open and closed magnetic streamtubes originating from the thruster throats. The fact that part of the magnetic lines connect both nozzles and guide the species' streamlines poses an interesting phenomena: plasma is able to scape this confinement but divergence may be mitigated by orienting the geometry of the clustered units. Consequently, issue 2) would also be addressed.
- Additionally, over more complex models, two MNs may be throttled independently to allow for some degree of thrust vectoring.

Regarding the outside magnetic field, that of the expansion region, recall that it is generally conformed by both closed and open magnetic streamtubes, differentiated by the separatrix, at which, if existent, magnetic streamfunction value is null, $\psi_B = 0$. The term *closed magnetic streamlines* corresponds to those connecting the two magnetic nozzles of the clustered system, while when *open* these propagate downstream as in a MN. The position of the separatrix, is essentially dependent on the devices positioning and geometry, which enables the definition of diverse thruster configurations and proportionalities between open and closed magnetic lines.

The applied magnetic field $\mathbf{B}_a$ over a MA results in a plasma expansion radically different to that in MNs, as flux needs to necessarily transverse the confinement of the closed streamtubes that fall roughly perpendicularly. This alters the generated currents from being solely diamagnetic, to being diamagnetic and paramagnetic respectively in the upstream and downstream regions of the expansion [6]. Additionally, differently from MNs, in which the plasma-induced magnetic field $\mathbf{B}_p$ contribution plays a secondary role if well designed [25], in MAs $\mathbf{B}_p$ may completely alter the topology of the total field, $\mathbf{B} = \mathbf{B}_a + \mathbf{B}_p$. Studies conducted at [6], show that as the beta of the plasma $\beta = \mu_0 n T_e / B_a^2$ is increased, hence enlarging the induced field influence, the geometry of the central lines of the MA is altered, stretching these downstream and converting some inner magnetic lines (that previously intersected the symmetry plane) into outer lines (open lines). The matter of plasma-induced magnetic field will not be discussed further and the case for which $\beta_0 \to 0$ is to be analyzed, but its influence over magnetic field topology must not be forgotten.

Continuing with magnetic field topology, let us revisit the various possible MA configurations that may arise from selected geometry and hence, by separatrix line positioning:

1. The case in which the separatrix line falls within the limiting magnetic lines at the edges of the source constitutes the general *open arch* formation, depicted in Fig. 1.2(a). In this MA type there are both inner (closed) and outer (open) magnetic

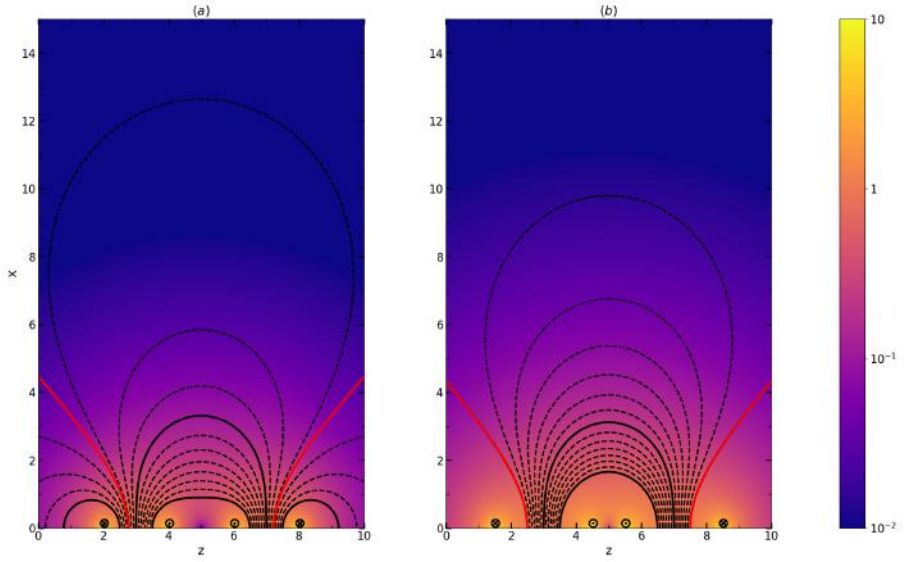

Fig. 1.2. Open Magnetic Arch (a) and Closed Magnetic Arc (b). Solid black lines correspond to magnetic streamtubes originating from edges and center of the thrusters, dashed black lines represent selected magnetic field streamlines and red line represents the separatrix at which $\psi_B = 0$.

streamtubes. Open arch is the case generally simulated in this project, unless otherwise specified. The plasma expansion may still be globally current-free, as long as the open lines above the separatrix carry the arising electron current responsible of balancing the ion current [6].

2. If all magnetic lines fall below the separatrix, connecting both sources, a *closed magnetic arch* is constituted, as shown in Fig. 1.2(b). This configuration arises from larger separation being set between the magnetic field generators and the source.

3. The last case is defined by the separatrix falling below all magnetic lines originating from the source, conforming a field topology of solely open streamtubes. This configuration is not strictly defined as MA, as no real 'arch' is constituted. The situation would arise when plasma sources are not concentric with the magnetic generators [6].

A primary simulation and analysis has been conducted numerically in Merino 2023 [6], implementing the python-based framework POSETS developed by Diego García-Lahuerta, a finite volume method fluid solver intended for plasma expansion characterization in EPTs. Initial results show a plume expansion that manages to scape the confinement of closed magnetic streamtubes and accelerates downstream, similarly to what would be expected from a conventional MN. An oblique shock structure is developed along the expansion as the jet beams from the clustered devices collide in the symmetry plane, deviating ion streamlines and presenting a property discontinuity. From [6] and further experimental verification conducted at [18], the MA configuration is devised as a working electrodeless propulsion device pending from further optimization.

1.1.3. Magnetic Arch Thruster (MAT)

As an additional note, Mario Merino Martínez recently patented a novel thruster configuration based on a U-shaped geometry[1] [19] [24] [6], what will be referred to as Magnetic Arch Thruster (MAT). This novel plasma motor is comprised of a dielectric-material, U-shaped ionization chamber and a magnetic field generation device, which is designed to provide a strictly parallel field to the ionization chamber walls.

Due to its U-shaped geometry, with open magnetic nozzles at each of the branches, the rear wall (present in rectilinear configurations) is eliminated. Instead, two plasma beams are generated and flow in parallel to the device walls, directed and confined by the applied magnetic field. Thereby, inconvenience 3) is eliminated. This phenomena, already expected in conventional MN to ensure thruster's efficiency, thermal resistance and an elongation of its useful life, is maintained along the complete structure at all regions, thus the topology of the magnetic field needs to adhere to the toroidal formation.

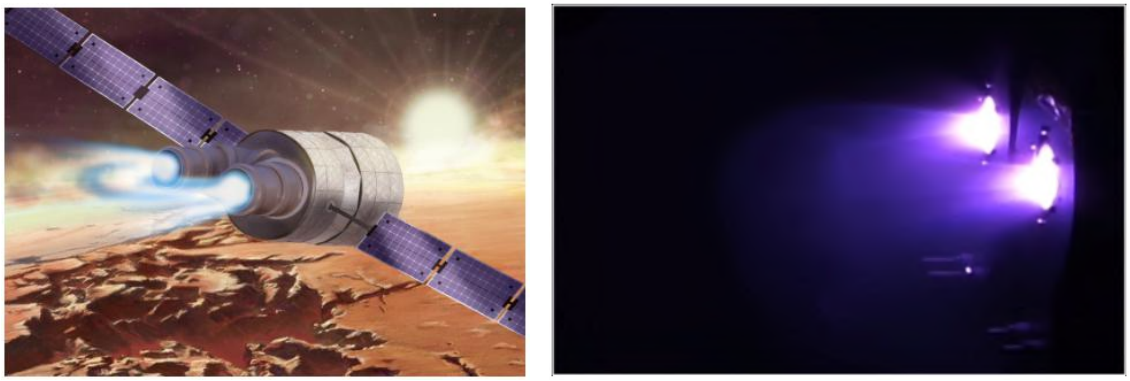

Fig. 1.3. On the left, Magnetic Arch Thruster (MAT) Concept Art integrated into spacecraft, [23]. On the right, dual-source cluster in operation featuring a a magnetic arch (MA), retrieved from [18]

1.2. Objectives of this Work

The primary aim of this research project is to develop a high-fidelity numerical simulation framework for electrodeless plasma thrusters, in order to unveil the physical phenomena underlying the expansion mechanisms of clustered systems of cylindrical MNs conforming a Magnetic Arch (MA).

Building upon earlier models and software, which have provided essential insight on plasma expansion and acceleration, this work seeks to address their limitations and improve physical accuracy. Specifically, the objectives may be outlined as follows,

1. **Inclusion of Ion Energy Equation**. A key innovation of this work is the inclusion of an ion energy conservation framework into the simulation. With this, we aim

[1] Also referred to in literature as C-shaped electric thruster [6].

to evaluate the distribution transformation of electron and ion thermal energies into direct kinetic energy through the propulsion process.

In this context, the project intends to confirm ion temperature evolution according to the cooling law $T_i = T_{i0} n^{\gamma_i - 1}$, where ions are expected to be adiabatic, and perform a thermodynamic analysis over various T_{i0} cases.

Additionally, this update aims to confirm the development of oblique shock structures originating in cold ion models and adequately characterize other arising discontinuities.

2. **Provide an Study on Electron and Ion Cooling parameters.** Evaluate the influence of the electron polytropic exponent in $T_e = n^{\gamma_e - 1}$, which determines how rapidly the electrons lose thermal energy as they expand. Moreover, it influences the formation of ambipolar electric fields which drive the plasma acceleration downstream.

   Assess the impact of the initial imposed ion temperature at the thruster's throat T_{i0} to determine the influence of ion cooling, the efficiency of energy conversion, and the resulting plasma dynamics, including the maximum attainable flow velocity.

3. **Evaluate Magnetic Generators Positioning and Geometry.** Provide a complete analysis on the influence of the magnetic field generators (i.e. current loops, fixed magnets, etc.) positioning with respect to the thrusters' nozzles. Study the closed and open MA configurations and asses their benefits and inconveniences. Particularly, determine whether the plasma jet is able to scape magnetic confinement in closed MAs.

   Identify optimal configurations for plume divergence reduction and thrust efficiency enhancement.

4. **Code Improvements on accuracy and convergence.** On top of the model code improvements required to asses the analysis described in previous Objectives, several numerical improvements are targeted to mitigate computational errors and flux dissipation.

   The project intends to accelerate the convergence process to offer a straightforward fluid solving framework that encompasses the physical mechanisms of plasma expansion in an effective and compact code.

1.3. Project Outline

The investigation begins with the development of the magnetic field and plasma model for ions and electrons in Chapter 2. A special focus is given to the inclusion of the energy conservation law and energy conversion processes during expansion. All necessary and imposed assumptions are detailed in this chapter.

Chapter 3 continues with the numerical integration techniques to solve the ion-electron equations outlined in the previous Chapter. This includes defining the finite volume approach, the numerical flux function and the time integration protocol, ending with the introduction of the new features implemented on POSETS-v2, the solving python-based framework.

Chapter 4 includes the results and discussion for the case $T_{i0} = 0.01$, which is compared to the cold ion model developed on [6]. Verification of the resulting expansion in the cited article is performed, by sophisticating the physical model implemented.

Chapter 5 is devoted to evaluating the influence of the initial ion temperature T_{i0} boundary conditions, performing simulations for $T_{i0} = 0.1, 1, 3$ and 10. This Chapter is intended to explore devices that rely on larger ion thermal energies for plasma acceleration, instead of fully electron-thermally accelerated flows.

Chapter 6 performs various simulations on diverse magnetic field topologies, including open and closed magnetic arch configurations. This intends to determine optimal positioning of the magnetic generators and geometry of the nozzle system.

Chapter 7 serves as a conclusive section of the project, where future work is outlined and previous discussion is summed up to detail the relevant conclusion that arises from the performed research. In this Chapter, initiated parallel projects are displayed as introduction to what comes in further investigations.

Lastly, Chapter 8 outlines the existent legal framework to which the project is subjected and the socio-economic impact of the work performed. A budget estimation is also included in this Chapter, to serve as an approximate indicator of the total cost of the activities carried out.

1.4. Acknowledgments

This work has been carried out in the framework of the ZARATHUSTRA project, which received funding from the European Research Council (ERC) under the European Union's Horizon 2020 research and innovation programme (grant agreement No 950466).

2. PLASMA MODEL

2.1. Plasma Model Assumptions

Plasma is characterized by the collective motion of numerous particles and their interplay through the Coulomb interaction. Due to its intrinsic complexity and the enormous number of elements contained within a small volume, it is typically not feasible to trace particle motion all along the domain [26]. In other words, relying on particle-in-cell (PIC) methods to study large-scale evolutions of plasmas is often impractical due to computational challenges and resource demands associated with this simulations. Therefore, instead of kinetic or PIC methods, the model may be simplified by assuming the distribution function to be Maxwellian locally or, what is the same, that plasma is modeled as a fluid, as performed in [27].

A plasma steady state, two-fluid model composed of singly-charged ions (i) and electrons (e) is then considered as function of time and space (t, $\mathbf{r}$) for density (n), velocity ($\mathbf{u}$) and energy (E). Nevertheless, a set of further assumptions is necessary to achieve a physically coherent and mathematically tractable model.

1. *Quasineutral, collisionless, fully-ionized plasma.* In a quasineutral medium the difference between the density charges of the species is negligible [28]. The approximation holds true over macroscopic scales larger than the Debye length ($\lambda_D = (4\pi n_e e^2/kT_e)^{1/2})^2$, as can be determined from Eq. 2.1.

$$\frac{|n_i - n_e|}{n} \sim \frac{\lambda_D^2}{L^2} \ll 1, \tag{2.1}$$

   where $L = |\nabla \ln n|^{-1}$ is a typical spatial density scale. The paradigm of quasineutrality results on the densitites of the charge species to be considered equal $n \equiv n_i = n_e$.

   Additionally, plasma is assumed to be collisionless, implying that the mean distance between two consecutive collisions, the mean-free path, is considerably large compared to the scale of the system under study. Thereby, the consideration $R_V \ll \lambda_c$ holds in the presented model, where λ_c is treated as the electron-ion collision mean-free path and $R_V(z)$ as the jet cross-section radius along the nozzle. As a consequence, ion trajectories are only affected by the ambipolar electric field, strictly related to plasma density gradients in the plume. [29].

   Lastly, plasma is fully ionized, consisting solely of charged particles, electrons and ions. Negligible presence of neutral particles is assumed and particle dynamics are governed by electromagnetic forces rather than molecular or atomic interactions.

[2]Note that until otherwise stated, equations will be introduced and interpreted in dimensional form, with variables taking adequate International Sytem Units (SI).

2. *Inertialess, quasi-Maxwellian, perfectly-magnetized electrons with a polytropic closure relation.* Electron inertia is neglected with respect to ion inertia, $m_e \ll m_i$. Furthermore, electron population is assumed to be fully magnetized and the electrons' trajectories coincide with magnetic streamtubes. This assumption requires that the dimensionless electron Larmor radius based on the sonic velocity is small.

$$\varepsilon_e = \frac{c_e}{\Omega_e} = \frac{\sqrt{\gamma_e T_e}}{B} \ll 1 \tag{2.2}$$

The Larmor radius arises from the radius of the cycloidal motion imposed by centripetal component of the Lorentz force in presence of a magnetic field [30].

As previously commented, the agent capable of influencing ion trajectories is the ambipolar electric field which, in general, depends on the evolution of the electron energy distribution function (EEDF). Any cooling will then affect the energy of the downstream plasma, and therefore the thrust gain produced, the potential jump, and the the final velocity of the plasma [9]. Although basic plasma phenomena is expected to be qualitatively independent of electron thermodynamics, prediction of the EEDF is not a trivial task in regions of collissionless plasma regimes, consequently, a predefined evolution of the function is assumed to close the equations. Electrons are modeled as quasi-Maxwellian species and their density (n_e) and temperature (T_e) are given by a polytropic electron cooling law in Eq. 2.3 with fixed exponent $\gamma_e > 1$.

$$T_e \propto n_e^{\gamma_e - 1} \tag{2.3}$$

3. *Singly-charged ions, with arbitrary magnetization emitted from each source exit.*

Eq. 2.2 indicates that magnetic strength is large enough to confine electron momentum along magnetic streamlines, but it does not provide information regarding ion magnetization [6]. Besides, no particular assumption has been made accounting for ion motion in the magnetic field besides that the ion-electron mean-free path will be large enough to prevent collisions.

The local and initial ion gyrofrequency is defined by the source exit at the nozzle throat, thus explaining the reason behind magnetization arbitrariness. Nevertheless, it may be generalized that ion magnetization will be mild and of order one, as seen in Eq. 2.4.

$$R\Omega_{i0}/u_{i0} = O(1), \tag{2.4}$$

where $\Omega_i = eB/m_i$ is the ion gyrofrequency, the subscript 0 refers to the nozzle throat, and u_i is the macroscopic ion velocity. Notice that, except for $R\Omega_{i0}/u_{i0} \to \infty$, ion streamlines do not coincide with magnetic streamlines, as electron do.

4. *Low Beta, current-free plasma*. Finally, although not explicitly required in our model, plasma is considered current-free, so that the electric current across any radial section of the external jet cross-section of radius $R_V(z)$ is zero,

$$I(z) = \int_{A_V(z)} dA\, j_z = 0. \tag{2.5}$$

Here, $A_V(z) = \pi R_V^2(z)$ is the plasma jet cross section at z and j_z is the axial component of the total electric current density $\mathbf{j} = -en_e\mathbf{u_e} + en_i\mathbf{u_i}$.

The imposed assumptions, or those that arise as consequence of the ones commented, compose a set of fundamental simplifications that will benefit problem solving and interpretation both from the computational and physical perspectives. Nevertheless, it is to be considered that, even though the expansion solution under these premises will be highly resemblant to experimental plasma plumes, corroboration and verification will be indispensable as future work. Particularly, the error committed in the assumption of a simplified electron cooling law under a polytropic relation needs to be evaluated to asses the limits of fluid models.

Lastly, it is of importance to mention that the model has been normalized to ease physical interpretation and numerical integration. In order to do this, the following magnitudes are selected, as performed in [6]: the ion mass m_i, the electron charge q_e, and the radius R of one of the plasma thruster exits. Additionally, a set of properties evaluated at the center of one of the symmetric thruster outlets are also considered: the plasma density n_0, the ion temperature T_{i0} and the electron temperature T_{e0}, where, as before, the subindex corresponds to the injection value. Notice that, in certain simulations for a set of specific boundary conditions, the plasma flux may arrive at the symmetric outlet, consequently affecting the flux in it. However, the definition of n_0, T_{e0} and T_{i0} remains unaltered, with values taken from the single-beamlet injection properties.

Finally, the magnetic field strength at the center of the thruster, B_0, is normalized with $\sqrt{m_i T_{e0}}/(eR)$, which is numerically equivalent to the dimensionless ion gyrofrequency Ω_{i0}.

2.2. Magnetic Field Model for MA

This Section is devoted to the mathematical and physical apparatus required to model the magnetic field topology resultant from a MA configuration.

For the sake of convenience, let us define two useful reference systems: the Cartesian vector basis $\{\mathbf{1}_z, \mathbf{1}_x, \mathbf{1}_y\}$ and the magnetic vector basis $\{\mathbf{1}_\parallel, \mathbf{1}_\perp, \mathbf{1}_\times\}$. On the one hand, the Cartesian reference is the right-handed orthonormal basis that constitutes the plane O_{xy}, coincident with the exit plane of the plasma sources, the plane O_{zx}, which is the plane under study in a two dimensional case, and O_{zy}, which corresponds to the symmetry plane [6]. This basis is used to determine the solution for the plasma model general equations (Chapter 2), with flow properties being defined in the aforementioned directions. On the other hand, the magnetic vector basis, also right-handed and orthonormal, with $\mathbf{1}_\parallel = \mathbf{B}/B$ and $\mathbf{1}_\perp = \mathbf{1}_\times \times \mathbf{1}_\parallel$, offers a more intuitive representation of plasma transport along, across, and perpendicular to magnetic field lines.

The applied magnetic field $\mathbf{B}_a$ is generally generated by a set of circular wire loops

centered at $\mathbf{C}_w$ and with a radius R_w, each carrying an electric current I_w along the azimuthal direction $\mathbf{1}_\times$. This is modeled using the Law of Biot Savart, which may be integrated along the loop in cylindrical coordinates, where $r = \sqrt{(x - C_{w,x})^2 + (y - C_{w,y})^2}$. Hence, the off-axis magnetic field of a current loop is described by [31],

$$B_z = B_0 \frac{1}{\pi\sqrt{Q}} \left[E(k) \frac{1 - \alpha^2 - \beta^2}{Q - 4\alpha} + K(k) \right], \tag{2.6}$$

$$B_r = B_0 \frac{\gamma}{\pi\sqrt{Q}} \left[E(k) \frac{1 + \alpha^2 + \beta^2}{Q - 4\alpha} - K(k) \right]. \tag{2.7}$$

Where B_0 is the magnetic field strength at the center of the coil loop, and $K(k)$ and $E(k)$ are the complete elliptic integral functions of the first and second kind, respectively. The additional parameters are defined as,

$$\alpha = \frac{r}{R_w}, \qquad \beta = \frac{z}{R_w}, \qquad \gamma = \frac{z}{r}, \qquad Q = \left[(1 + \alpha)^2 + \beta^2 \right], \qquad k = \sqrt{\frac{4\alpha}{Q}}. \tag{2.8}$$

Components of the applied magnetic field strength might then be expressed in the corresponding Cartesian basis such that $\mathbf{B} = B_z \mathbf{1}_z + B_r \sin\theta \mathbf{1}_x + B_r \cos\theta \mathbf{1}_y$, computed for each of the magnetic generators and added up to constitute the magnetic arch.

In a two dimensional model, the applied magnetic field can be defined as being generated by a set of infinite electric wires, each carrying an electric current I_w along the $\mathbf{1}_y$ direction. The magnetic stream function of a single wire would then be given by,

$$\psi_{B,w} = -\frac{\mu_0 I_w}{2\pi} \ln \rho_w, \tag{2.9}$$

where ρ_w is the polar distance from the wire. Summing all wire contributions, the resultant streamfunction is that of the applied field, $\psi_{B,a}$. Which, in the absence of an induced magnetic field ($\beta_0 = 0$) is $\psi_B = \psi_{B,a}$ and $\mathbf{B} = \nabla\psi_B \times \mathbf{1}_y$.

2.3. General Plasma Equations

Before assumption imposition and model specific modifications, it is relevant to overview the general macroscopic non-dimensional fluid equations for a species j of a collisionless plasma under the effect of a predetermined magnetic field $\mathbf{B}$,

$$\frac{\partial n_j}{\partial t} + \nabla \cdot (n_j \mathbf{u_j}) = 0, \tag{2.10}$$

$$\frac{\partial (n_j \mathbf{u_j})}{\partial t} + \nabla \cdot (n_j \mathbf{u_j} \mathbf{u_j}) = -\nabla p_j - q_j n_j \nabla\phi + q_j n_j \mathbf{u_j} \times \mathbf{B}, \tag{2.11}$$

$$\frac{\partial E_j}{\partial t} + \nabla \cdot ((E_j + p_j)\mathbf{u_j}) = -q_j n_j \mathbf{u_j} \cdot \nabla\phi. \tag{2.12}$$

where n_j is the density of the species, $\mathbf{u}_j$ the fluid flow velocity vector and E_j the total energy (encompassing thermodynamic internal energy (e_j) and kinetic energy of the fluid

flow), which are the system variables being solved for in this hyperbolic Euler-like problem of PDEs. Additionally, q_j is the non-dimensional electric charge ($q_i = 1$ and $q_e = -1$), ϕ is the ambipolar electric potential, and the rest of the symbols are conventional [5]. Eq. 2.10 accounts for continuity or mass conservation, Eq. 2.11 for momentum conservation in all directions of the considered spatial domain, with pressure p_j being a tensor, and Eq. 2.12 solves for energy conservation of the species, with E_j defined as,

$$E_j = n_j e_j + \frac{1}{2} n_j \|\mathbf{u_j}\|^2. \tag{2.13}$$

Making use of the previous expression, where the term e_j accounts for internal energy, Eq. 2.12 may be decoupled to result in the differential equation for internal energy conservation (Eq. 2.14) and an equation for the kinetic term (Eq. 2.15), as derived in [32], that may be appropriate for some specific implementations.

$$\frac{\partial n_j e_j}{\partial t} + \nabla \cdot (n_j e_j \mathbf{u_j}) = -p_j \nabla \cdot \mathbf{u_j}, \tag{2.14}$$

$$\frac{\partial}{\partial t}\left(\frac{1}{2} n_j \|\mathbf{u_j}\|^2\right) + \nabla \left(\frac{n_j \|\mathbf{u_j}\|^2}{2} \mathbf{u}_j\right) = -\mathbf{u_j} \cdot \nabla p_j - q_j n \mathbf{u} \cdot \nabla \phi. \tag{2.15}$$

Observe that, assuming external force terms in momentum equations may be predefined by magnetic field imposition and isentropic electron temperature distribution, there is yet another relation necessary to make the fluid equations in closed form. An equation of state (EOS) given with temperature (T_j) as new thermodynamic variable is defined for pressure and internal energy such that,

$$p_j = p_j(n_j, T_j) = n_j T_j, \tag{2.16}$$

$$e_j = e(n_j, T_j) = \frac{1}{\gamma_j - 1} T_j, \tag{2.17}$$

where T_j is expressed in units of energy[3] including Boltzmann constant k_B and the equality holds for $\gamma_j \neq 1$.

2.4. Electron Model

Assumption for inertialess electrons and introduction of the polytropic closure relation into the system lead, after some rearrangements, to the relevant continuity and momentum fluid equations for electrons,

$$\partial_t n + \nabla \cdot (n \mathbf{u_e}) = 0, \tag{2.18}$$

$$0 = -\nabla n T_e + n \nabla \phi - n \mathbf{u_e} \times \mathbf{B}, \tag{2.19}$$

[3]The practice of expressing T_j in energy units will be recurrent in further derivations, unless an indication declares otherwise.

For the sake of convenience, besides the Cartesian vector basis $\{\mathbf{1}_x, \mathbf{1}_y, \mathbf{1}_z\}$, the local magnetic vector basis $\{\mathbf{1}_\parallel, \mathbf{1}_\perp, \mathbf{1}_\times\}$ is made use of. The fluid velocity of electrons may be decomposed then into its parallel component and a drift vector along $\mathbf{1}_\perp$ and $\mathbf{1}_\times$, denoted in Eq. 2.20 as $\hat{\mathbf{u}}_e$.

$$\mathbf{u}_e = u_{\parallel e}\mathbf{1}_\parallel + \hat{\mathbf{u}}_e \tag{2.20}$$

Assumption 2.2 describes fully magnetized electrons and allows the asymptotic expansion of Eq. 2.18 and Eq. 2.19 around the zero-Larmor radius limit, where the motion of electrons is mainly given along magnetic lines. As plasma expands supersonically, electrons have parallel velocity of the order of the sonic velocity, $u_{\parallel e} \sim c_s$, and drift velocities, considering both diamagnetic and $\mathbf{E}\times\mathbf{B}$ drifts, which scale as $\hat{u}_e \sim \varepsilon_e c_s$ [33]. This leads to the presented assumption, in the limit $\varepsilon_e \to 0$, $\hat{\mathbf{u}}_e$ is negligible and electron streamlines coincide with magnetic lines.

With this premises, Eq. 2.18 is rearranged as follows,

$$0 = -\frac{1}{n}\nabla(n^{\gamma_e}) + \nabla\phi - \hat{\mathbf{u}}_\mathbf{e}B, \quad \text{where} \quad -\frac{1}{n}\nabla(n^{\gamma_e}) = -\frac{\gamma_e}{\gamma_e - 1}\nabla n^{\gamma_e - 1}, \tag{2.21}$$

$$0 = -\nabla\left[\frac{\gamma_e}{\gamma_e - 1}(n^{\gamma_e - 1} - 1) - \phi\right] - \hat{\mathbf{u}}_\mathbf{e}B. \tag{2.22}$$

Eq. 2.22 is then integrated along the magnetic streamlines to define the electron tube-wise Bernoulli function $H_e(\psi_B)$ (electron energy), which is conserved along them,

$$H_e(\psi_B) = \frac{\gamma_e}{\gamma_e - 1}(n^{\gamma_e - 1} - 1) - \phi \tag{2.23}$$

Eq. 2.23 can be also interpreted as a generalized Boltzmann relation on each stream-tube, with $-H_e(\psi_B)$ understood as the thermalized potential [6].

Observe that while the electron drift velocity component $\hat{\mathbf{u}}_e$ is of the order $O(\varepsilon_e)$, the magnetic force term arising in the momentum equation $\hat{\mathbf{u}}_\mathbf{e}B$ is zeroth-order and, in a fully magnetized electron plasma, this term is responsible for most of the confinement and streamline deflection of each species [33]. Making use of Eq. 2.22, drift components ($u_{\perp e}$ and $u_{\times e}$) of the momentum equations may be written as:

$$\hat{\mathbf{u}}_\mathbf{e}B = -\mathbf{1}_\parallel \times \nabla H_e \quad \text{so that} \quad \hat{\mathbf{u}}_\mathbf{e} = \frac{-1}{B}(\mathbf{1}_\parallel \times \nabla H_e). \tag{2.24}$$

Notice that, due to the conservative property of the electron energy function along magnetic streamlines, $H_e(\psi_B)$, the map of ∇H_e, and consequently $\hat{\mathbf{u}}_\mathbf{e}$, can be computed from imposed boundary conditions at the thruster outlet. This computation may be performed before solving the system of differential equations that determine the plasma regime. One value of H_e shall be imposed to restrict its magnitude along magnetic streamlines, thus setting valid boundary conditions along the considered domain.

From Eq. 2.20, the drift velocity component is solved algebraically from the map of ∇H_e, but note that the parallel component to the magnetic streamlines $u_{\parallel e}$ is completely

decoupled from the system, as it does not appear in Eqs. 2.27-2.29. It may be computed once the plasma problem has been fully solved for, from Eq. 2.18 in steady state and projecting it along $\mathbf{1}_{\parallel}$, as indicated in the simplified expression 2.25.

$$\frac{\partial}{\partial \mathbf{1}_{\parallel}}\left(\frac{n u_{\parallel e}}{B}\right) = 0 \tag{2.25}$$

Continuing with the definition of ϕ, The discrepancy between the ion and electron bulk flow velocities in a diverging expansion requires that a parallel ambipolar electric field develops to maintain quasineutrality, which consequently leads to the flow of a parallel current arising in the plume. This acts by retarding electron motion while simultaneously accelerating ions. The rise of the ambipolar potential (ϕ) plays a fundamental role in ion acceleration, as it is the mechanism that allows for conversion of thermal electron energy to direct kinetic ion energy [34]. In other words, electrons, magnetically confined in the field streamlines, transfer energy to ions, which allow the later species to gain momentum in the axial direction, thus accelerating and contributing to thrust formation.

The ambipolar electric field will be determined from the imbalance between the expanding electron pressure and the confining thermalized electron potential (in consonance with Eq. 2.26), which would essentially model the Hall force in the system. Ambipolar potential gradient scales as $\nabla\phi \sim \frac{\nabla p_e}{n}$ due to its dependence on electron pressure gradient occurring as plasma escapes the magnetic nozzle.

Observe that Eq. 2.23 may be regarded as the law that provides the electrostatic potential as a function of the electron density and the electron thermalized potential. Recall that the electron thermalized potential could be computed algebraically along the magnetic streamlines given a set of boundary conditions, which implies that the electrostatic potential expression will essentially depend on n and ψ_B, such that,

$$\phi(n, \psi_B) = \frac{\gamma_e}{\gamma_e - 1}(n^{\gamma_e - 1} - 1) - H_e(\psi_B). \tag{2.26}$$

The physical relevance of the ambipolar potential does not simply rely on the energy transfer and ion acceleration mechanism, but its distribution presents a fundamental role for plume control in the radial direction at non-negligible ion pressure conditions. Dominant ion thermal energy in the model poses a new paradigm in which a mechanism for perpendicular confinement of energy in the initial plasma column needs to be defined. This can be understood by analyzing radial equilibrium at the nozzle throat. Consider the case for which $p_i \ll 1$ and 'hot' electrons, in this situation the presence of an expanding force originated from the ion pressure gradient is negligible, and the magnetic force from the magnetically confined electrons will account for the electron pressure gradient at the thruster's outlet[4], thus preventing the plume from expanding on the radial direction at $z_0 = 0$ In other words, the gyration of each electron about its magnetic line adds up to

[4]For a negligible ion pressure gradient, the ambipolar potential boundary condition at the thruster's outlet will be set to $\phi_0(0, x) = 0$ at the prescribed thruster's domain.

give rise to a diamagnetic drift current that balances forces radially at the throat. Nevertheless, for models in which ions carry part of the thermal energy, that scale as $p_i \sim O(1)$ or at higher magnitudes, ion pressure gradient would be no longer negligible and the extra radial pressure should be confined too. Because of the mild and arbitrary initial ion magnetization, ion magnetic force would not be sufficient to counteract the radial expansion of the plume initially, increasing the divergence angle and leading to a rapid loss of thrust and efficiency.

Note from Eq. 2.28 that, at steady state and for weak ion magnetization ($\mathbf{u_i} \times \mathbf{B} \approx 0$), the only term counteracting the introduced ion pressure force in the axial direction is the ambipolar potential. Indeed, the expected scenario in this case is that ions are confined by the radial electric field, $\partial p_i/\partial r \approx -n\partial\phi/\partial r$ [35]. The consequence of this phenomenon poses a fundamental imposition from the simulation perspective over boundary conditions, as these will need to be adequately assessed to confine ions strictly axially at the nozzle exit. It is worth mentioning that ion pressure will not only determine throat ambipolar electrostatic potential, but it will highly determine its evolution downstream, as will be seen in Chapter 5 of the present thesis.

2.5. Ion Model

Ion species continuity, momentum and energy fluid equations are depicted below, accounting for the imposed assumptions and simplifications,

$$\partial_t n + \nabla \cdot (n\mathbf{u_i}) = 0, \tag{2.27}$$

$$\partial_t (n\mathbf{u_i}) + \nabla \cdot (n\mathbf{u_i}\mathbf{u_i}) = -\nabla n T_i - n\nabla\phi + n\mathbf{u_i} \times \mathbf{B}, \tag{2.28}$$

$$\partial_t E_i + \nabla \cdot ((E_i + nT_i)\mathbf{u_i}) = -n\mathbf{u_i} \cdot \nabla\phi, \tag{2.29}$$

where the the system is complemented with the algebraic equations Eqs. 2.30-2.31.

$$E_i = \frac{1}{\gamma_i - 1} nT_i + \frac{1}{2} n \|\mathbf{u}_i\|^2, \tag{2.30}$$

$$T_e = n^{\gamma_e - 1} \quad \text{resulting in} \quad p_e = nTe = n^{\gamma_e} \tag{2.31}$$

A set of rearrangements may be performed over the ion energy equation, Eq. 2.29. Consider, in first instance, the term $\nabla\phi$ which, due to its definition, translates into derivatives of the dynamic variables considered in the system, particularly the density n, leading to a non-conservative formulation of the problem. Furthermore, as investigated in Chapter 3, the presence of this derivatives implies that jump conditions across element boundaries in a Discontinuous Galerkin space are not handled correctly by the numerical solver.

In order to solve for the ion energy equation appropriately, consider the gradient product rule and ion continuity given by Eq. 2.27 to rewrite the term,

$$\begin{aligned} \mathbf{j_i} \cdot \nabla\phi = \nabla \cdot (\mathbf{j_i}\phi) - \phi\nabla \cdot \mathbf{j_i} = \nabla \cdot (\mathbf{j_i}\phi) + \phi\partial_t n = \\ = \nabla \cdot (\mathbf{j_i}\phi) + \partial_t(n\phi) - n\partial_t(\phi). \end{aligned} \tag{2.32}$$

From Eq. 2.32, a new energy expression ($\hat{E}_i$) may be defined for convenience by adding up the total ion energy to a component governed by the ambipolar electric potential ϕ,

$$\hat{E}_i = E_i + n\phi = \frac{1}{\gamma_i - 1} nT_i + \frac{1}{2} n\|\mathbf{u}_i\|^2 + n\phi. \tag{2.33}$$

Rewriting the ion energy equation to include the previously commented rearrangements recovers the conservative formulation that is needed, shown in Eq. 2.34. Note that a new time derivative of ϕ arises on the right hand side in this formulation. Nevertheless, this is of little concern as it may be computed numerically in a Discontinuous Galerkin space without issue, and regardless, it is zero when solving in steady state.

$$\partial_t \hat{E}_i + \nabla \cdot [(\hat{E}_i + p_i)\mathbf{u}_i] = n\partial_t \phi \tag{2.34}$$

Notice that, if solving the plasma equations for the new notation $\hat{E}_i$, the ion pressure will be defined now as a function of the electric potential,

$$p_i(n, \mathbf{u}_i, \hat{E}_i) = (\gamma_i - 1)\left(\hat{E}_i - \frac{1}{2} n\|\mathbf{u}_i\|^2 - n\phi\right) \tag{2.35}$$

Prior research on plasma expansion physics assume cold ions, and consider the species to remain cold downstream along the plume structure, neglecting the effects of shock-like discontinuities (Ahedo et al. [5] and Merino et al. [6]), or impose a polytropic cooling law for ions similarly to the imposition for isentropic pressure distribution in 2.3 (Merino et al. [35]). In such cases, the non-dimensional definition $c_s = \sqrt{\gamma_e T_e}$ for ion-sound speed may be applicable under certain restrictions for the ion acoustic waves (IAWs). Nevertheless, as shown by Dubinov in [36] the general formulation for sound speed may only be implemented when considering a single-species plasma or for ordinary plasmas in which an ion-electron thermal equilibrium exists neglecting ion temperature.

The conducted study intends to explore a range of possible ion temperatures which differ from this property being negligible, and to determine accurate solutions for the Mach number of solitons in this plasma model. To derive an exact expression for the sound speed, the dispersion relation of the ion plasma waves as a function of the wave frequency with respect to the wave number, $\omega(k)$, needs to be computed from Eqs. 2.27-2.29. For the sake of simplicity, additional details on the derivation may be found in [37]. Finally, by simplification of the dispersion relation and using the standard definition of sound speed as $c_s = \lim_{\kappa \to 0} \frac{\omega}{\kappa}$ or $c_s = \lim_{\kappa \to 0} \frac{\partial \omega}{\partial \kappa}$, a generalized expression for ion-sound speed dependent on each species' polytropic index may be found

$$c_s = \sqrt{\gamma_e T_e + \gamma_i T_i}. \tag{2.36}$$

2.6. Coupled Ion-Electron Plasma Model

Once the ion and electron model species have been fully characterized and the proper rearrangements and simplifications defined, a closed set of Euler-like partial differential

equations for determining n, $\mathbf{u_i}$, and E_i, and algebraic expressions for ϕ and $\mathbf{u_e}$ may be rendered.

$$\partial_t n + \nabla \cdot (n\mathbf{u_i}) = 0, \tag{2.37}$$

$$\partial_t (n\mathbf{u_i}) + \nabla \cdot (n\mathbf{u_i}\mathbf{u_i}) + \nabla p_i + \nabla (n^{\gamma_e}) = (\mathbf{1}_\parallel \times \nabla H_e) + n\mathbf{u_i} \times \mathbf{B} \tag{2.38}$$

$$\partial_t \hat{E}_i + \nabla \cdot [(\hat{E}_i + p_i)\mathbf{u}_i] = n\partial_t \phi, \tag{2.39}$$

$$\phi = \frac{\gamma_e}{\gamma_e - 1}(n^{\gamma_e - 1} - 1) - H_e, \tag{2.40}$$

$$\hat{\mathbf{u}}_\mathbf{e} = \frac{-1}{B}(\mathbf{1}_\parallel \times \nabla H_e), \tag{2.41}$$

$$\frac{\partial}{\partial \mathbf{1}_\parallel}\left(\frac{n u_{\parallel e}}{B}\right) = 0. \tag{2.42}$$

Eqs. 2.37-2.39 are the PDEs to be solved for n, $\mathbf{u_i}$, and E_i, while Eqs. 2.40-2.42 are the algebraic expressions closing the set of differential equations and solving for ϕ and $\mathbf{u_e}$, recalling electron flow velocity is described in terms of the magnetically confined velocity and a drift component, $\mathbf{u}_e = u_{\parallel e}\mathbf{1}_\parallel + \hat{\mathbf{u}}_e$.

3. NUMERICAL INTEGRATION

The appropriate formulation of the Euler-like physical model to be solved is the defined using conserved variables, density n, momentum $\mathbf{m} = n\mathbf{u}$ and energy $\hat{E}$, as described in the differential ion Eqs. 2.37-2.39. The unknows are functions of $(t, \mathbf{x})$ and take values in $\mathbb{R}^+$, $\mathbb{R}^N$ and $\mathbb{R}^+$, respectively. In this notation, where the expression is fully conservative, the ion equations can be formally written as

$$\frac{\partial \mathbf{Q}}{\partial t} + \nabla \cdot \mathcal{F}(\mathbf{Q}) = \mathcal{R}(\mathbf{Q}) \quad \text{in} \quad \Omega, \tag{3.1}$$

where $\mathcal{O} = \mathbb{R}^+ \times \mathbb{R}^N \times \mathbb{R}^+$, Ω is an open bounded domain in $\mathbb{R}$ and $\nabla \cdot \mathcal{F}(\mathbf{Q}) \equiv \sum_{k=1}^{n} \frac{\partial}{\partial x_k} \mathbf{f}_k(\mathbf{Q})$. Here, $\mathbf{Q}$ is the vector of conserved variables, $\mathbf{f}_k$ the fluxes and $\mathcal{R}$ the right-hand side vector, which are defined as follows,

$$\mathbf{Q} = \begin{pmatrix} n \\ \mathbf{m} \\ \hat{E} \end{pmatrix} \in \mathbb{R}^{N+2}, \tag{3.2}$$

$$\mathcal{F}(\mathbf{Q}) = \begin{pmatrix} \mathbf{m}^\top \\ \frac{\mathbf{m}\otimes\mathbf{m}}{n} + p_e(n) + p_i(n, \mathbf{m}, \hat{E}) \\ (\hat{E} + p_i(n, \mathbf{m}, \hat{E})\frac{\mathbf{m}^\top}{n} \end{pmatrix} \in \mathbb{R}^{(N+2)\times N}, \tag{3.3}$$

$$\mathcal{R}(\mathbf{Q}) = \begin{pmatrix} 0 \\ (\mathbf{1}_\parallel \times \nabla H_e) + n\mathbf{u}_i \times \mathbf{B} \\ n\partial_t \phi \end{pmatrix} \in \mathbb{R}^{N+2}. \tag{3.4}$$

For simplicity, electron pressure is defined as $p_e(n) = n^{\gamma_e}$ and ion pressure as $p_i(n, \mathbf{m}, \hat{E}) = (\gamma_i - 1)\left(\hat{E} - \frac{1}{2}\frac{\|\mathbf{m}\|^2}{n} - n\phi\right)$ with ϕ as defined in Eq. 2.40. Other subindex for species' type have been dropped, as the system is being solved strictly for ion flow conserved quantities. The number of unknowns is $m = N + 2$, depending on the assumption taken for the dimensional space. From the flux matrix, given an arbitrary $\nu \in \mathcal{S}^{N-1}$ we obtain from Eq. 3.3 the Jacobi matrix,

$$\sum_{k=1}^{N} \nu_k \nabla_{\mathbf{Q}} \mathcal{F}_k = \begin{pmatrix} 0 & \nu^\top & 0 \\ -\frac{(\mathbf{m}\cdot\nu)\mathbf{m}}{n^2} + \partial_n p_i\ \nu + \partial_n p_e\ \nu & \frac{\mathbf{m}}{n}\nu^\top + \nu\nabla_{\mathbf{m}} p_i + \frac{\mathbf{m}\cdot\nu}{n} & \partial_E p_i\ \nu \\ -(\hat{E} + p_i)\frac{\mathbf{m}\cdot\nu}{n^2} + \frac{\mathbf{m}\cdot\nu}{n}\partial_n p_i & (\hat{E} + p_i)\frac{\nu^\top}{n} + \frac{\mathbf{m}\cdot\nu}{n}\nabla_{\mathbf{m}} p_i & \frac{\mathbf{m}\cdot\nu}{n} + \frac{\mathbf{m}\cdot\nu}{n}\partial_E p_i \end{pmatrix} \tag{3.5}$$

Notice that, due to the presence of an electron species in the plasma model and its respective pressure contribution, a term accounting for electron pressure gradient, $\partial_n p_e\ \nu$, arises in $\sum_{k=1}^{N} \nu_k \nabla_{\mathbf{Q}} \mathcal{F}_k$. This differentiates the posing of the problem from a typical Euler system configuration, as the system pressure for energy conservation accounts simply for ion pressure.

The notion of hyperbolicity is taken from the textbook by Dafermos [38]. In the reference, a system of conservation laws is considered hyperbolic if for any $\mathbf{Q} \in \mathcal{O}$ and $\nu \in$

$\mathcal{S}^{N-1}$ there exist m real eigenvalues denoted by $\lambda_i(\nu; \mathbf{Q}) \in \mathbb{R}$ of the matrix $\sum_{k=1}^{N} \nu_k \nabla_{\mathbf{Q}} \mathcal{F}_k$, and their respective linearly independent eigenvectors.

Computation of the eigenvalues from Eq. 3.5 is a fundamental step on numerical flux determination, thus an adequate approximation must be taken to fully characterize the velocity of the transport waves. After mathematical rearrangement and numerical corroboration of the outputted results, the expressions governing eigenvalues in a 2-dimensional domain are given by:

$$\lambda_1 = \nu - c_s, \qquad \lambda_{2,3} = \nu, \qquad \lambda_4 = \nu + c_s, \tag{3.6}$$

where c_s is defined as indicated in Eq. 2.36. The determination of the eigenvalues for an hyperbolic system including ions is not trivial, as it does not strictly fall under the typical Euler-like expressions for eigenvalues, mathematical derivation and verification was performed to validate the indicated eigenvalues.

3.1. Finite Volume Method

Finite Volume Methods (FVM) are a set of numerical techniques designed to solve by discretization an existent model in conservative form such as Eq. 3.1. The fundamental principle of FVMs is the subdivision of the spatial domain (i.e. Ω) into a finite number of non-overlapping control elements (volumes or cells) and the enforcement of the conservation principles (i.e., continuity, momentum and energy) over each volume [39].

Finite Volume Methods are specially well-posed to handle discontinuities, which in classical finite difference methods lead to computational difficulties and breaking down of the solution. As indicated, rather than pointwise approximations at grid points, each of the grid elements of the FVM discretisation is assigned a cell average, which is then modified in each time step. This time marching modification will be handled both by a time integration algorithm and a numerical flux function that is able to approximate the adequate fluxes with sufficient accuracy. This last feature makes the FVM an attractive method in problem modeling where flux is of relevance, such as in fluid mechanics, which is the case of the proposed plasma model. Further mathematical insight and literature references for solving nonlinear hyperbolic conservation laws by FVMs has been gathered from Leveque [40].

For the purposes of the present project, the conserved equations in 3.1 will be discretized using a Discontinuous Galerkin (DG) method. Note that for zeroth-order polynomials, the proposed method coincides with the operations performed in a FVM discretization, thus easing optimization of the procedure by reducing mesh size or increasing polynomial order [6].

3.2. Numerical Discretization. Discontinuous Galerkin

In order to formulate the Discontinuous Galerkin approximation for Eq. 3.1, the outlined procedures by Houston [41] and Hartmann [42] are taken as reference. Consider, firstly, the division of the given domain Ω into a mesh $\mathcal{T}_h = \{\kappa\}$ consisting of elements κ.

To complement the given notation, notice that for each $\kappa \in \mathcal{T}_h$, the unit outward normal vector to the boundary $\partial\kappa$ is $\mathbf{n}_k$ and every one of these κ is an image of a fixed reference element $\hat{\kappa}$. Consequently, it may be formally written that $\kappa = \sigma_k(\hat{\kappa})$ for all $\kappa \in \mathcal{T}_h$ [41]. On the reference element $\hat{\kappa}$, let us proceed by defining a series of spaces of polynomials of degree $p \geq 0$ as follows:

$$\mathcal{Q}_p = \text{span}\{\hat{\mathbf{x}}^\alpha : 0 \leq \alpha_j \leq p, 0 \leq j \leq N\}, \qquad \mathcal{P}_p = \text{span}\{\hat{\mathbf{x}}^\alpha : 0 \leq |\alpha| \leq p\}. \tag{3.7}$$

Once the set of polynomials has been defined, the finite element space $\mathbf{V}_p^m(\mathcal{T}_h)$ for the Discontinuous Galerkin method can be described as,

$$\mathbf{V}_p^m(\mathcal{T}_h) = \begin{cases} \mathbf{v} \in [L_2(\omega)]^m : \mathbf{v}|_\kappa \circ \sigma_\kappa \in [\mathcal{Q}_p]^m, & \text{if } \hat{\kappa} = \sigma_\kappa^{-1}(\kappa) \text{ is the unit hypercube,} \\ \mathbf{v}|_\kappa \circ \sigma_\kappa \in [\mathcal{P}_p]^m, & \text{if } \hat{\kappa} = \sigma_\kappa^{-1}(\kappa) \text{ is the unit simplex; } \kappa \in \mathcal{T}_h. \end{cases} \tag{3.8}$$

Before continuing with the method derivation, let us explore the characteristics of interior faces and boundary faces of the partitioned mesh, $\mathcal{T}_h$. An interior face is defined as the (N-1)-dimensional interior of $\partial\kappa^+ \cap \partial\kappa^-$, where κ^+ and κ^- are the two elements of the mesh, which do not necessarily need to match [41]. While the boundary face f is the non-empty (N-1)-dimensional facet of κ, such that $f \subset \partial\kappa \cap \Gamma$. Furthermore, let $\mathbf{v}$ be a smooth valued vector function inside each element $\kappa^\pm$.

To formulate the Discontinuous Galerkin method, let us first introduce a weak formulation of Eq. 3.1. To this end, the aforementioned equation is multiplied by the arbitrary smooth vectorial function $\mathbf{v}$ and integrated by parts over an element κ in the mesh $\mathcal{T}_h$, as shown in Eq. 3.9.[5]

$$\int_\kappa \mathbf{v} \cdot \frac{\partial \mathbf{Q}}{\partial t} d\mathbf{x} - \int_\kappa \mathcal{F}(\mathbf{Q}) : \nabla \mathbf{v} d\mathbf{x} + \int_{\partial\kappa} \mathbf{v}^+ \cdot \mathcal{F}(\mathbf{Q}^+)\mathbf{n}_\kappa dS = \int_\kappa \mathbf{v} \cdot \mathcal{R}(\mathbf{Q}) d\mathbf{x}. \tag{3.9}$$

Notice that the derived weak formulation may be applicable for an arbitrary element in the mesh, thus it is now possible to replace the analytical solution $\mathbf{Q}$ and the test function $\mathbf{v}$ with the Galerkin finite element approximations $\mathbf{Q}_h$ and $\mathbf{v}_h$, respectively. Additionally, due to the discontinuous nature of the numerical solution $\mathbf{Q}_h$, it is imperative to substitute the considered flux function by the numerical flux depending on the inner and outer traces and the outward normal vector [42],

$$[\mathcal{F}(\mathbf{Q})\mathbf{n}_\kappa]_h \rightarrow \mathcal{H}(\mathbf{Q}_\mathbf{h}^+, \mathbf{Q}_\mathbf{h}^-, \mathbf{n}_\kappa). \tag{3.10}$$

[5] Additional insight on admissible and relevant weak formulations for a certain system set-up and particularly for full Euler-like configurations may be found in Markfelder [43].

This convective numerical flux term will be chosen to be any two-point monotone Lipschitz function which is both consistent and conservative [42]. Further details on the implemented flux will be indicated eventually. Let us first close the discontinuous Galerkin discretisation by summing over all the elements κ in the mesh $\mathcal{T}_h$, then find $\mathbf{Q}_h$ in the finite element space $\mathbf{V}_p^m(\mathcal{T}_h)$.

$$\mathcal{N}(\mathbf{Q_h}, \mathbf{v_h}) \equiv \sum_{\kappa \in \mathcal{T}_h} \left\{ \int_\kappa \mathbf{v}_h \cdot \frac{\partial \mathbf{Q}_h}{\partial t} d\mathbf{x} - \int_\kappa \mathcal{F}(\mathbf{Q}_h) : \nabla \mathbf{v}_h d\mathbf{x} + \int_{\partial\kappa} \mathcal{H}(\mathbf{Q}_h^+, \mathbf{Q}_h^-, \mathbf{n}_k) \mathbf{v}_h^+ dS \right.$$
$$\left. - \int_\kappa \mathbf{v}_h \cdot \mathcal{R}(\mathbf{Q}_h) d\mathbf{x} + \int_\kappa \varepsilon \nabla \mathbf{Q}_h \cdot \nabla \mathbf{v}_h d\mathbf{x} \right\} = 0 \tag{3.11}$$

In the previous equation, observe that a term which was not present in Eq. 3.9 arised. The presence of this term accounts for the artificial viscosity model, where ε denotes the artificial viscosity coefficient defined by,

$$\varepsilon = C_\varepsilon h^{2-\beta} |\nabla \mathcal{F}(\mathbf{Q}_h)| I. \tag{3.12}$$

In Eq. 3.12, C_ε and $0 < \beta < 1/2$ are positive constants and I denotes the identity matrix in $\mathbb{R}^N$.

3.3. Numerical Flux Function. Local Lax-Friedrichs

As denoted in Eq. 3.10, discretisation of the convective flux function $\mathcal{F}(\mathbf{Q})$ involves defining a numerical flux function $\mathcal{H}(\mathbf{Q}^+, \mathbf{Q}^-, \mathbf{n}_\kappa)$ on the element boundaries. As previously introduced, the the numerical flux may be chosen to be any two-point monotonic Lipschitz function which is conservative, $\mathcal{H}(\mathbf{Q}^-, \mathbf{Q}^+, \mathbf{n}_\kappa) = \mathcal{H}(\mathbf{Q}^+, \mathbf{Q}^-, \mathbf{n}_\kappa)$, and consistent, $\mathcal{H}(\mathbf{Q}, \mathbf{Q}, \mathbf{n}_\kappa) = \mathcal{F}(\mathbf{Q})\mathbf{n}_\kappa$, as indicated in [42].

There are numerous numerical fluxes that satisfy the aforementioned conditions, such as the Godunov, the HLLE, the Vijayasundaran or the Roe fluxes, for example. Nevertheless, for the purposes of the described project the Local Lax-Friedrichs flux is implemented as indicated in [44], aiming for a balance in flux computation accuracy and model formulation simplicity. The local Lax-Friedrichs flux may be defined as follows,

$$\mathcal{H}_{LF}(\mathbf{Q}^-, \mathbf{Q}^+, \mathbf{n}_\kappa)|_{\partial\kappa} = \{\{\mathcal{F}(\mathbf{Q}_h)\}\} + \frac{\alpha}{2}[[\mathbf{Q}_h]], \tag{3.13}$$

where $\{\{\mathcal{F}(\mathbf{Q}_h)\}\}$ is the average of the interior value $\mathbf{Q}_h^-$ and the exterior value $\mathbf{Q}_h^+$, $[[\mathbf{Q}_h]]$ is the jump between the two states and α is the local dissipation parameter. These are written as,

$$\{\{\mathcal{F}(\mathbf{Q}_h)\}\} = \frac{\mathcal{F}(\mathbf{Q}_h^-) + \mathcal{F}(\mathbf{Q}_h^+)}{2} \qquad [[\mathbf{Q}_h]] = \mathbf{n}_\kappa^- \mathbf{Q}_h^- + \mathbf{n}_\kappa^+ \mathbf{Q}_h^+ = \mathbf{n}_\kappa^- (\mathbf{Q}_h^- - \mathbf{Q}_h^+) \tag{3.14}$$

Substituting these expressions in Eq. 3.13 results in

$$\mathcal{H}_{LF}(\mathbf{Q}^-, \mathbf{Q}^+, \mathbf{n}_\kappa)|_{\partial\kappa} = \frac{\mathcal{F}(\mathbf{Q}_h^-) + \mathcal{F}(\mathbf{Q}_h^+)}{2} + \frac{\alpha}{2} \mathbf{n}_\kappa^- (\mathbf{Q}_h^- - \mathbf{Q}_h^+). \tag{3.15}$$

The dissipation parameter α is selected to be the maximum absolute value of the eigenvalues of the Jacobi matrix $J(\mathbf{Q}, \mathbf{n}_\kappa)$ defined in Eq. 3.5 evaluated on the element face. Consequently, α stands for

$$\alpha|_{\partial\kappa} = \max_{\mathbf{w}=\mathbf{Q}_h^+,\mathbf{Q}_h^-} \{|\lambda_{\max}(J(\mathbf{w}, \mathbf{n}_\kappa))|\}. \tag{3.16}$$

3.4. Boundary Conditions

Similarly to the discretisation method implemented for faces inside the domain, recall the existence of boundary faces f, defined for elements κ whose boundary intersects that of the considered domain Ω. These will be generally denoted as Γ such that $f \subset \partial\kappa \cap \Gamma$. As indicated in the weak form 3.9, the same numerical flux will be implemented, thus assuming weakly imposed boundary conditions, defined by the interior solution $\mathbf{Q}_h^-$ and an exterior value $\mathbf{Q}_h^+$ in additional cells positioned adjacent to the domain, receiving the name of ghost cells. The external boundary is generally[6] decomposed in Γ_{in}, Γ_{out} and Γ_{sym}, which account for inflow, outflow and symmetry planes, respectively.

- For inflow conditions, the exterior value $\mathbf{Q}_h^+$ is defined such that it models the desired inflow function g,

$$\mathbf{Q}_h^+ = g \quad \text{for } \partial\kappa \cap \Gamma_{in}. \tag{3.17}$$

- For the supersonic outflow boundary, where no information is given, the exterior value $\mathbf{Q}_h^+$ is that of the interior of the domain $\mathbf{Q}_h^-$ [6],

$$\mathbf{Q}_h^+ = \mathbf{Q}_h^- \quad \text{for } \partial\kappa \cap \Gamma_{out}. \tag{3.18}$$

- Finally, for the symmetry plane Γ_{sym}, the density, parallel flux components and energy of $\mathbf{Q}_h^+$ are set as those of $\mathbf{Q}_h^-$, while zero perpendicular flux is imposed [6]. Parallel and perpendicular notions are taken with respect to the outeard normal vector $\mathbf{n}_\kappa$.

3.5. Time Integration

Once mesh discretisation is defined by the Discontinuous Galerkin method and local Lax-Friedrichs numerical flux is imposed, the problem is now conditioned to be initially integrated in time. To perform this operation, a Strong Stability Preserving Runge Kutta scheme, as the one detailed in [45], will be implemented.

[6] For some particular simulations, i.e., three-dimensional geometry of the device, an additional boundary condition accounting for azimuthal rotation of species may need to be introduced to reduce computational expenses.

The equation defining the approximate solution after inverting the "mass" matrix can be rewritten in ODE form as:

$$\frac{d}{dt}\mathbf{Q}_h = L_h(\mathbf{Q}_h) \tag{3.19}$$

If a finite element space $\mathbf{v}_h$, included in $\mathbf{V}_p^m(\mathcal{T}_h)$, is being used; the system of ODEs is ought to be discretized in time introducing a (p+1)th-order accurate Runge Kutta method. This limiting value is established as an acceptable minimum. For the purposes of the simulations developed in the present research, a third-order accurate Runge-Kutta scheme will be sufficient for piecewise linear and piecewise quadratic finite element approximations. Thereby, let us introduce the notation[7] for time partitioning, where $\{t^n\}_{n=0}^N$ is a partition of $[0, T]$ and $\Delta t^n = t^{n+1} - t^t;\ n = 0, ..., N-1$. Taking this into consideration, the time integration algorithm is implemented as follows,

1. Set initial conditions for time integration, $\mathbf{Q}_h^0$. Any gross approximation of the subsequent step may be used [45].

2. For $n = 0, ..., N-1$ compute $\mathbf{Q}_h^{n+1}$. The steps to obtain this value are the following:

   (a) Set $\mathbf{Q}_h^{(0)} = \mathbf{Q}_h^n$,

   (b) for i = 1,...,p+1 (in the particular assumption that a third order RK is being used $p + 1 = 3$) compute the intermediate functions:

   $$\mathbf{Q}_h^{(i)} = \left\{ \sum_{I=0}^{i-1} \alpha_{iI}\mathbf{Q}_h^{(I)} + \beta_{iI}\Delta t^n L_h\left(\mathbf{Q}_h^{(I)}\right) \right\}. \tag{3.20}$$

   (c) Finally, set $\mathbf{Q}_h^{n+1} = \mathbf{Q}_h^{(p+1)}$.

Parameters α_{iI}, β_{iI} and d_I are gathered from the ones defined in [45].

After a sufficient amount of steps, and once the solution is close enough to the expected simulation results, the system may be solved for steady-state. The time marching algorithm is essentially performed to speed up convergence of the steady state solution, as a gross approximation of the expected output needs to be introduced to solve the non-linear system of equations.

There is still one parameter whose magnitude has not yet been defined, and its scale will be highly relevant for time integration convergence and proper functioning of the RK method; this is the time step, Δt^n. The time step in a Discontinuous Galerkin discretization using a third order Runge-Kutta method is constrained by the Courant-Friedrichs-Lewy (CFL) condition. The CFL condition ensures numerical stability by limiting the time step on the spatial discretization and wave propagation speed, so that

$$\Delta t \leq \frac{C}{\lambda_{\max}}, \tag{3.21}$$

[7] Notice that notation for time partitioning introduces variables n and N, which account for specific time step and total number of time divisions, respectively. These variables coincide with density and dimensional domain of the model, however, their definition is modified to the stated just for the time discretisation case.

where C is a stability coefficient depending on the RK scheme and polynomial degree and $\lambda_{\max}$ is the maximum wave speed in the system as defined in Eq. 3.16. Substituting by known variables, it has been determined that the optimum CFL condition establishes a time step given by,

$$\Delta t = \frac{1}{(p+1)} \frac{h}{(M_{i0}+1)} \tag{3.22}$$

where the expression depends on the DG polynomial degree p, the size of the mesh elements h, and the initial mach ion number M_{i0}.

3.6. POSETS-v2: Plume SOlver for Electrodeless Thruster Systems - Version 2

The plasma physical and numerical model described in Chapters 2 and 3, respectively, have been integrated into a python-based code for the simulation of the plasma expansion along the divergent region of MAs. POSETS-v2 takes the POSETS framework code developed by Diego García-Lahuerta as part of the ERC-ZHARATHUSTRA project and implemented for Merino 2023 [6], and introduces a series of relevant updates that allow for further and more sophisicated physical analysis of plasma expansion and plume characterization. Similarly to the original version, POSETS-v2 is built upon the FEniCS library, a powerful open-source framework for solving partial differential equations (PDEs) using the finite element method (FEM). The core of POSETS-v2 implements FEniCS for mesh generation, function spaces definition, and weak formulation handling, which coupled with the time integration methods described in Chapter 3 emable the precise numerical solution of the complex Euler-like hyperbolic plasma equations described in Chapter 2. Among POSETS-v2 updates, major sophistications include the following:

- Introduction of total and internal ion energy conservation effects as defined by 2.39. This sophistication enables modeling of complete ion thermodynamics and non-negligible temperature conditions, unveiling physical phenomena left out by cold-ion approximations. Thereby, intricate mechanisms and formulation of ion acoustic waves (IAWs) are adequately solved for and represented.

- Convergence improvement by redefinition of FEniCS Function Space for precomputed variables, including magnetic field conditions. B_a and ψ_B, and electron-related properties, H_e and u_{ye}. From being defined in a second order Continuous Galerkin space, conversion to a Discontinuous Galerkin space matching the order of the solution space considerably reduces convergence time.

- Error fix in boundary conditions imposition. Previous version presented considerable relative error between imposed boundary conditions through ghost cells and resultant simulation values, which have been mitigated in POSETS-v2.

- POSETS-v2 allows for three-dimensional magnetic field computation from a set of circular coil loops of current intensity I_w, and solving of 3D plasma expansion

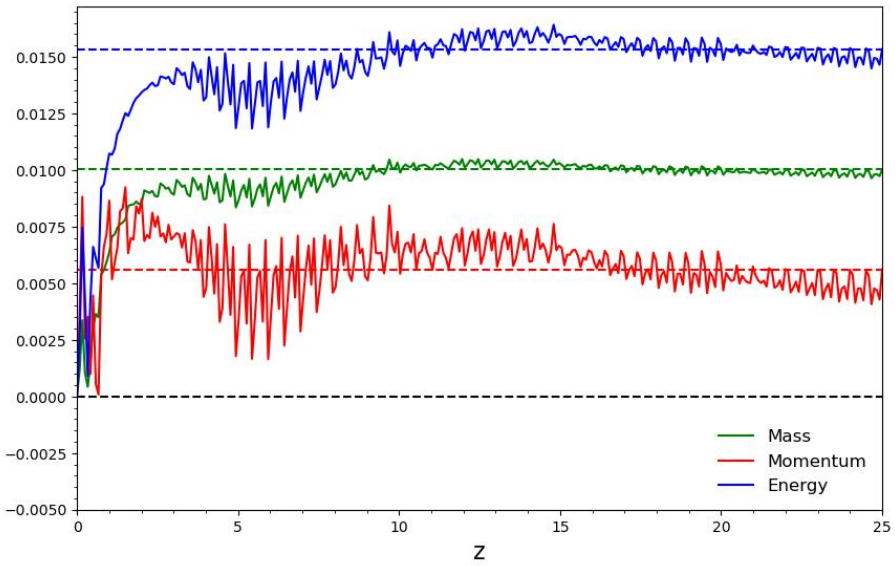

Fig. 3.1. Numerical integrals for conserved properties along control volume defined by z-coordinate: mass, momentum in z-direction and ion energy.

simulations. This offers the possibility of full characterization of the influence of azimuthal flow of species (i.e. u_{yi}) and evaluation of the effects of into-the-plane magnetic field strength B_y.

3.7. POSETS-v2 Code Verification

A fundamental consideration on POSETS-v2 is its verification as fully working module. A convenient method for validation and verification is testing property conservation (i.e. mass, momentum and energy). Thereby, integral expressions for conservation laws are integrated numerically along the solution grids to evaluate simulation accuracy. The expectation is that continuity, momentum and energy integral equations converge to zero, as these are equivalent to the system of hyperbolic differential equations solved for. The implemented expressions read as,

$$\int_{\partial\Omega} n\mathbf{u}_i \cdot \mathbf{1}_n dS = 0, \tag{3.23}$$

$$\int_{\partial\Omega} n\mathbf{u}_i(\mathbf{u}_i \cdot \mathbf{1}_n)dS + \int_{\partial\Omega} p_e \cdot \mathbf{1}_n dS + \int_{\partial\Omega} p_i \cdot \mathbf{1}_n dS = \int_{\Omega} \mathbf{F}(z)d\Omega, \tag{3.24}$$

$$\int_{\partial\Omega} (\hat{E} + p_i)\mathbf{u}_i \cdot \mathbf{1}_n dS = 0. \tag{3.25}$$

Simulation in Chapter 4 is to be used for validation, hence, additional details on model setup and selected boundary conditions may be gathered in the sections that follow. Fig. 3.1 depicts the conservation curves with respect to a z-coordinate that defines the integrated control volume, computed from Eqs. 3.23-3.25.

As can be observed, the bulk of the error is mainly concentrated on the near expansion

region, close to the thruster's throat. While the following downstream expansion does not accumulate major error apart from background noise. The sources of the noticeable deviation from the expected conservation arise due to a series of factors, including:

- *Local Lax-Friedrich dissipation.* The Lax-Friedrichs method introduces artificial dissipation to stabilize numerical solutions, particularly when applied for hyperbolic conservation laws as is the case. This additional dissipation ensures robustness of the solution process but comes at the cost of accuracy. In the near expansion region ($z = 0$ to $z = 5$ of Fig. 3.1), where rapid variations in plasma properties occur, this artificial smoothing may supress finer details, leading to the accumulation of deviations from the expected conservation properties. This effect is also appreciable when computing the entropy evolution of the system, discusses in Section 4.4 and depicted in Fig. 4.12.

- *Error due to density cut-off imposition.* In order to avoid instabilities related to near-zero values, a minimum density threshold has been imposed. Enforcing density cut-off prevents from small scale density fluctuations but may introduce discrepancies in the computed plasma flow evolution.

  This imposition, which is particularly applied at local zones over and under the edges of the thrusters, where the plasma-vacuum transition is abrupt, impedes absolute conservation of properties, hence resulting in accumulation of error in the near expansion region.

- *Grid transformation induced error.* Grid transformation is applied to map the *Fenics* solved function to a manageable format, which is then integrated to determine conservation. Near the thruster's throat, where plasma properties change rapidly, grid warping or numerical interpolation artifacts may lead to distortions in computed values. Additionally, this errors propagate downstream and may arise in the form of background noise error, as seen in Fig. 3.1.

4. LOW ION TEMPERATURE MA EXPANSION SIMULATION

By using the physical and numerical models formulated in Chapters 2 and 3, and particularizing the presented equations to a two-dimensional domain, the properties of the supersonic acceleration of a low-beta, collisionless plasma in a MA may be studied. For computational simplicity, half MA will be modeled, with the contribution of the complementary half introduced by a symmetry boundary condition.

The presented simulation for low temperature ions (cold species approximation), with $T_{i0}/T_{e0} = 0.01$, is intended to serve as a model comparison to Merino 2023 [6]. Previous work and simulations solve the Euler-like plasma general equations by excluding the energy conservation relation, either by assuming the presence of cold ions or by imposing adiabatic relations for its temperature[8]. The simulation studied in [6] assumes negligible ion temperature and disregards the contribution and effects of the energy conservation equation, thus ignoring ion cooling mechanism, gasdynamic acceleration and, consequently, the appearance of possible ion acoustic waves and basic ion-electron thermodynamic interaction of the plasma plume.

The purpose of the subsequent Sections is to provide a sophisticated plasma model that fully characterizes a particular case of MA plasma expansion including ion thermodynamics, and identifies potential differences and errors deriving from the cold-ion assumption.

4.1. Description of the Simulation and Boundary Conditions

A single simulation resembling the input parameters and dimensions of that in Merino's 2023 [6] article will be investigated to characterize the influence of ion thermodynamics. The values of the dimensional parameters and simulation set-up are summarized in Table 4.1. The implemented non-uniform mesh, depicted in Fig. 4.1[9], has been constructed from the map of H_e to account for high precision at near throat regions, MA centerline and plume domain, while relaxing cell dimensional parameters downstream and radially outward (strictly vacuum regions).

The applied magnetic field used for the simulation presented is generated by four identical wires contained in the O_{xy} plane, equivalent to the use of axis-symmetric magnetic coil loops, located at $x = 3, 7, -3, -7$. The thruster outlet in the simulated half of the MA is located as well on the O_{xy} plane and goes from $x = 4$ to $x = 6$. As observable, the geometrical centers of the current wires and the thrusters outlet coincide, with their radius being $R_w = 2$ and $R_t = 1$, respectively.

[8] Similarly to the polytropic assumptions made for electron temperature distribution shown in Eq. 2.3.

[9] The final simulated mesh underwent two fenics-integrated refinement processes, thus the displayed mesh layout coincides but its final cell dimensions were diminished, increasing accuracy.

TABLE 4.1. MA SIMULATION (T_{I0} = 0.01) SETUP CHARACTERISTICS

Mesh Characteristics		**Applied Magnetic Field**		**Thruster Outlet**	
Mesh l_z	25	R_w	2	R_t	1
Mesh l_x	15	C_w	x = 5, -5	C_t	x = 5, -5
Mesh size h	0.0942	L_{w1}	x = 3, -3	L_{t1}	x = 4, -4
Polynomial p	1	L_{w2}	x = 7, -7	L_{t2}	x = 6, -6

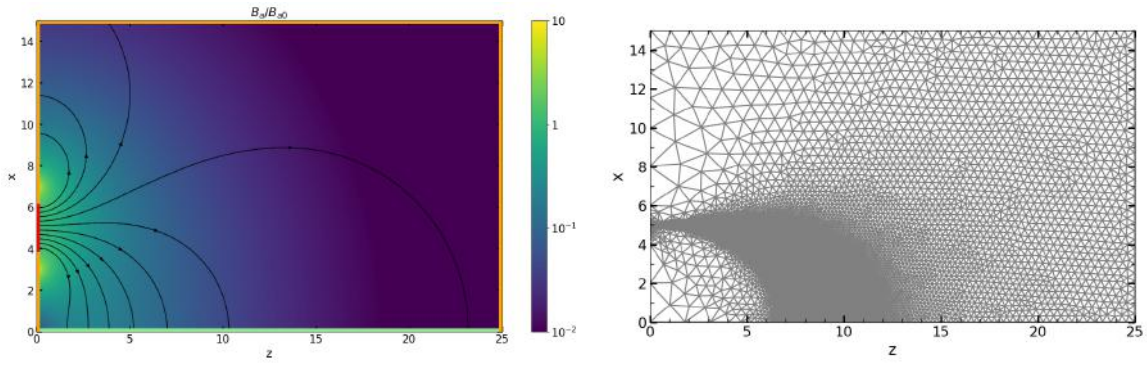

Fig. 4.1. On the left, applied magnetic field (a) generated by axis-symmetric magnetic coil loops located at $x = 3, 7, -3, -7$. Magnetic streamtubes are represented as arrowed black lines. On the right, non-uniform mesh (b) constructed from the map of H_e, prior refinement.

The dimensionless ion gyrofrequency Ω_{i0} is an important parameter for the ion flow evolution, as it governs the intensity of the magnetic force on ions. Ω_{i0} coincides numerically with the dimensionless factor for magnetic field strength, B_0. The normalized magnetic field at the center of the thruster outlet $C_t = (0, 5)$ is then set to $B_0 = 1$, which accounts for a mild initial ion magnetization.

The plasma properties at the MA throat need to be inputted to simulate the expansion; namely, it is required to provide profiles for the density n, the velocity vector $\mathbf{u_j}$ of each species, the ion energy $\hat{E}_i$ (by defining a convenient T_i profile), and the electric potential ϕ. These properties are highly dependent on the plasma source located upstream. Boundary conditions are imposed in the model for each of the solved variables via numerical fluxes across ghost-cells adjacent to the domain boundaries. Differently from solution-defined boundary conditions, these fluxes may experience numerical dissipation that can modify the expected solution slightly, thus verification of appropriate behavior is required to validate the simulation. Additionally, recall that the inputted profile is typically Gaussian (Eq. 4.1), and due to the nature of DG approximation, the function will be introduced with the selected polynomial degree.

The inputted and solution resultant throat conditions are displayed in Fig. 4.2, where a sufficiently precise resemblance is observed with minor deviations from the expected values.

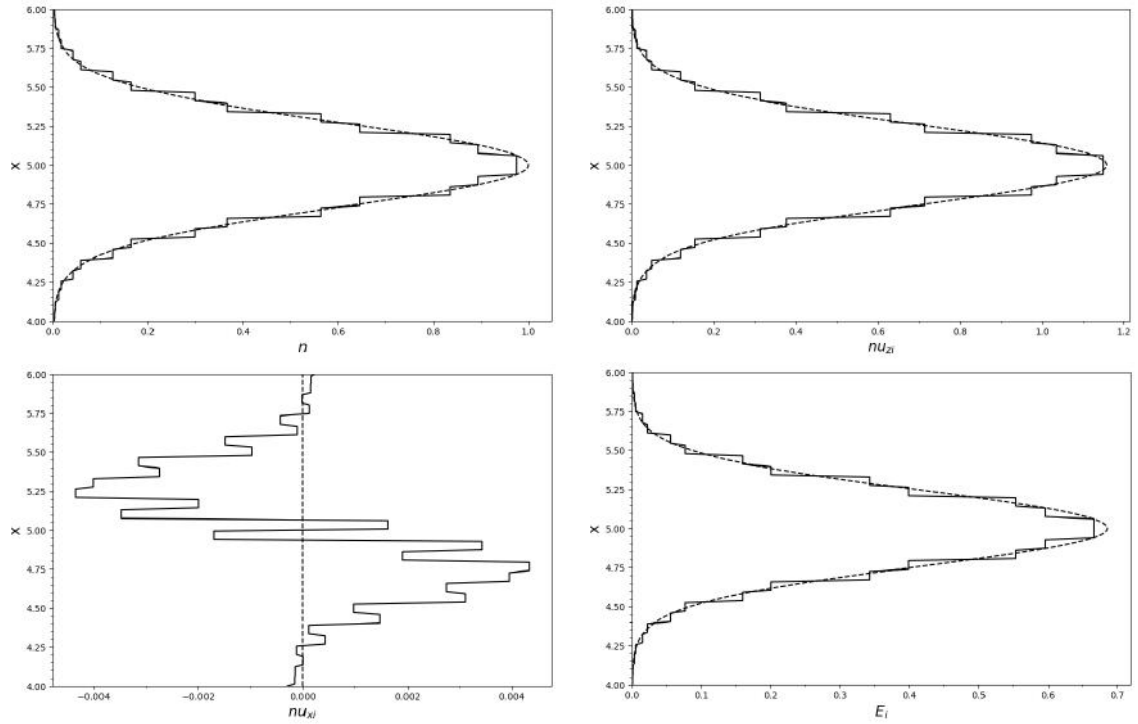

Fig. 4.2. Weakly imposed boundary conditions profile for density n (a), z-directed ion current j_{zi} (b), x-directed ion current j_{zi} (c) and ion energy $\hat{E}_i$ (d) (discontinuous black lines). Solution retrieved conditions at thruster's throat (continuous black lines).

In this particular case, radial profiles[10] of the aforementioned quantities will be imposed at section $z = 0$ and $C_t - R_w \leq x \leq C_t + R_w$. Note that for H_e and $\partial H_e/\partial\psi$ computation purposes, the boundary conditions are extended to the magnetic field generators.

Plasma density profile is assumed Gaussian, centered on C_t and falling three orders of magnitude at the edges of the thruster's outlet:

$$n(0, x) = 10^{-3(\frac{x-C_t}{R_t})^2}. \tag{4.1}$$

Continuing with injection of the ion flow currents through the thruster's outlet, unless otherwise stated, ions are injected purely axially into the MA, with

$$u_{zi}(0, x) = M_{i0}c_s(0, x), \qquad u_{xi}(0, x) = 0, \qquad u_{yi}(0, x) = 0, \tag{4.2}$$

where c_s is defined as indicated in Eq. 2.36, adding both the thermodynamic contribution of ions and electrons. M_{i0} is the initial injection Mach number, set to $M_{i0} = 1$ to account for sonic in-plane ion flow at the throat.

Regarding energy boundary conditions, for convenience and ease in physical interpretation, these are defined from a preimposed ion temperature radial profile. Let us first

[10]Due to the axis-symmetry of the model, x-direction and coordinate may be understood as a radial component in a cylindrical based reference system.

introduce the ion-electron temperature factor, $F_{T_0} = T_{i0}/T_{e0}$, which helps in providing a simple comparison between the energetic state of the species. To account for nearly cold ions, $F_{T_0} = T_{i0} = 0.01$, so that $T_i \ll T_e$ and, thereby, $T_i \ll 1$. The initial radial ion temperature profile will be given by the isentropic relation:

$$T_i(0,x) = T_{i0} n(0,x)^{\gamma_i - 1}, \qquad p_i(0,x) = n(0,x) T_i(0,x), \tag{4.3}$$

where $\gamma_i = 5/3$, a value commonly found empirically in plasma expansions.

From the definition of $\hat{E}_i$ in Eq. 2.33, energy profile is expressed as,

$$\hat{E}_i(0,x) = \frac{1}{\gamma_i - 1} p_i(0,x) + \frac{1}{2} n(0,x) \|\mathbf{u}_i(0,x)\|^2 + n(0,x)\phi(0,x). \tag{4.4}$$

Notice that the electrostatic potential profile which arises in Eq. 4.4 has not yet been defined. In Merino's article, ϕ's profile is initially described as null, however, with the introduction of a non-negligible ion thermal energy, which accounts for the total thermal energy od the system, the ion flow tends to expand radially due to a force imbalance, accelerating divergence of the plume and counteracting thrust generation. As mentioned, an equilibrium could be achieved, in principle, by and azimuthal ion drift, similar but opposite to the electron drift, or by a radial electric field. Thereby, the distribution of electrostatic potential may be adjusted to control the expansion and counteract the thermal energy carried by ions, thus avoiding radial expansion at the throat. Nevertheless, it is worth mentioning that at low ion temperatures, the additional thermal energy does not pose an excessive expansion issue and ϕ may still be maintained null. The ambipolar electrostatic potential outlet profile is given by,

$$\phi(0,x) = -T_{i0} \frac{\gamma_i}{\gamma_i - 1} \cdot n(0,x)^{(\gamma_i - 1)} \approx 0. \tag{4.5}$$

Expression 4.5 will gain relevance in simulations at which thermal ion energy is equivalent to that of ions or it dominates the expansion (i.e. Chapter 5).

Finally, electron flow velocities need to be defined for throat conditions. At the outlet boundary, no x-directed electric field is to exist, $u_{xe} = 0$, resulting in currents only along the parallel direction to the magnetic field and along the y-direction. This way electron pressure and electron magnetic force are in balance. Recalling Eq. 2.24 and Eq. 2.25, the electron inlet flow is expressed as,

$$u_{\|e}(0,x) = u_{ze}(x,0) = \begin{cases} 0 & \text{for } \psi_B < 0 \\ U_{\|e} & \text{for } \psi_B \geq 0 \end{cases} \qquad u_{ye}(0,x) = \frac{1}{B_z} \frac{\gamma_e}{\gamma_e - 1} \frac{\partial n^{\gamma_e - 1}}{\partial x}. \tag{4.6}$$

The electron polytropic exponent is set to $\gamma_e = 1.2$[11], a value commonly found empirically in MNs [46][35].

[11] Unless otherwise specified for electron cooling parametric analysis purposes.

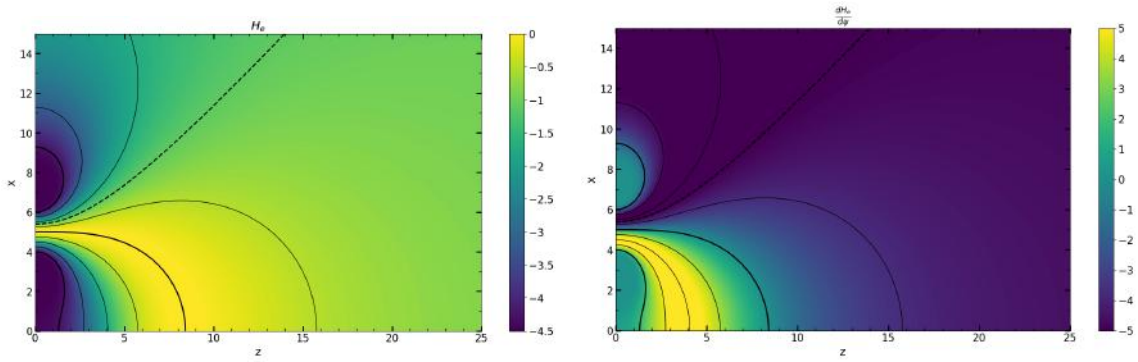

Fig. 4.3. Dimensionless H_e function (a) and $\partial H_e/\partial\psi$ accounting for into-the-plane electron velocity $u_{ye} = -\partial H_e/\partial\psi$ (b) resulting from applied magnetic field and inlet boundary conditions.

4.2. Plasma Expansion and Acceleration

Let us begin the analysis by studying the resultant distribution of the *a priori* computed variables, as these will highly determine the evolution of the species' flow. Both $He(\psi_B)$ and its derivative $\partial H_e/\partial\psi_B$ play a fundamental role in the plasma response to the magnetic field, fixing the electron out-of plane current, $nu_{ye} = -n\partial H_e/\partial\psi_B$, resulting in the electron magnetic force [6]. These magnitudes differ little at negligible ion thermal energy contributions from those derived at cold-ion simulations (Merino 2023 [6], Figure 3), as the necessary imposed throat electrostatic potential to compensate radial forces is negligible. This is not the case for ion thermal dominant simulations, in which H_e's dependence on ϕ alters its evolution downstream (Chapter 5).

Fig. 4.3 show the profile of H_e and $\partial H_e/\partial\psi$ that follow from the imposed boundary conditions at the thruster. Magnetic lines are included in the plots for reference. Thin black lines correspond to streamtubes, thicker black lines to edges and central source streamtubes, and dashed black line to separatrix ($\psi_B = 0$). In contrast with typical MN configurations, the magnitude of the out-of-plane electron velocity takes positive values above the magnetic centerline and negative values below that same limiting line, due to the presence of symmetrically placed magnetic nozzles [6]. The resulting effect is consistent with what is observed in single MNs, a confinement of the expanding electrons to magnetic stream tubes.

Once the algebraically-computed variables are determined and a sufficiently accurate time-stepping integration procedure is performed, the steady-state non-linear hyperbolic system of equations may be solved for. This results in the characterization of the plasma solutions shown in Fig. 4.5, respectively for density n (a), electrostatic potential ϕ (b), in-plane ion velocity $\tilde{\mathbf{u}}_i$ (c) and ion Mach number M_i (d).[12] Thermodynamic-related variables, such as species thermal energy and pressure, are discussed in Section 4.4.

[12]The represented variables and figures are comparable to those in Figure 4 in Merino 2023.

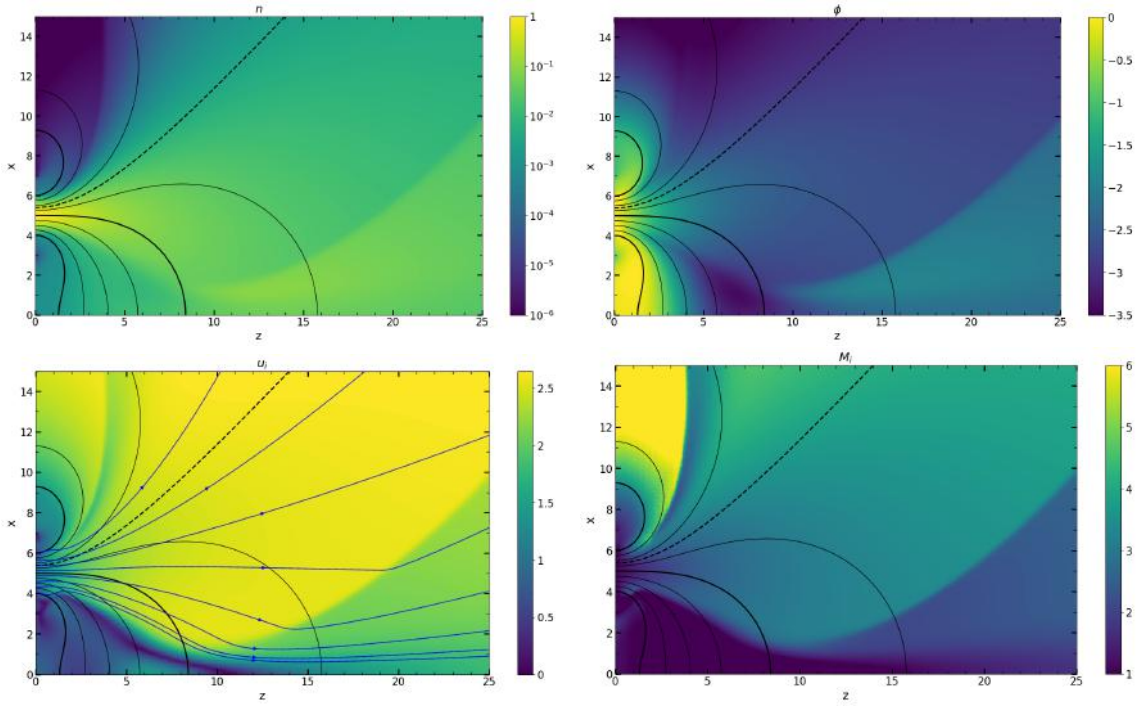

Fig. 4.4. Dimensionless plasma density n (a), electrostatic potential ϕ (b), in-plane ion macroscopic flow velocity $\tilde{\mathbf{u}}_i$ (c) and in-plane ion Mach number M_i (d). Selected ion streamlines originating at the thruster's throat are represented as arrowed blue lines on (c) for trajectory reference.

On an initial basis, plasma response is qualitatively similar to that in Merino 2023 [6], with an expansion guided by the magnetic streamtubes at the thruster's outlet and a subsequent species separation, due to ion acceleration and inertia. In the region surrounding the throat, plasma solution is highly dependent on boundary inlet conditions, taking largest density values along the throat's centerline defined by $n(0, C_t) = O(1)$, which then decay downstream and fall around two orders of magnitude. Along this first fraction of the domain, both the plasma density and electrostatic potential (Fig. 4.5(a) and Fig. 4.5(b)) decrease radially across the upper half of the magnetic nozzle[13], conforming a rarefaction at nearly model-vacuum conditions at the edge of the plasma jet beam. Nevertheless, density and potential magnitudes at the radial expansion across the lower half of the nozzle, towards the symmetry plane, do not decay as rapidly, which poses a major difference with respect to results shown in Fig. 4.4 (a), gathered from Merino 2023 [6]. To assess the cause of the observed phenomenon, let us detail the origination of the observed shock structures.

Closer to the symmetry plane, where ion flow from the upper and lower magnetic nozzles collide, two oblique shock structures form and expand in opposite directions. The oblique shock arising at an approximate coordinate $(x, z) \approx (10, 0)$ and expanding radially downstream was also present in the simulation performed by Merino 2023 and has not

[13]Referred to the represented and solved thruster of the magnetic arch, contained in the considered domain, above the symmetry plane.

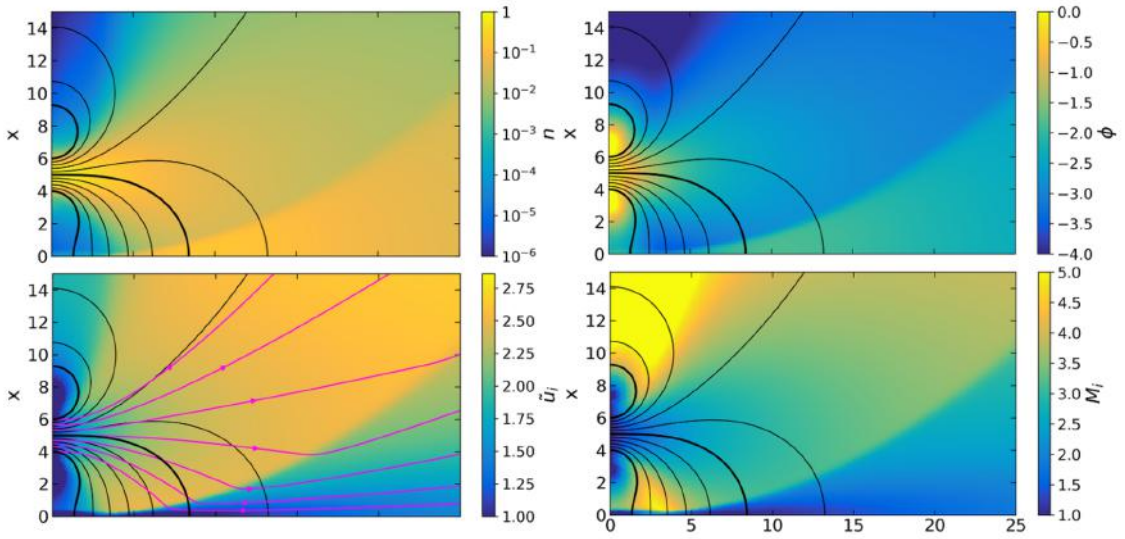

Fig. 4.5. Dimensionless plasma density n (a), electrostatic potential ϕ (b), in-plane ion macroscopic flow velocity $\tilde{\mathbf{u}}_i$ (c) and in-plane ion Mach number M_i (d). Figures taken from Merino 2023, [6].

experienced major modifications in behavior apart from a slight forward deviation, due to the presence of a second oblique shock. This indicates that the commented structure originates from kinetic factors and ion streamline encounters and its effect is enhanced by the introduction of ion thermodynamics. The second shock structure originating at $(x, z) \approx (10, 0)$, however, presents a radial expansion upstream, towards the inlet boundary and can be clearly identified in Fig. 4.5(c). This new shock does appear because of ion thermal energy consideration in the model (Eq. 2.39), and its influence appears to be stronger in terms of discontinuity compared to the former. Even though the shock flux advances towards the inlet, weakly imposed conditions are not altered at the throat.

The shock structures lead to a rise in n and ϕ across the discontinuity limit, which explains the region of non-negligible ion density below the centerline of the nozzle. From the acceleration perspective, in-plane $\tilde{\mathbf{u}}_\mathbf{i}$ and M_i fall across the shock waves, deflecting ion streamlines. The upstream-directed shock structure is, however, not crossed by any of the selected streamlines, but still reduces in-plane velocity to nearly static values, mainly at the shock's boundary. Regarding M_i, computed as $M_i = \|\tilde{\mathbf{u}}_i\|/c_s$, its magnitude experiences a sudden drop but flow remains supersonic ($M_i \geq 1$). The downstream-directed oblique shock is crossed by ion streamtubes, deflecting these upwards and detaching them from the closed magnetic field lines. Mach number follows a similar evolution across the wave, maintaining its supersonic condition.

Let us continue the analysis downstream, where the area of the plasma beam expands gradually as ions detach, ion population cools down and flow accelerates; mainly due to the presence of the electrostatic potential, displayed in Fig. 4.5(b). The evolution of the ambipolar electric potential ϕ shows an interesting phenomena: it does not decrease logarithmically to infinity, as would be the case for isothermal models, instead it is determined

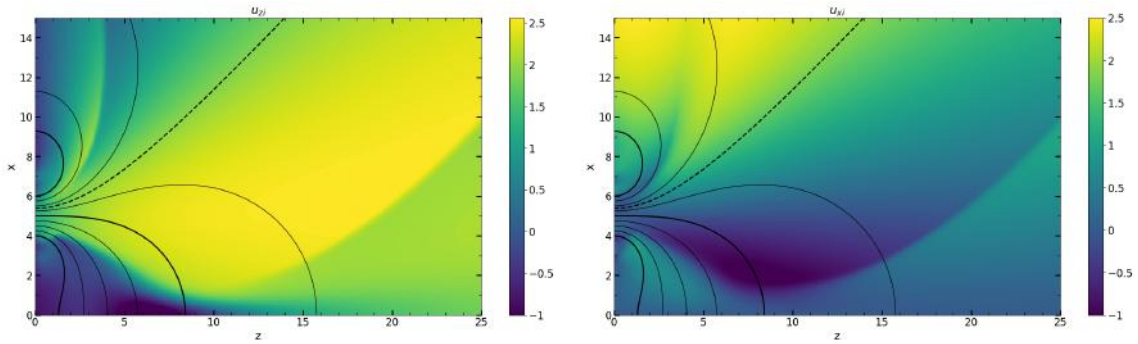

Fig. 4.6. Dimensionless axial (z-directed) and radial (x-directed) ion flow velocity components, u_{zi} (a) and u_{xi} (b), contributing to total in-plane macroscopic fluid velocity.

that an asymptotic value is reached at far regions, as proved in [35] and as given by Eq. 2.23. This imposes an upper bound for ion velocity, since $u_i \propto (-\phi)^{1/2}$, and taking into consideration flow speed grows at a lower rate than in the isothermal limit, there is a M_i increase at a faster rate, developing from a rapid decrease of sonic velocity. This varies subtly when considering T_i, as now $c_s = \sqrt{\gamma_i T_i + \gamma_e T_e}$, and acceleration is also given by gasdynamic contributions. In the case for negligible T_i, nonetheless, Mach number comparison with Merino 2023 (Figure 4 (e)) [6] indicates that achieved peak acceleration values are practically equal, but larger regions of sonic flow ($M \approx 1$) develop in the discussed model, due to concentrated ion heating in the edges of the beam.

Further insight may be gathered by retrieving the axial and radial ion fluid velocities, depicted in Fig. 4.6. On the one hand, and as expected from the conducted analysis, a large contribution of ϕ is directed axially in the form of kinetic ion energy (Fig. 4.6(a)). In fact, it can be observed that the divergent plume constituted in the electrostatic potential solution coincides with that of u_{zi} and scales as $u_{zi} \propto (-\phi)^{\frac{1}{2}}$, neglecting T_i influence. Radial velocity, on the other hand, experiences the effect of ϕ jump close to the beam edge, concentrating an outward high velocity section in the plasma-to-vacuum intersection.

4.3. Ion Magnetization Strength, Plasma Detachment and in-plane Electron Current

The initial ion magnetization strength is measured by the parameter Ω_{i0} (i.e., the ion gyrofrequency), which coincides numerically with the magnetic field normalization factor, $\sqrt{m_i T_{e0}}/(eR)$. Based on literature, most of the magnetic nozzle applications are covered by the range $\Omega_{i0} \leq O(10)$. In this particular simulation, initial magnetic strength is taken to be arbitrary and dependent on the geometrical characteristics of the thruster, so that it accounts for an initial magnetic field of $B_0 = 1$ at the thruster's center, C_t. Thus, the ion flow is considered weakly magnetized initially (a condition that is extended down the flow) and the magnetization effect both radially and axially is negligible.

For a quantitative characterization of the magnetization set-up, consider plasma to be

magnetized only in regions where $\Omega_{i0} > R_V(z)M(z) \geq 1$ and to be mildly magnetized in the general case $\Omega_{i0} \leq O(10)$. An analysis on the influence of ion magnetization, considering both mild magnetization ($\Omega_{i0} = 1$) and highly magnetized ions ($\Omega_{i0} = 10$) is performed and displayed in Fig. 4.7.

Observe how as ion magnetization strength is increased to $O(10)$ from mild ion magnetization, the evolution of the commented properties is altered substantially. The natural ion response to additional magnetization is to follow magnetic streamtubes downstream, retarding detachment and promoting plume divergence. The response for $\Omega_{i0} = 10$ resembles that of a closed MA configuration (to be seen in Chapter 6), where the plasma flow that follows connected lines clashes against the symmetric beam and stagnates, thus concentrating ion density that is not able to scape effectively from magnetic confinement. From this phenomena, it is deducted that ion and electron temperature are also concentrated these streamtubes connecting both thrusters. Nevertheless, as open streamtubes do exist, plasma accelerates and eventually separates from magnetic trajectories above the separatrix, conforming two separate jet beams (one corresponding to each of the clustered EPTs devices) that diverge outward from the symmetry plane.

An additional detail on the higher magnetic strength formulation is that the oblique shock structure originating for $\Omega_{i0} = 1$ modifies its behavior when applying $\Omega_{i0} = 10$. Instead of arising as the two jet beams collide and expanding downstream, it now advances towards the throat, creating a complex static flow region where plasma is concentrated and unable to scape. Further research must be performed including collisions to evaluate the effect of high ion magnetization along closed magnetic streamtubes.

The results that follow maintain the $\Omega_{i0} = 1$ assumption indicated in the simulation setup.

The fact that electrons are fully magnetized and ions are weakly magnetized results in electron flow trajectories being completely guided by magnetic streamtubes, as magnetic confinement dominates force balances [47]. While ion flow trajectories are mainly driven by the ambipolar electric field because ion magnetization is not sufficient to control ion inertia. Even at high-magnetization strength values such as $\Omega_{i0} = 100$, magnetic field forces struggle to confine ions to the streamtubes, as shown in [5].

Ion streamlines beginning above the separatrix $\psi_B = 0$, guided by outer magnetic lines, proceed as would be expected in a MN, curving back and around the upper part of the domain in a helicoidal trajectory with respect to the line along $x_{\psi_B=0}$. Those originating below the limiting $\psi_B = 0$, in the region of closed magnetic lines, curve downward and intersect the symmetry plane to eventually cross the magnetic streamtubes. At the periphery of the MA, where the symmetry axis is defined, ion flow becomes essentially straight. Again, as mentioned, across the shock structure, the affected ion trajectories are deflected and curve upward, reducing speed but keeping flow supersonic. The described behavior is displayed in Fig. 4.5(c) for reference, where blue lines correspond to ion streamlines.

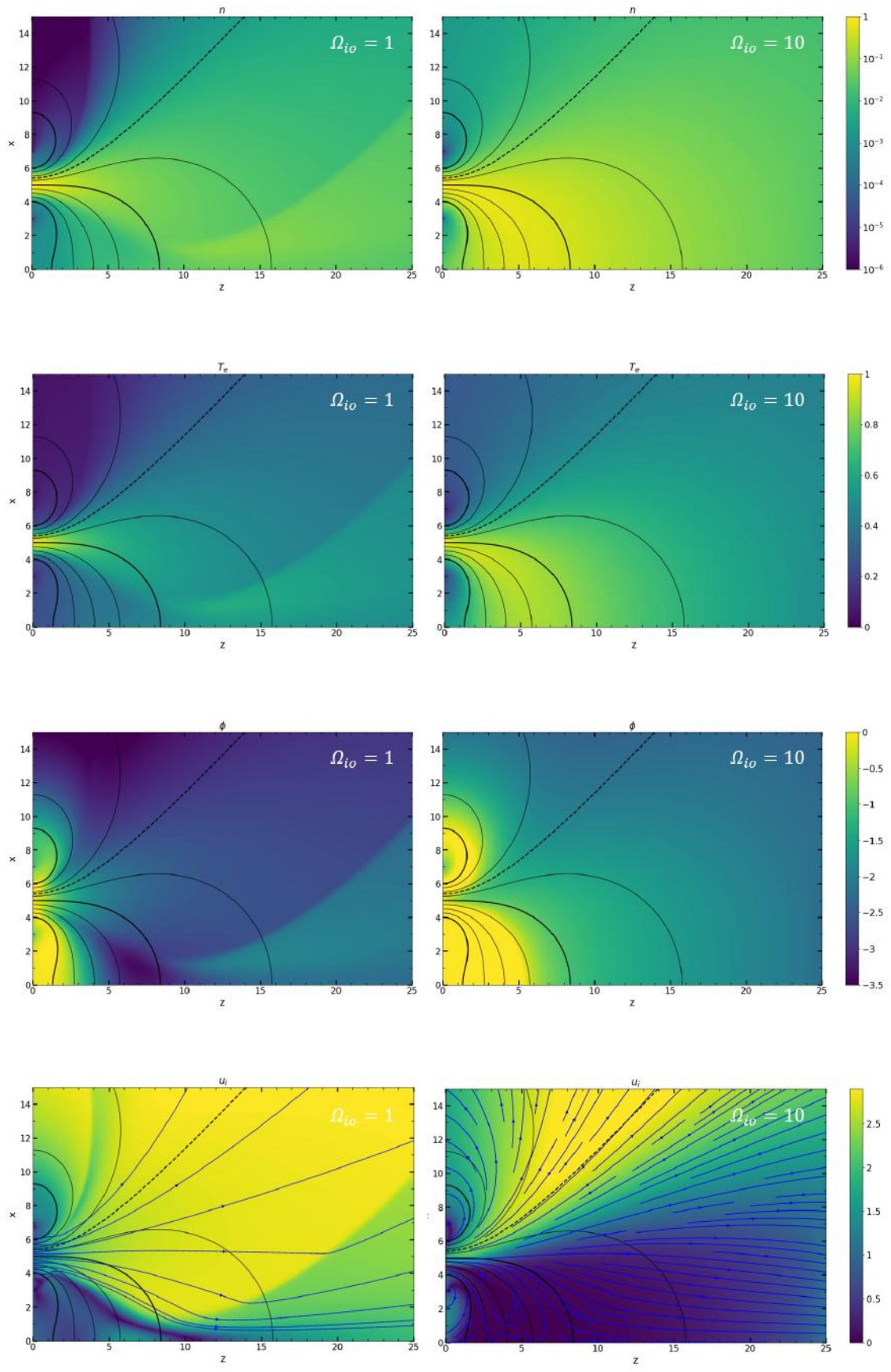

Fig. 4.7. Dimensionless n, T_e, ϕ and u_i, respectively for $\Omega_{i0} = 1$ and $\Omega_{i0} = 10$.

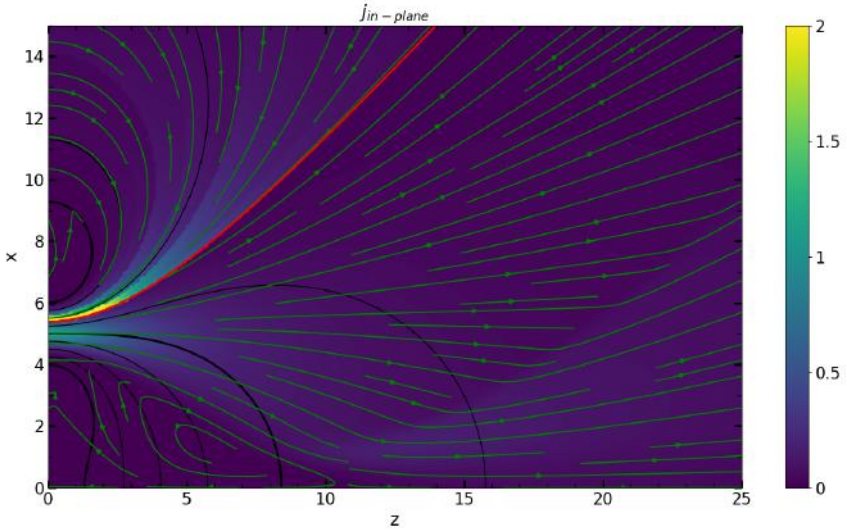

Fig. 4.8. Dimensionless in-plane ion-electron current density $\tilde{\mathbf{j}} = n(\tilde{\mathbf{u}}_i - u_{\|e}\mathbf{1}_b)$. Current flow trajectories are represented by green-colored arrow lines.

Although already confirmed in Merino 2023, a major conclusion arises from the aforementioned phenomenon; ion streamlines are not confined by the MA closed magnetic field lines [48]. Instead, trajectories propagate downstream forming a MN-type jet [6]. This may appear as a trivial conclusion, but it is crucial for the validity of the magnetic arch concept and the operation of the proposed thruster model.

Since ion streamlines progressively separate from magnetic streamtubes where electrons are confined, the unbalance between ion-electron current develops an electric current to maintain plasma current free [49]. Notice that, due to the presence of both open and closed magnetic field lines, respectively above and below the separatrix $\psi_B = 0$, maintaining the current-free condition is not trivial.

As defined in Eq. 4.6, for the cases in which $\psi_B > 0$, a uniform distribution of electron macroscopic velocity is imposed, while for $\psi_B < 0$ the electron flux must be zero. Otherwise, magnetically confined electron trajectories would collide at the symmetry plane, leading to a non-physical solution in the current model[14]. The imposed total electron current at the throat is then found to be negative and axially directed, concentrated at the vicinity of the jet edge, above $\psi_B = 0$. Below the separatrix, the only current contribution is generated by the ion flux. The distribution of $\tilde{\mathbf{j}}_\mathbf{e}$ is computed *a posteriori* from Eq. 2.42. This ensures current-free plasma globally.

Fig. 4.8 displays the total in-plane electric current density defined by $\tilde{\mathbf{j}} = n(\tilde{\mathbf{u}}_i - u_{\|e}\mathbf{1}_b)$, accounting for the electron current distribution above and below the separatrix. Above the separatrix, arrowed lines point towards the nozzle throat, indicating that electron current flows negatively with respect to ions, compensating the integrated surface current and

[14]The simulated model does not include collisional effects or neutral species, which impedes the physical solution for species encounter along magnetic streamtubes. If collisions were to be considered, electron in-plane flux would be modeled differently to account for current ambipolarity.

imposing current-free plasma at the inlet.

The development of electric currents in the plasma implies that, for a finite Ω_{i0}, current ambipolarity (i.e. $\tilde{\mathbf{j}} = 0$) cannot be imposed everywhere in the domain. Condition 2.5 sets $\tilde{\mathbf{j}} = 0$ at the MA throat, but alternative distributions are immediate for current-free plasma conditions. As the computation of $u_{\|e}$ and $\tilde{\mathbf{j}}_e = -nu_{\|e}\mathbf{1}_b$ is performed after solving the rest of equations, we expect the electron flow to self-adjust to meet the imposed boundary conditions inside the source and at the far region of the plume [9].

4.4. Ion and Electron Thermodynamics

Ion and electron thermal energy can be transformed into axially-directed ion energy that accelerates the plasma flow. In essence, the perpendicular energy of each of the species is transferred to parallel energy thanks to the inverse magnetic mirror effect, and by electrostatic reflections at the plasma edge [35][50]. Notwithstanding, the macroscopic effect of each of the species thermal energy contribution is different. In general, electron thermal energy causes electrons to expand guided by magnetic streamtubes and create the ambipolar electric field that pulls the heavy ion species downstream. As introduced, the originated electrostatic potential ϕ acts as an energy conversion intermediary. Ion thermal energy, on the other hand, is essentially responsible for direct gasdynamic acceleration [35].

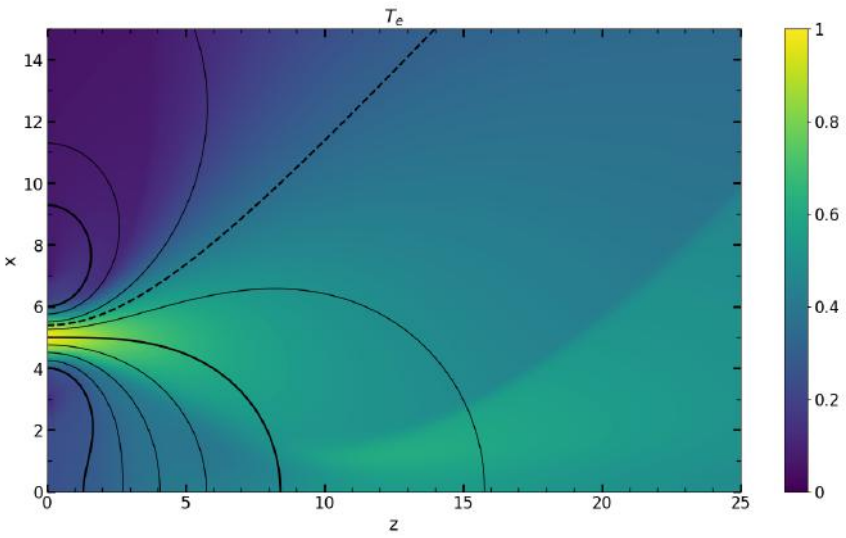

Fig. 4.9. Dimensionless electron temperature distribution computed from isentropic cooling law $T_e = n^{(\gamma_e - 1)}$ for $\gamma_e = 1.2$.

Contribution of each of the species' thermal energy is not evenly distributed, but depends on the fraction of thermal energy carried by each of them. A convenient dimensionless factor was defined and intended to characterize thermal energy distribution, that is $F_{T_0} = T_{i0}/T_{e0}$. The magnitude of this ratio will depend mainly on device type and characteristics, with thrusters such as the HPT with negligible ion temperature

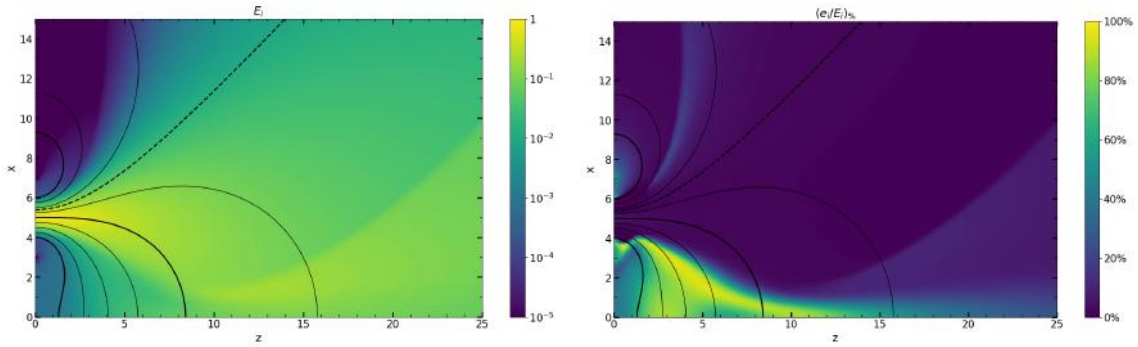

Fig. 4.10. Dimensionless total ion energy E_i (a) and internal ion energy (ion-thermal component) percentage contribution e_i/E_i (b), as defined in Eq. 4.7.

$F_{T_0} = T_{i0}/T_{e0} \ll 1$, and others such as VASIMR which can revolve around values of orders $O(1) - O(10)$. The approach of the current simulation is to approximate a thermodynamic solution for a cold-ion plasma with a predefined polytropic relation for electron cooling. Thereby, the case for which $F_{T_0} = T_{i0}/T_{e0} = 0.1 \ll 1$ is considered, where the mechanism for ion acceleration is driven by the ambipolar potential and ion-thermal acceleration effect is nearly negligible. The cooling rates of ions and electrons, represented by the effective values of γ_i and γ_e, pose an important parametrization parameter and can depend on the detailed kinetic behavior of each species. For the purposes of the model, and in accordance with experimental data retrieved from [35], consider initially $\gamma_i = 5/3$ and $\gamma_e = 1.2$.

Fig. 4.9 shows the electron pressure and temperature distribution governed by the electron polytropic cooling law, $p_e = n^{\gamma_e}$ and $T_e = n^{\gamma_e - 1}$. The introduction of this isentropic profile stands in contrast with the unphysical behavior of an isothermal model, bounding the downstream value of ϕ to an asymptotic constant. Moreover, it was demonstrated by [35] that electron cooling facilitates plasma detachment, promoting earlier ion separation.

Ion thermal energy is defined at the inlet from an isentropic temperature profile, such that $T_i(0, x) = T_{i0} n(0, x)^{\gamma_i - 1}$, where $T_{i0} = F_{T_0} = 0.01$, and is expected to maintain this condition along streamlines, as long as no rarefaction or shock waves are crossed. The ion-electron temperature ratio is expected to remain constant given the isentropic nature of the flow, recalling the entropy conservation principle derived from the energy and continuity conservation expressions. From Eq. 2.39 the modified ion energy distribution $\hat{E}_i$ is solved for in the simulation, nonetheless, for adequate physical interpretation ion total energy E_i and ion internal energy e_i need to be computed as,

$$E_i = \hat{E}_i - n\phi, \qquad e_i = \hat{E}_i - n\phi - \frac{1}{2} n \|\mathbf{u}_i\|^2 = E_i - \frac{1}{2} n \|\mathbf{u}_i\|^2. \tag{4.7}$$

Fig. 4.10(a) displays ion total energy as defined in Eq. 4.7, where the kinetic energy term dominates, indicating a rapid species acceleration. The downstream-directed

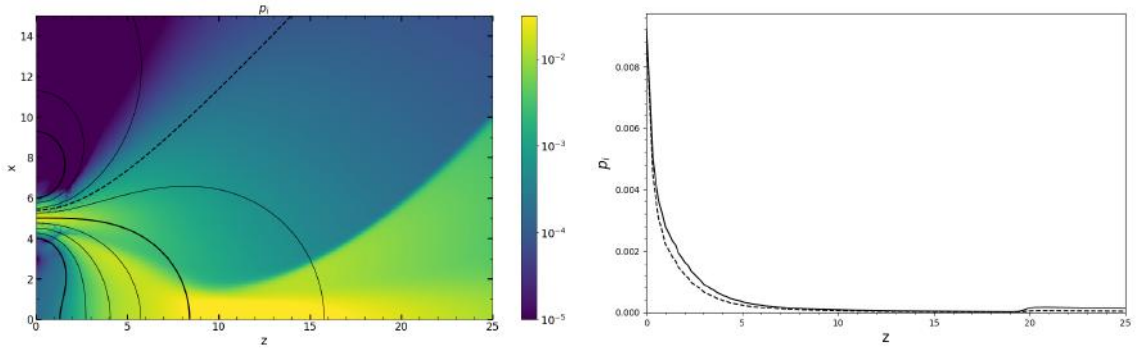

Fig. 4.11. Dimensionless ion pressure p_i map (a) and evolution along selected streamline (b) originating on $x = C_t$. Computed from the originally retrieved $\hat{E}_i$, given an initial temperature factor $T_{i0} = F_{T_0} = 0.01$. Continuous black line corresponds to energy-computed ion pressure and dashed line accounts for ideal adiabatic evolution of the flow.

shock wave is visible and leads to an energetic upswing which accounts for the ion density increase. It is noticeable that the magnitude at the thrusters throat is of $O(1)$ and the internal energy, displayed in Fig. 4.10(b) as its contribution towards total energy, falls below $O(0.01)$ at its maximum value at the nozzle throat, accounting for the cold-ion approximation. Percentage-wise, thermal internal energy is then negligible when compared to the total energy of the system, including kinetic contribution of the macroscopic flow velocity.

In Fig. 4.10(b), a concentrated region of ion thermal energy is observable along the lower plasma beam edge, towards the symmetry plane. This highly ion thermal energetic section originates the described shock structures and composes a high pressure-temperature discontinuity, where ion energy is not transferred to direct kinetic energy but, instead, acts as an ion heating mechanism. The phenomenon is observable over primary fluid characteristics such as p_i, shown in Fig. 4.11(a). Ion pressure is directly computed from $\hat{E}_i$, n and ϕ following Eq. 2.35. When accounting for the ion-cooling mechanism, its downstream evolution and effects relate to those commented for electrons. Introducing a non isothermal ion contribution provides a more sophisticated physical approximation which facilitates earlier ion separation, resulting in easier plasma detachment.

Another relevant detail derived from the analysis is that the thermal distribution is found to be isentropic $T_i \propto n^{\gamma_i - 1}$, an indirect imposition introduced when considering ion energy conservation principle in Eq. 2.39, with the given γ_i cooling rate. This resembles the cooling profile assumed for electrons with an ion-specific cooling rate and a proportional factor given by $T_{i0} = F_{T_0} = 0.01$. Fig. 4.11(b) depicts the ion pressure evolution along the indicated streamline and Fig. 4.12 displays the curve for entropy evolution of the system, computed as:

$$S_i = \frac{1}{\gamma_i - 1} \ln\left(\frac{p_i}{T_{i0} n^{\gamma_i}}\right) \tag{4.8}$$

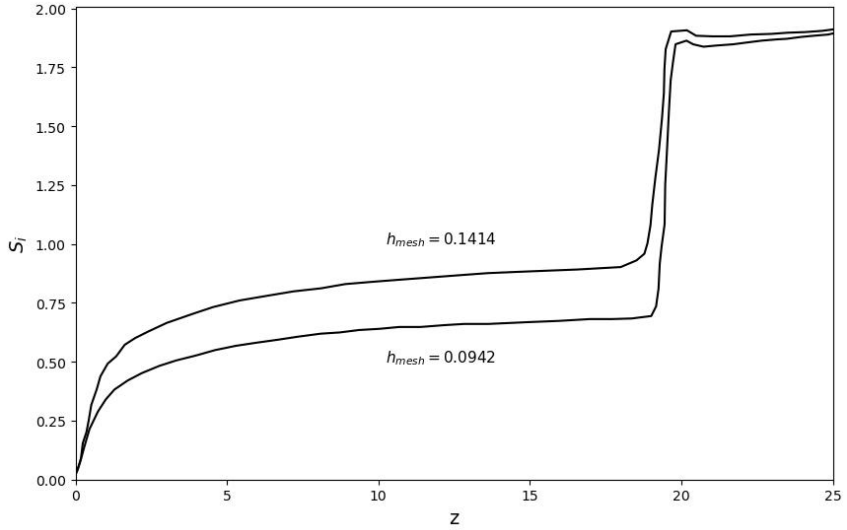

Fig. 4.12. Entropy distribution, S_i, along selected streamline originating on $x = C_t$, computed from Eq. 4.8, respectively for mesh size $h_{mesh} = 0.0942$ (fine) and $h_{mesh} = 0.1414$ (coarse).

Actual p_i is gathered from the total energy distribution solution (E_i) and the expected $p_{i,isentropic}$ from the cooling law relation $p_{i,isen} = n^{\gamma_i}$. In the presented analysis, the discrepancy between the expected isentropic pressure evolution $p_{i,isentropic}$ and the actual computed pressure p_i arises primarily in the near-throat region, where a significant entropy increase is observed instead of its expected constant behavior. This deviation can be attributed to the numerical method employed, the local Lax-Friedrichs scheme.

Lax-Friedrichs introduces an inherent artificial dissipation due to the way eigenvalues are approximated in the flux calculation, leading to a loss of fine-scale structures in the solution. This diffusion contributes to the observed entropy rise, as small-scale pressure variations near the throat are overly damped, specially when performing cold approximations with $T_{i0} \rightarrow 0$. Due to this smoothing effect, localized shock structures and rarefaction waves at the throat may not be accurately captured. Concluding, entropy rise in the throat is likely not a physical phenomenon, but rather an artifact of the numerical dissipation. This can be proven by noticing that for finer meshes, where minimum cell size h_{mesh} is smaller, the near-throat jump reduces.

On the other hand, at the far expansion region, where the selected streamline crosses the originated shock structure ($z \approx 19$), an increase in entropy is also noticeable. Entropy increases due to the sudden compression and dissipation of energy within the system, a fundamental consequence of the second law of thermodynamics. This is interpreted as a consequence of the shock's formation and, thereby, as a physical response of the system. Once the shock structure is crossed, downstream from the discontinuity, entropy remains nearly constant, as would be expected. Again, it may be proven that this mechanism is loely physical, and not induced due to numerical artifacts, because when reducing the resolution of the mesh the far-region entropy level remains stable.

4.4.1. Electron Polytropic Index γ_e Influence

As commented, the polytropic index γ_e constitutes an essential cooling factor modifying the downstream evolution of the plasma flow. Simulation under analysis explores the case for which $\gamma_e = 1.2$, a conventional case recurrent in numerous literature [51]. Nevertheless, further consideration on alternative cooling rates is essential for full electron thermodynamics comprehension, thus two additional cases have been considered for the previous simulation setup, $\gamma_e = 1.01 \approx 1$ (isothermal approximation) and $\gamma_e = \gamma_i = 5/3$. Due to the implemented plasma equations, particularly Eq. 2.23, it is required that $\gamma_e > 1$, so that the isothermal case may only be approximated.

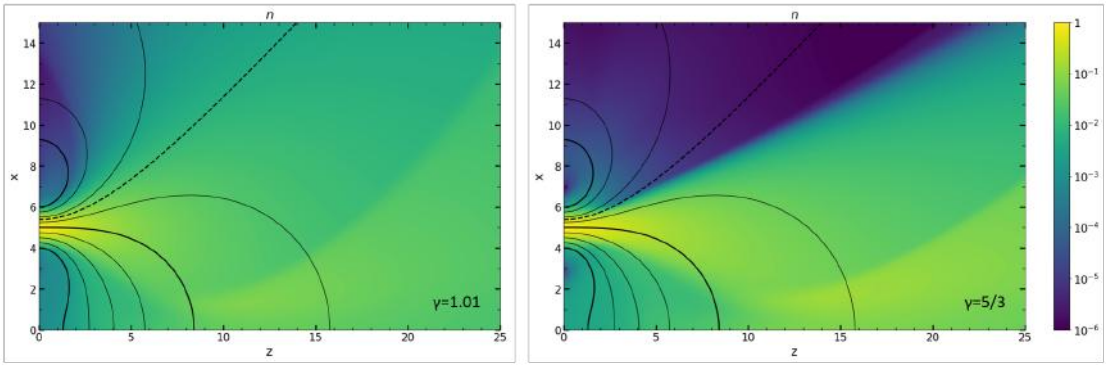

Fig. 4.13. Dimensionless density n for iothermal case $\gamma_e = 1.01$ (a) and $\gamma_e = 5/3$ (b).

Fig. 4.13 displays the density n map, where the influence of γ_e results evident. Near the isothermal case, $\gamma_e = 1.01$, plume divergence is accentuated as electron pressure gradients are minimized. The confining effect is then reduced, allowing for ion streamlines to diverge earlier in the expansion. This results in a larger bulk of flow colliding at the symmetry plane, incrementing oblique shock dimensions but alleviating the discontinuity. For $\gamma_e = 5/3$, the effect is quite the opposite, the plasma beam concentrates as the electron pressure gradients are increased due to the larger cooling factor. This collimation effect results in an accentuated rarefaction where the plasma jet and vacuum meet, while reducing the expansion of the downstream shock structure. Hence, electron cooling facilitates ion detachment from magnetic streamtubes and promotes earlier separation of the trajectories, as proved for MNs in [35].

The vacuum-plasma transition is highly determined by the evolution of the ambipolar electric field, particularly by the values attained at the far expansion region, ϕ_∞. As defined in [35], the asymptotic value of the potential is defined as,

$$\phi_\infty = -\frac{\gamma_e}{\gamma_e - 1} T_{e0} \quad \text{as} \quad (n, T_e) \to 0, \tag{4.9}$$

however, although density is practically negligible at this edge regions, the values of ϕ_∞ still vary. This minor differences at infinity exert radial forces that confine the plasma

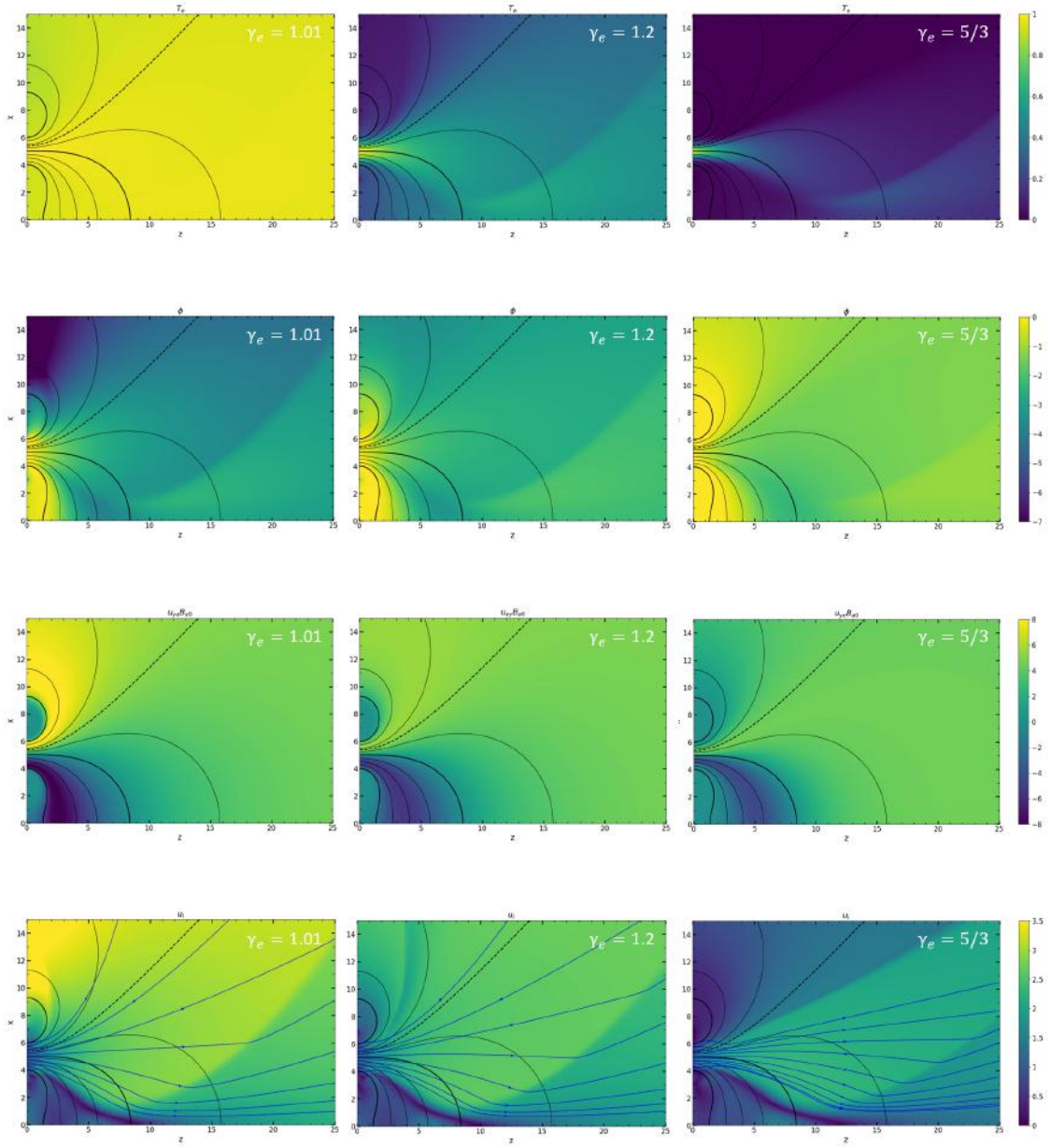

Fig. 4.14. Dimensionless electron temperature T_e, ambipolar electric potential ϕ, out of plane electron velocity $u_{ye}B_{a0}$ and ion in-plane velocity u_i. On the left for $\gamma_e = 1.01$, center for $\gamma_e = 1.2$ and right for $\gamma_e = 5/3$.

plume, accentuating the plasma-vacuum transition, and accentuating this rarefaction as γ_e is increased.

The aforementioned phenomena is confirmed by the properties represented in Fig.4.14. Electron temperature evolution (depicted in Fig. 4.14(a)-(b)), given by $T_e = n^{\gamma_e - 1}$, is nearly isothermal for the first case, with reduced gradients and a variation range of $\Delta T_e = 0.13$ given by the approximation. In the second case, a larger polytropic index accentuates electron temperature and pressure gradients, leading to a faster isentropic cooling mechanism. This, in turn, influences the map of ϕ (Fig. 4.14(c)-(d)), H_e and H'_e, which determine the out-of-plane electron velocity u_{ye} (Fig. 4.14(e)-(f)). Electron u_{ye} highly influences electromagnetic forces, as u_{yi} contribution is negligible at low magnetization strength conditions. In the isothermal case, elevated u_{ye} is concentrated at the near throat expansion region, where line curvature is accentuated. This poses larger electromagnetic forces that manage to prevent ions from early streamtube separation. On the other hand, for $\gamma_e = 5/3$, u_{ye} and magnetic forces decay is faster, which implies that these become incapable of deflecting ion trajectories to match magnetic streamtubes. The aforementioned features lead to fundamental changes in thrust generation and plume efficiency, which are detailed in Section 4.5.

4.5. Local Thrust and Plume Efficiency

Momentum equation (Eq. 2.38) details the radial (x) and axial (z) forces driving the plasma expansion downstream. In the radial direction two contributions are distinguishable, an expanding pressure gradient $\partial(p_e + p_i)/\partial r$, both by ions and electrons, and a confining magnetic force, defined as $F_{x,B} = j_y B_z$. Notice that $j_y = n(u_{yi} - u_{ye})$ is the out of plane current density dominated, in the case of nearly cold ions, by electron thermal energy. This x-force magnetic density is essentially perpendicular to the magnetic lines at the thruster's outlet and will balance forces along the throat. However, as the expansion advances downstream, pressure gradient will tend to dominate, thus observing a radial expansion of the plasma plume.

Fig. 4.15(a) depicts the x-directed magnetic force density, which confines the expansion laterally. In the innermost part of the magnetic arch, between the two plasma sources, the confining force points in the $x > 0$ direction, while in the rest of the domain it points along $x < 0$, helping reduce the jet divergence [6].

In the axial direction, the pressure gradient and the axial magnetic force, $F_{z,B} = -j_y B_x$, stablish the acceleration mechanism. In the studied case, this corresponds mainly to the electron electrothermal and the equivalent to a MN's Hall acceleration, respectively. As previously commented, the acceleration mechanism relies on the ambipolar potential field arising to maintain quasineutrality, essentially holding electron inertia and transmitting their thermal energy to ion kinetic energy.

Fig. 4.15(b) depicts the z-directed magnetic force density, which is large and posi-

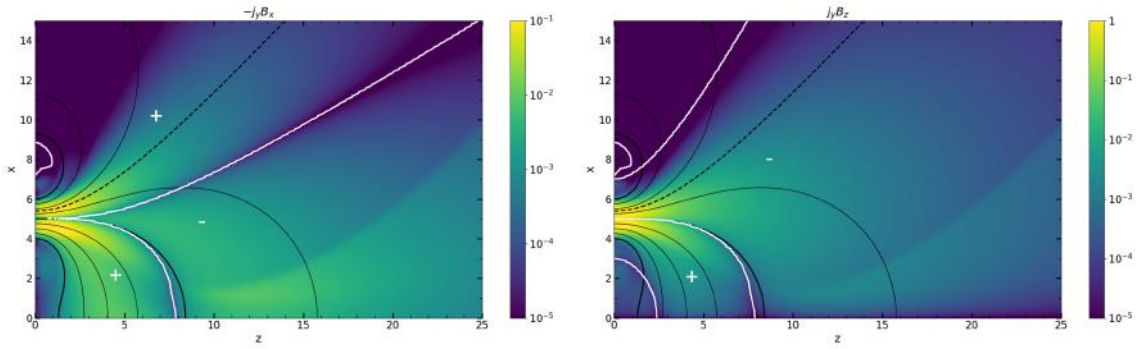

Fig. 4.15. Magnetic force density in the axial $F_{z,B} = -j_y B_x$ (a) and radial $F_{x,B} = j_y B_z$ (b) directions for the case $\gamma_e = 1.2$. White lines separate regions with positive (+) and negative (-) contributions of the force densities.

tive at the beginning of the expansion, where n, T_e and B are large. Nevertheless, the flow continues downstream a negative contribution arises at the point where $B_x = 0$ and lines curve towards the symmetry plane. This negative force is particularly noticeable at the shock structure, where out-of-plane current density increases locally. The fact that a negative axial force contribution arises poses major consequences for thrust generation. While positive thrust is generated near the outlet, on the far expansion region a drag force will arise as a consequence of the shock formation, as observed in Fig. 4.16.

The local plasma thrust may be defined from the indicated momentum and pressure forces, respectively for ions and electrons, and in a given rectangular control volume $\Omega(z)$ that spans from $z = 0$ to a variable z-position. Plasma thrust may be then expressed as $F(z) = F_i(z) + F_e(z)$, with

$$F_i = \int_{\partial\Omega(z)} [(nu_{zi}^2 + nT_i)\mathbf{1}_z + nu_{xi}u_{zi}\mathbf{1}_x] \cdot \mathbf{1}_n dS, \qquad F_e = \int_{\partial\Omega(z)} nT_e\mathbf{1}_z \cdot \mathbf{1}_n dS. \tag{4.10}$$

Where $\partial\Omega(z)$ constitutes the boundary of the control volume and $\mathbf{1}_n$ accounts for the surface normal unitary vector, which simplifies the expression to the z-directed contribution when considering flux across the O_{xy} plane. Observe that the fundamental performed computation is the flux integral of total momentum on the selected boundary of integration. Sufficiently downstream, electron force contribution decays to zero as density reduces, while ion contribution dominates. From the expression it is understood that the expansion essentially converts electron thermal energy into ion kinetic energy, accelerating the later mentioned species. Notice, however, the presence of the ion thermal energy term arising in the ion force integral as the thermodynamics of this species are considered. This contribution modifies the acceleration mechanism, such that the ions are not only transferred energy in solely kinetic form, but thermal energy too, giving rise to an ion-electron energy interaction that leads to heating and cooling mechanisms downstream and ion acoustic waves forming on the solution.

Rearranging expressions in Eq. 4.10 along the axial momentum direction, in order to

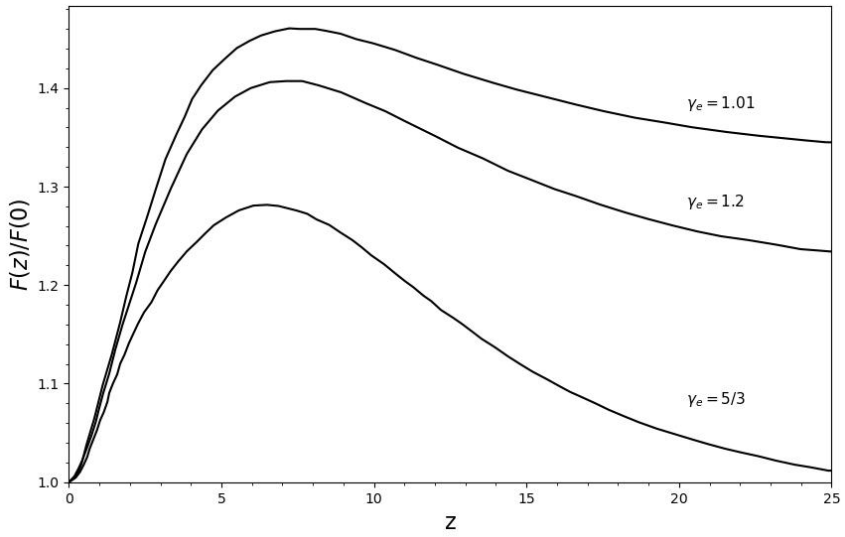

Fig. 4.16. Magnetic thrust integral $F(z)$ as a function of z, normalized with the total momentum flux at the throat, $F_0 = F(0)$. Curves correspond respectively for $\gamma_e = 1.01, 1.2 \text{and} 5/3$.

eliminate the ambipolar electric field, and integrating along the predefined control volume $\Omega(z)$, leads to

$$F(z) = F_0 + F_v, \tag{4.11}$$

with $F_0 = F(0)$, the initial momentum flux of the plasma coming out of the sources, and

$$F_v = \int_{\Omega(z)} F_{z.B} d\Omega = \int_{\Omega(z)} (-j_y B_x) d\Omega \tag{4.12}$$

Fig. 4.16 displays the thrust force evolution $F(z)$ normalized with the integrated force contribution at the throat $F(0)$, for the cases $\gamma_e = 1.01, 1.2 \text{and} 5/3$. For the conventional case $\gamma_e = 1.2$, a large positive magnetic thrust is generated in the first part of the expansion, reaching its largest contribution at $F(z \approx 7.1) \approx 1.4$. As plasma approaches the bending of closed magnetic lines and a region of negative axial magnetic force density is developed, thrust contribution becomes negative (i.e. magnetic drag), resulting in $F(z)$ decreasing to a value of $F(z = 25) \approx 1.225$. The negative thrust contribution is not strictly a consequence of the shock structure, in fact, it develops due to a phenomena inherent to the configuration of a MA and the applied closed magnetic streamtubes. However, the increase in negative axial magnetic force due to the discontinuity highly influences the thrust drop. This accounts for an approximate 12% from the peak value. When compared to Figure 7 in Merino 2023, the introduction of ion-thermodynamic effects induces an elevation of of thrust generation at its peak value, with it increasing approximately a 7%.

For alternative electron cooling cases, the evolution of local thrust varies notably. For nearly isothermal cases $\gamma_e = 1.01$, electromagnetic forces decay at a slower rate, thus resulting in a larger thrust accumulation in the near region of the expansion. Due to this, shock expansion and discontinuity limiting differences are mitigated, thus preventing from excessive magnetic drag. Notice that in this particular case, although plume

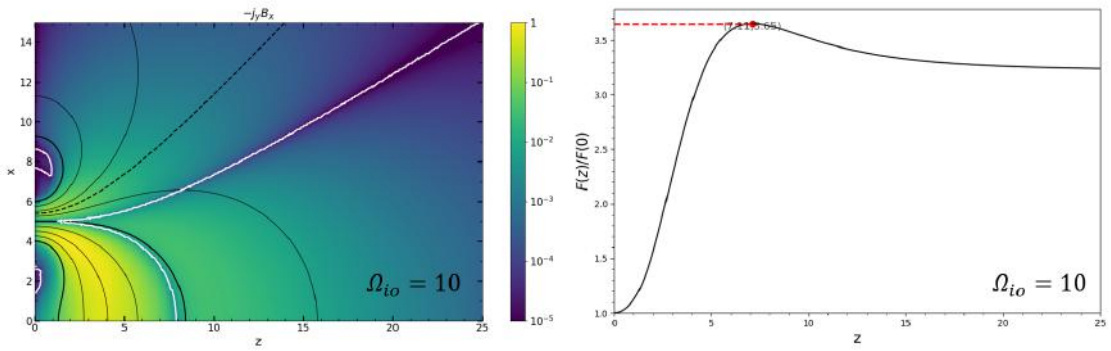

Fig. 4.17. Magnetic thrust integral $F(z)$ as a function of z, normalized with the total momentum flux at the throat, $F_0 = F(0)$ for $\Omega_{i0} = 10$.

divergence is higher and jet is less collimated, thrust remains larger than for faster cooling cases. For values of $\gamma_e = 5/3$ behavior falls under expected physical mechanisms, faster decay of electromagnetic forces imply a lower initial thrust region and accentuation of the shock structure dimensions account for the decline in local thrust (i.e. increase in magnetic drag, negatively affecting thrust).

Fig. 4.17 gives some additional insight on the $\Omega_{i0} = 10$ case. Magnetic drag is mitigated, as a large portion of the positive z-directed magnetic force is concentrated along the open streamtubes, and oblique shock formation is avoided. Thrust curve is elevated, offering higher effective thrust levels than those occurring for mild ion magnetization. This proves that, in a MA, detachment occurring further downstream acts in favor of thrust levels, probably due to the closed topology of the clustered device.

It is relevant to notice that Fig. 4.16 constitutes a representation of a defined control volume with z_F being defined by the z-axis coordinates. Consequently, the effective thrust generated by the device accounts for that found at a control volume reaching $z_F \to \infty$ or, in other words, the asymptotic normalized thrust value resulting from the evolution with z. The depicted figure displays the expected asymptote of the curve as a dashed line at $F(z)/F(0) = 1.225$, with this being an approximation of the expected total thrust generated by the MA. A similar approach is applicable to the computation of total and axial ion power, where the final asymptotic values provide insight into the total plasma flow characteristics and energy conversion efficiency.

For the axial ion power analysis, an expression obtained from the axial momentum equation may be derived and takes the form

$$P_{zi}(z) = \int_{\partial\Omega(z)} \frac{1}{2} n u_{zi}^3 dS = P_{zi,0} + P_{zi,th} + P_{zi,mag} \tag{4.13}$$

with the definition of $P_{zi,0} = P_{zi}(0)$ being the same as that for initial z-directed thrust, and

$$P_{zi,th} = -\int_{\Omega(z)} u_{zi} \left(\frac{\partial p_e}{\partial z} + \frac{\partial p_i}{\partial z} \right) d\Omega, \qquad P_{zi,mag} = -\int_{\Omega(z)} u_{zi} j_y B_x d\Omega. \tag{4.14}$$

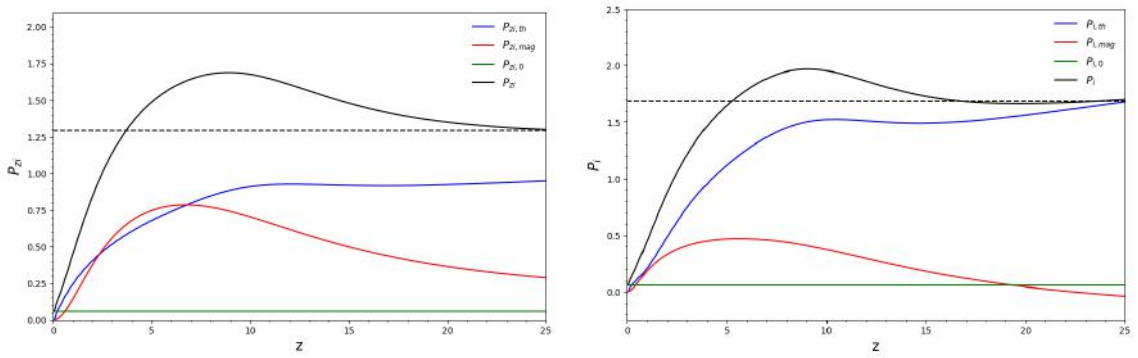

Fig. 4.18. Dimensionless axial total ion axial power $P_{zi}(z)$ (a) (as defined in Eq. 4.13), and dimensionless total ion power $P_i(z)$ (b) (as defined in Eq. 4.16).

Here, $P_{zi,th}$ is no longer simply the electronthermal power gain (as would be in cold-ion models), but the ionthermal contribution is also of relevance. For the present simulation, due to nearly-zero ion temperature, its introduced effect is not of major importance, but Eq. 4.14 should be consistent with the model, specially at higher initial ion thermal energies. $P_{zi,mag}$, on the other hand, corresponds to the electromagnetic power gain.

In Figs. 4.18(a)-(b) the reader may observe the z-directed ion power evolution, (a) depicts the contribution of the various terms described in Eq. 4.14, while (b) accounts for the addition of the aforementioned terms. In the proposed simulation, the thermal energy from the electrothermal component is the dominant contribution, while the z-directed magnetic components comes from the in-plane current (dominated by electron flow) and introduces a magnetic drag that reduces the overall generated power. Typically, from the graph of axial power, one may determine whether the MA is predominantly an electrothermal or an electromagnetic plasma accelerator depending on the initial plasma conditions [9]. In this case, a balance between the contributions is observed in the initial region and, as the plasma expands, the ion-electron (i.e. mostly electron due to cold-ion approximation) pressure term gains importance, compensating for magnetic drag uprise, thus from the energy conversion viewpoint, the device is mainly electrothermal.

The analysis varies subtly when studying the equation for the total ion power. For convenience, let us recall and rewrite the equation for ion mechanical energy (Eq. 2.15),

$$\nabla \cdot \left(\frac{1}{2} n \|\mathbf{u_i}\|^2 \mathbf{u_i} \right) + \mathbf{u_i} \cdot \nabla p_i = -\mathbf{j_i} \cdot \nabla \phi = -\mathbf{u_i} \cdot \nabla p_e + \mathbf{u_i} \cdot (\mathbf{j_e} \times \mathbf{B}) \tag{4.15}$$

.

Integrating the previous expression over the $\Omega(z)$ volume, the total ion power function is retrieved

$$P_i(z) = \int_{\partial\Omega(z)} \frac{1}{2} n u_{zi} \|\mathbf{u_i}\|^2 dS = P_{i,0} + P_{i,e}. \tag{4.16}$$

Similarly to previously commented cases, $P_{i,0} = P_i(0)$ and $P_{i,e}$ may be understood as the electric work exerted on the ions by the arising ambipolar electric field. In analogy to

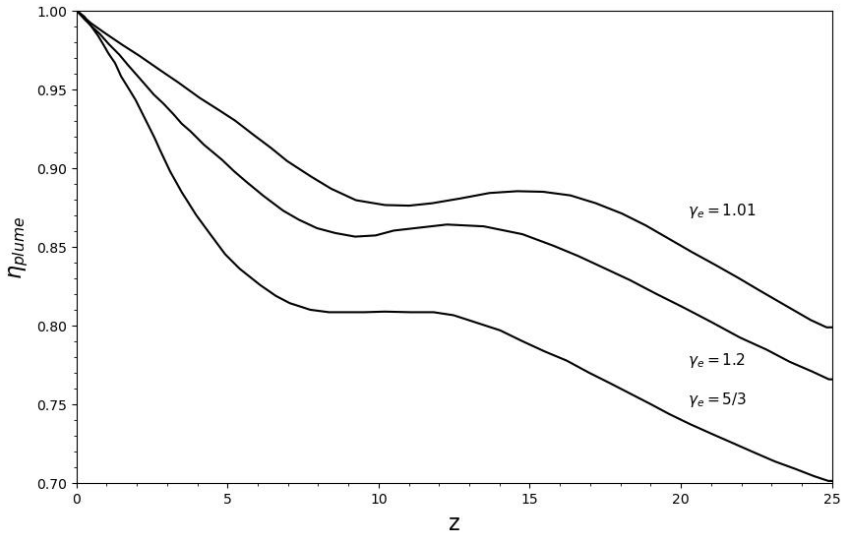

Fig. 4.19. Plume efficiency ($\eta_{plume} = P_{zi}/P_i$) along the domain.

Eq. 4.13, this work is split in thermal and magnetic contributions, as $P_{i,e} = P_{i,th} + P_{i,mag}$, with each of the terms being,

$$P_{i,th} = -\int_{\Omega(z)} (\mathbf{u_i} \cdot \nabla p_e + \mathbf{u_i} \cdot \nabla p_i) d\Omega, \qquad P_{i,mag} = \int_{\Omega(z)} \mathbf{u_i} \cdot (\mathbf{j_e} \times \mathbf{B}) d\Omega. \tag{4.17}$$

Figs. 4.18(c)-(d) represent the total ion power evolution and the profile of each of its components in Eq. 4.17. Similarly to the case for axially directed ion power, thermal domination is more pronounced than magnetic component, with a final linear increase from $z \approx 22.5$ arising from the shock structure expansion and consequent ion pressure increment. The introduction of the radial ion-electron thermal expansion pressure forces, that gain relevance downstream, increase the total power generation but have an unfavorable effect on plume efficiency.

Finally, consider that the radial expansion of the plasma increases the overall plume divergence which, as commented, induces drag forces and negatively affects thrust generation. A characteristic parameter for electric propulsion devices is the efficiency, which for EPTs and, particularly, the case of magnetic arch, constitutes an accurate indicator of the thruster's thrust generation capacity. The ion-based plume efficiency can be defined as,

$$\eta_{plume}(z) = \frac{P_{zi}}{P_i} = \frac{\int_{\partial\Omega(z)} \frac{1}{2} n u_{zi}^3 dS}{\int_{\partial\Omega(z)} \frac{1}{2} n u_{zi} \|\mathbf{u_i}\|^2 dS} \tag{4.18}$$

The MA propulsive performance is shown in Fig. 4.19 and this serves as confirmation of the commented behavior. The downstream radial expansion due to pressure-term domination over magnetically originated power leads to an unfavorable plume divergence that reduces thruster's efficiency. This again indicates that fast-diverging devices imprint a larger radial component of the plasma jet which, eventually, impose a penalty on the thrust efficiency. The flat plateau arises from the thrust approaching asymptotic values

as the jet beam influence reduces downstream, however, a subsequent fall occurs due to the origination of the shock structure at $z \approx 12.5$ and an increase in the total ion power, again reducing plume efficiency. The objective is, thereby, to develop a MA of low ion magnetization, so that a long and slowly diverging magnetic field is originated, while still ensuring correct operation with magnetically confined electrons.

The asymptotic behavior commented for thrust and power device properties is also present in the computation of plume efficiency. For a large enough control volume, this is $z \to \infty$, the performance of the MA would attain its overall efficiency. Due to the selected domain characteristics, it is not possible to infer the net efficiency. Consequently, a decrease in the final indicated magnitude is expected for the expansion's far region and, thereby, for the effective overall device efficiency. Based on empiric correlations and efficiency curve tendency, plume efficiency for $\gamma_e = 1.2$ is expected to fall around $\eta(z \to \infty) \approx 0.6$.

Observe how faster cooling rates elevate plume efficiency values, although, as commented, effective efficiency may not be inferred and is expected to be lower than final represented values.

A final note on the specific impulse of the MA, $I_{sp} = F(z)/\dot{m}$, is also required. Notice that due to the definition of $F(z)$, I_{sp} follows its same evolution, and defining $I_{sp,0}$ as the specific impulse at the throat, it is derived that:

$$\frac{I_{sp}(z)}{I_{sp,0}} = \frac{F(z)}{F_0}. \tag{4.19}$$

The evolution along the expansion is, consequently, identical. Both F_0 and $I_{sp,0}$ are proportional to the sonic velocity c_s,

$$I_{sp} \propto c_s, \qquad F_0 \propto R^2 n_0 c_s, \tag{4.20}$$

which in turn is dependent on ion and electron initial temperature profiles. This illustrates the relevance of T_e and T_i over the propulsive performance of the MA. It may be then stated that the MA is an electromagnetic device from the thrust generation perspective and an electrothermal device from the energy conversion viewpoint.

5. ION TEMPERATURE PARAMETRIC ANALYSIS ON MA EXPANSION

As indicated in Chapter 4, in an actual plasma thruster, thermal energy is divided between ion and electron species. Nonetheless, the energetic distribution is usually not even, and two acceleration mechanisms coexist: ambipolar and gas-dynamic, respectively for electrothermal and ion-thermal processes. The relevance and possible dominance of an species is determined by the initial throat thermal conditions, and may be characterized by an already introduced parameter, the ion-to-electron temperature ratio: $F_{T_0} = \frac{T_{i0}}{T_{e0}}$.

Chapter 4 simulates the case for a cold-ion approximation, in which $F_{T_0} \ll 1$. The commented model is typical in HPT devices, in which ion energy may be neglected as an initial approximation. This thruster type relies thereby on the origination of an ambipolar electric field that transfers electron thermal energy to direct ion-kinetic energy, thus accelerating heavy ions and retaining light electrons, confining them along magnetic streamtubes.

Nevertheless, the development of other thrusters, such as the VASIMR, incorporate an Ion Cyclotron Resonance Heating (ICRH) mechanism to enhance plasma energy after ionization in the source, ensuring that most of the energy is transferred to the ions. In this situations F_{T_0} may reach higher values ranging between $O(1) - O(10)$.

The present Chapter intends to explore the physical behavior of high ion thermal energy thrusters and determine the potential of new thrusters under development. To do so, four model situations will be considered: a case for dominant electron thermal energy $F_{T_0} = 0.1$, a case for comparable ion and electron thermal contribution $F_{T_0} = 1$, another in which ion thermal energy $F_{T_0} = 3$ is considerable, and a final case in which ion thermal energy is dominant $F_{T_0} = 10$.

5.1. Description of the Simulation and Boundary Conditions

The set up of the simulation environment is similar to that described in previous Chapters, with a mesh and thruster defined by the characteristics listed in Table 5.1.

TABLE 5.1. MA SIMULATION FOR PARAMETRIC ANALYSIS SETUP CHARACTERISTICS

Mesh Characteristics		**Applied Magnetic Field**		**Thruster Outlet**	
Mesh l_z	7	R_w	1	R_t	0.5
Mesh l_x	5	C_w	x = 2, -2	C_t	x = 2, -2
Mesh size h	0.0471	L_{w1}	x = 1, -1	L_{t1}	x = 1.5, -1.5
Polynomial p	1	L_{w2}	x = 3, -3	L_{t2}	x = 2.5, -2.5

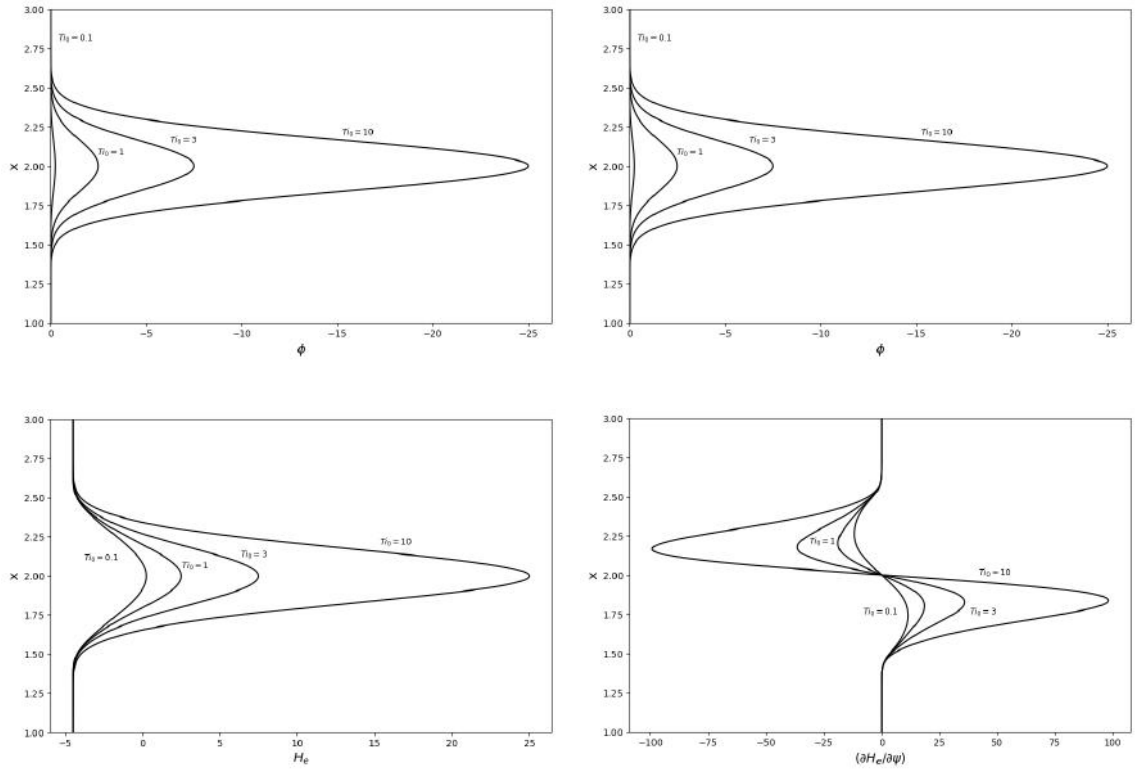

Fig. 5.1. Thruster outlet boundary conditions for ion temperature T_i (a), ambipolar electric potential ϕ (b), electron Bernoulli function H_e (c) and $\partial H_e/\partial\psi$ (d). Corresponding initial ion temperature, T_{i0}, is depicted at the corresponding profile.

Mesh is more compact in order for the parametric analysis not to be excessively computationally expensive. Similarly, magnetization strength as defined by the ion gyrofrequency is arbitrary and determined by the geometric properties of the thruster, and plasma properties at the MA throat need to be given to simulate the four cases of expansion. Namely, it is required to provide profiles for the density n, the velocity vector $\mathbf{u_j}$ of each species, the ion energy $\hat{E}_i$ (by defining a convenient T_i profile), and the electric potential ϕ. Again, Gaussian input profiles are given as expected distributions for upstream source plasma evolution,

$$n(0,x) = 10^{-3(\frac{x-C_L}{R_t})^2} \qquad u_{zi}(0,x) = M_{i0}c_s(0,x) \tag{5.1}$$

$$u_{xi}(0,x) = 0, \qquad u_{yi}(0,x) = 0 \tag{5.2}$$

$$T_i(0,x) = F_{T_0}n(0,x)^{\gamma_i-1} \qquad p_i(0,x) = n(0,x)T_i(0,x) \tag{5.3}$$

$$\hat{E}_i(0,x) = \frac{1}{\gamma_i-1}p_i(0,x) + \frac{1}{2}n(0,x)\|\mathbf{u}_i(0,x)\|^2 + n(0,x)\phi(0,x) \tag{5.4}$$

Recall that when ions carry part of the thermal energy, the newly added radial pressure needs to be confined to prevent from rapid plume divergence. This may be achieved by introducing an azimuthal ion drift, similar but opposite to the electron drift, or by imposing a radial electric field. This radial electric field may be initially determined by

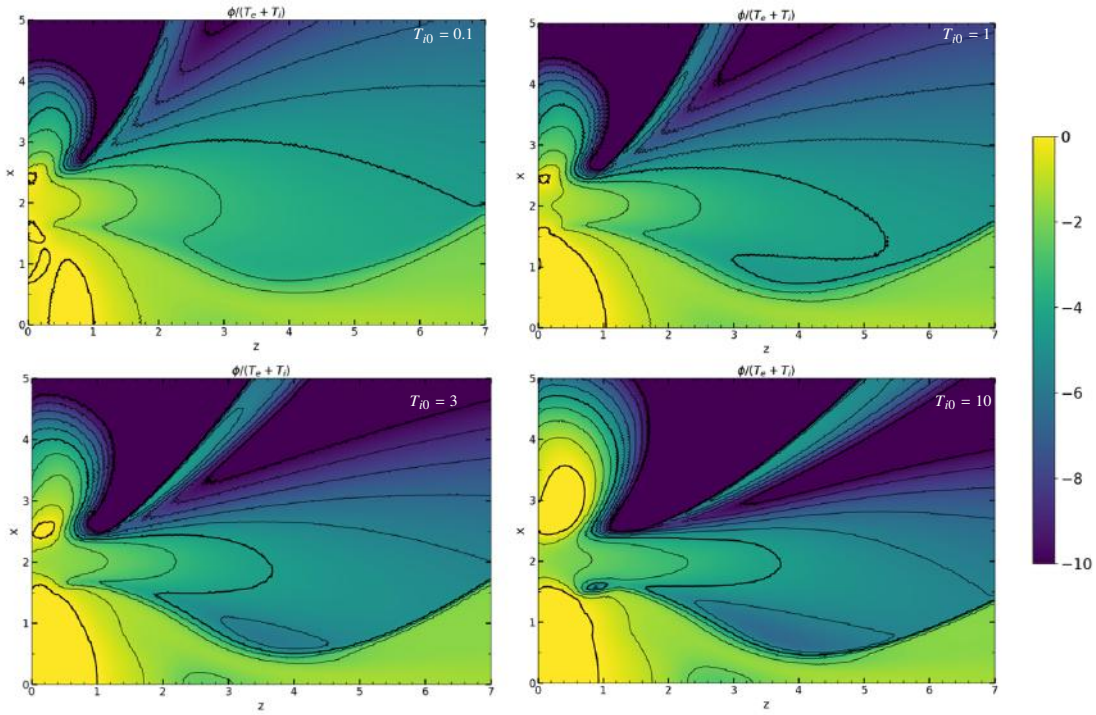

Fig. 5.2. Ambipolar electric potential ϕ normalized with total plasma temperature, $T = T_i + T_e$, for $F_{T_0} = 0.1$ (a), $F_{T_0} = 1$ (b), $F_{T_0} = 3$ (c), $F_{T_0} = 10$ (d). Displayed isolines represent isopotential surfaces with separation $\Delta\phi/T = 1$.

imposing domain-inlet conditions for the ambipolar electrostatic potential ϕ. Derivation of the throat profile for ϕ is described in the ion model plasma model, and it is governed by Eq. 4.5, with the difference that it is no longer approximated to zero in the thruster's outlet.

In Fig. 5.1, throat profiles (i.e. the $(0, x)$ cross section) for p_i, ϕ, H_e and $dH_e/d\psi_B$ are depicted. As would be expected, larger initial ion temperature contributions require from a major ambipolar potential component to balance pressure radial forces, so that $-n\partial\phi/\partial x = \partial p_i/\partial x$, while ion azimuthal velocity remains negligibly low. Consequently, the demand for electron azimuthal velocity is increased, as these must now confine themselves and the ions. This demand results in an additional drift originating $u_{ye,E\times B}$, that adds up to the diamagnetic electron drift $u_{ye,diam}$. This newly added contribution is concentrated at the plasma edge and accounted for in the throat profile shown in Fig. 5.1(d).

5.2. Results and Discussion

Similarly to the phenomenon observed at throat conditions when increasing ion temperature, downstream properties are strongly affected by the pressure rise. Solution for the confining ambipolar potential is highly modified in shape and magnitude, as now the ions are carrying a larger fraction of the total thermal energy. Fig. 5.2 shows the ambipolar

electric potential distribution normalized with the total plasma temperature $T = T_i + T_e$ for the different values of F_{T_0}. Isolines represent isopotential surfaces spaced as $\Delta\phi/T = 1$. Throat region is consistent with the imposed boundary conditions, with higher strength potential for larger inlet temperatures, but downstream evolution differs subtly. The convexity of the represented isopotential lines is an indicator of the expansion distribution. For $T_{i0} = 0$, the ambipolar potential gradient $-\partial\phi/\partial r$ along the thruster points outward, indicating a monotonic decrease downstream, similarly to what observed in cold-conditions for isentropic ion temperature distributions, as studied in [35]. Nevertheless, as T_{i0} increases, $-\partial\phi/\partial r$ lines curve inwardly at the throat, with an accentuating effect for larger inlet temperatures. This essentially confines the expansion, as noted in above. Isopotential lines then curve outward again as flow advances downstream, accounting for the monotonic decrease noticed for near zero T_{i0}.

From the map of ϕ some additional insight on the downstream expansion may be already gathered. Observe how the plasma plume appears to be more collimated for larger F_{T0}, so that plume divergence is decreased and ion trajectory separation from magnetic streamtubes occur at an earlier stage. By imposing a radially force-balanced boundary profile, the ϕ that develops confines the beam further downstream, counteracting expanding electron pressure. The two oblique shock structures arising in Chapter's 4 do appear when increasing ion temperature.

The fact that the originated ambipolar electric field is now responsible of the ion and electron confinement implies that an additional electron drift velocity is developed, $u_{ye,E\times B}$. This newly added contribution, intended to balance the expanding ion pressure, presents a similar qualitative distribution in all four ion-temperature cases, with flow at the throat centerline divided in outside and inside plane velocities (i.e. positive and negative, respectively). Observe how negatively directed electrons are guided mainly by closed magnetic streamtubes, while positive electron flow is constituted from the magnetic line connecting both thrusters (where electron drift velocity falls to zero) and dominates downstream.

Regarding the electron Bernoulli function, H_e, its behavior may be interpreted from the ambipolar potential distribution described in Eq. 2.23, and recalling that it is conserved along ψ_B. Similarly to the inputted boundary condition, the distribution of the function is Gaussian and proportional to the evolution of ϕ. Taking the streamline connecting the thruster's centers as reference, the magnitude of H_e decreases radially from it, with its maximum given by inlet conditions in Fig. 5.1.

Continuing with plasma characteristic properties such as density n and ion in-plane Mach number $M_i = \sqrt{u_{zi}^2 + u_{xi}^2}/\sqrt{(\gamma_i T_i + \gamma_e T_e)}$, the resulting contours are depicted in Fig. 5.3 for all T_{i0} configurations.

Ion density decays progressively downstream from its peak value at the thruster's throat, similarly to the case for the cold ion approximation. No major variations are observed on the decaying factor axially. Nevertheless, as T_{i0} is increased, again, plume

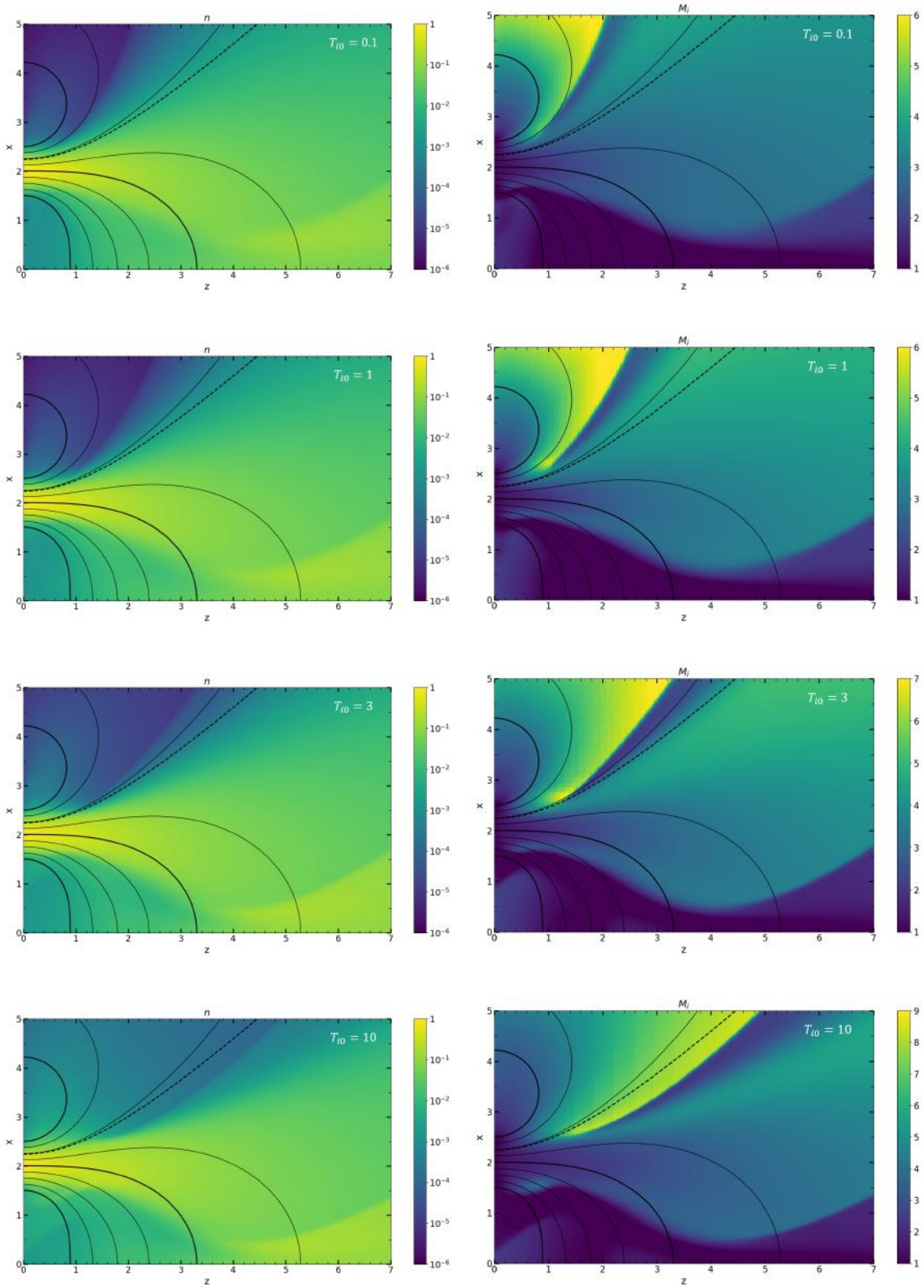

Fig. 5.3. On the left, ion-electron density distribution n. On the right, ion in-plane flow Mach number distribution M_i. Properties displayed for each of the $T_{i0} = 0.1, 1, 3, 10$ simulation cases, ordered from lower to higher.

divergence is highly influenced by the imposed confining conditions. Setting the initial potential to $-n\partial\phi/\partial x = \partial p_i/\partial x$ to prevent from direct radial expansion at the throat (Fig. 5.2), causes an overall alteration of the downstream evolution. Due to the concentration of an elevated modulus ambipolar potential along the centerline connecting the clustered thrusters, plasma tends to experience a larger confining force downstream, which the newly added ion pressure gradients do not manage to compensate. Thus, while the overall axial decay rate of ion density does not show major variations with increased T_{i0}, the radial profile of the plume is considerably modified. The stronger ambipolar potential downstream induces a more focused beam (not only at the throat, as would be expected). This collimation effect, which could be interpreted as beneficial, comes at the cost of increased magnetic drag and altered thrust generation capabilities, as will be seen.

From M_i map, shown in Fig. 5.3, the aforementioned plume divergence phenomena is evident. Comparing Fig. 5.3(a) to Fig. 5.3(d), a clear additional confinement is experienced downstream for the later case, although trajectories are ejected supersonically strictly axially in both cases and a radial velocity component would be expected to develop in the later case, as occurs in (a). Increase in ion temperature results in a increase of ion flow Mach number due to energy conversion processes and faster cooling adiabatic ions. When a larger T_{i0} is injected, acceleration is no longer only electrothermal—with electron thermal energy being converted into direct ion kinetic energy—but now ion thermal energy also adds up as a new kinetic contribution.

To end the ion kinetic analysis, let us explore an additional consequence of T_i increase over the shock structure. It has been commented that the quantitative behavior remains stable, with an overall velocity elevation but no discontinuity enhancement. Nevertheless, the downstream expansion of the shock is alleviated for higher T_{i0}, probably due to the higher collimation of the flow.

Getting into electron and ion thermodynamics, notice that the electron cooling mechanism remains that of simulation in Chapter 4, with the species being modeled as quasi-Maxwellian and its temperature defined by the polytropic relation $T_e = T_{e0}n^{\gamma_e - 1}$. Consequently, T_e distribution alterations with ion influence are essentially a function of those described for density.

Regarding ion temperature T_i, its distribution is highly determined by throat conditions, where plasma is expected to be initially hotter and progressively cool downstream according to the polytropic expression $T_i = n^{\gamma_i - 1}$. In other words, the entire ion temperature profile downstream is elevated, though its relative decay is not altered. Fig. 5.4 depicts ion pressure, $p_i = nT_i$, where the commented effects may be observed. Note that the shock phenomena maintains the temperature elevation but does not quantitatively accentuate due to thermal energy increase.

Fig. 5.5 confirms the polytropic evolution of the downstream flow along the horizontal line at $x = C_t$, where the solid line depicts the p_i extracted from the $\hat{E}_i$ solution, and the dashed line accounts for $p_i = n^{\gamma_i}$. This reassures that the flow expands isentropically

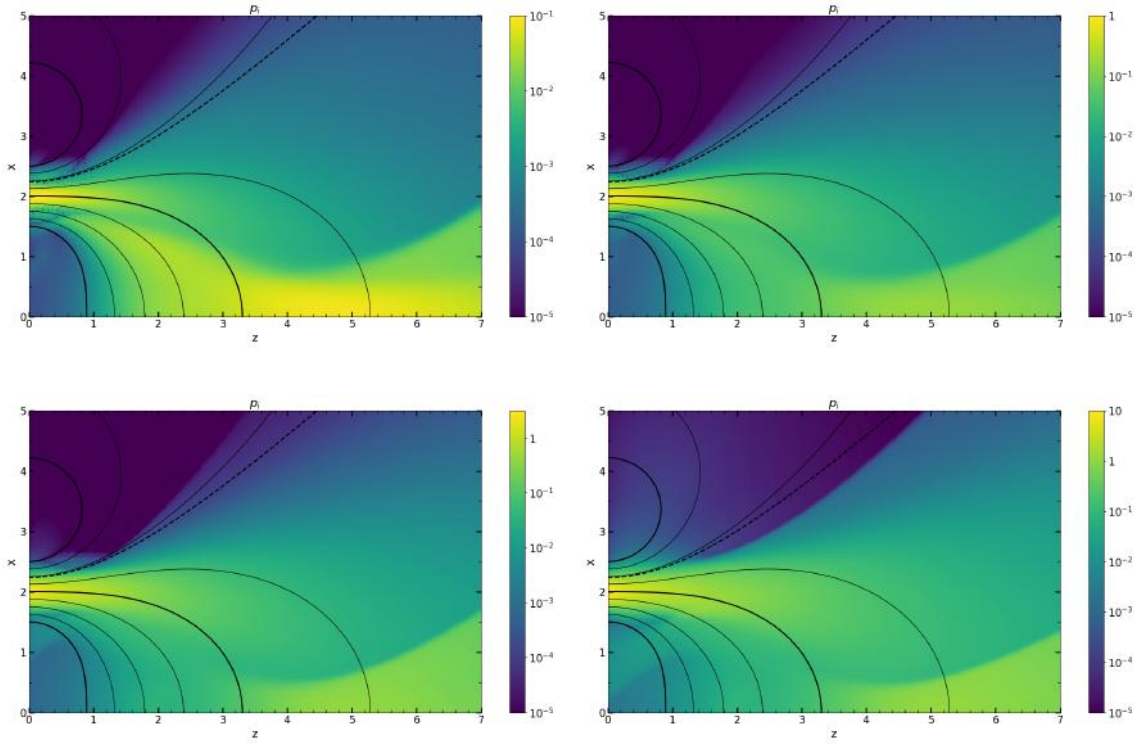

Fig. 5.4. Ion pressure distribution, $p_i = nT_i$. Respectively for $F_{T_0} = 0.1$ (a), $F_{T_0} = 1$ (b), $F_{T_0} = 3$ (c), $F_{T_0} = 10$ (d).

along regions where no shock structure is crossed. From the computational simulation standpoint, working at higher inlet temperatures results in an increase of solution precision, with lower T_{i0} introducing overshoot in the system (i.e. Fig. 5.5 (a) for T_{i0}=0.1). This numerical inconsistency originates from flux setup at ghost-cells and intrinsic Local Lax-Friedrich dissipation. The commented phenomena could be mitigated by introducing direct boundary condition imposition in future work.

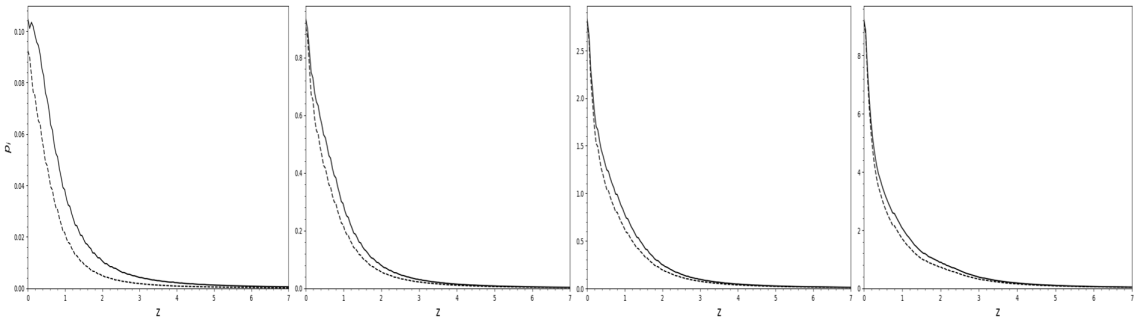

Fig. 5.5. Ion pressure downstream evolution (computed from $\hat{E}_i$ solution), depicted by solid black line, and curve for polytropic relation $p_i = n^{\gamma_i}$, depicted by dashed black line. Both displayed along the horizontal straight line starting from $x = C_t$. Respectively for $F_{T_0} = 0.1$ (a), $F_{T_0} = 1$ (b), $F_{T_0} = 3$ (c), $F_{T_0} = 10$ (d).

In order to complete the study, let us analyze the thrust resultant values for each of

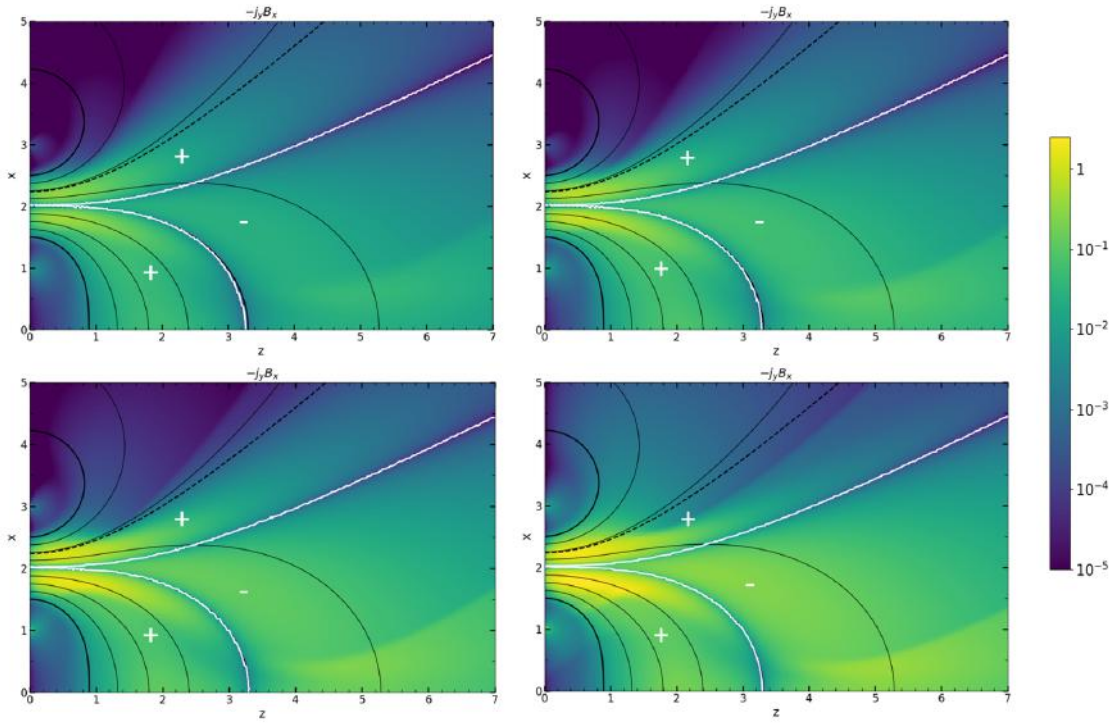

Fig. 5.6. Axial magnetic force $F_z = -j_yB_x$ generated by ion and electron azimuthal currents for $F_{T_0} = 0.1$ (a), $F_{T_0} = 1$ (b), $F_{T_0} = 3$ (c), $F_{T_0} = 10$ (d).

the given initial ion temperature profiles. Needless to mention that the axial magnetic force, defined as $F_{z,B} = -j_yB_x$, presents a considerable increase over its peak values due to the notable enlargement of u_{ye}, as depicted in Fig. 5.6. Collimation of the flow, however, concentrates these forces, reducing the effective z-directed F_v, slightly affecting peak values. Additionally, larger negative $F_{z,B}$ contribution arising downstream, enhanced by the oblique shock structure, does not experience this collapsing effect and its increasing values pose an issue for thrust development.

From a strictly thermodynamic and energy conversion perspective, when the ion temperature increases, a greater fraction of the energy is stored in thermal energy rather than being fully converted into the ordered, axial momentum of the plume. Consequently, even if the ions are accelerated to higher thermal speeds, if the energy is not efficiently directed, the overall thrust and, hence, efficiency are compromised.

Each of the represented curves in Fig. 5.7 correspond to the normalized thrust for a particular ion temperature condition, and show no major differences in the initial near the nozzle region, with the characteristic rapid thrust increase and a plateau section around $z \approx 3$. This plateau would indeed be the asymptotic effective thrust in a typical single nozzle system, but in the case for the MA this is later reduced from the oblique shock, where negative axial force is relevant. It is at this magnetic drag dominated region where ion temperature highly affects the final generated thrust, with an increase in thermal energy leading to insufficient resulting thrust. From the aforementioned figure, a conclusion arises: an increase in the initial ion temperature profile enlarges magnetic drag down-

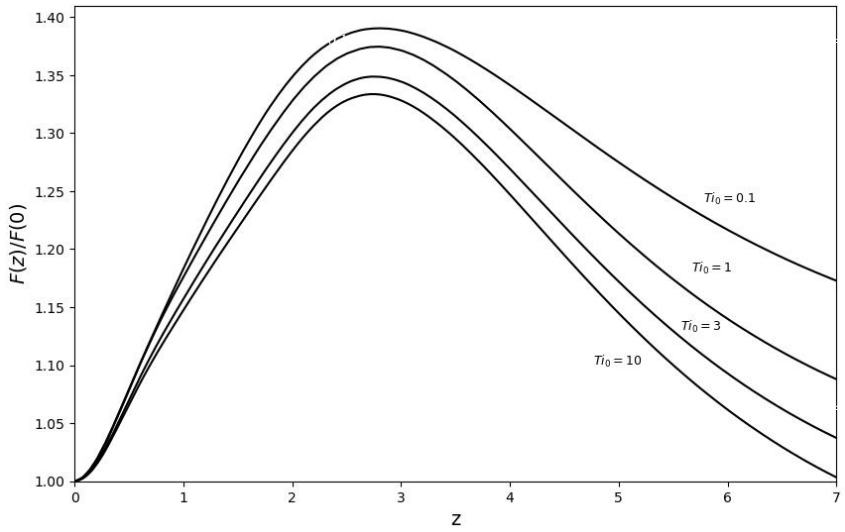

Fig. 5.7. Normalized generated thrust $F(z)/F(0)$ for the T_{i0} cases indicated adjacent to the curves.

stream, working against the generated thrust and causing a reduction in net efficiency. In fact, for $T_{i0} = 3$ and $T_{i0} = 10$ the device is not able to provide significant additional thrust from that outputted at the throat.

Take into consideration that Fig. 5.7 simply shows the normalized thrust values for a control domain defined by some z-coordinate. The effective thrust would be given by the asymptotic value of $F(z)/F(0)$ found at $z \to \infty$, thus being lower than that given at z_F. For $T_{i0} = 3, 10$, it may be approximated that $[F(z)/F(0)]_{z\to\infty} \to F(0)$.

Typically, a low-divergence angle beam is desired for efficient momentum transfer. Nevertheless, it is observed that high-temperature conditions under the effect of a highly confining ambipolar electric field do result in lower plume divergence angles, suggesting a more concentrated beam. However, this improvement in flow geometry is offset by the fact that increased thermal energy enhances magnetic drag, due to elevated negative z-directed force values originating at the downstream shock structure. This conclued that there is a trade-off between achieving a narrow plume and maintaining high net thrust output. High temperatures under imposed ambipolar potential confinement adversely influence the energy balance by augmenting drag mechanisms.

6. MAGNETIC FIELD GENERATORS ANALYSIS ON MA EXPANSION

As commented on Chapter 1, diverse magnetic field topologies may be achieved depending on the positioning of field generators, which would lead to one of the three geometries described: fully-closed MA, open-closed MA and fully-open expansion. Magnetic coils geometry and consequent situation of the streamfunction separatrix highly influences the applied magnetic field and, thus, the plasma expansion downstream.

The present Chapter is devoted to studying four cases of wire positioning that result in differentiated magnetic field topologies to evaluate an optimal configuration that results in higher beam-collimation, effective thrust and efficiency.

6.1. Description of the Simulation and Boundary Conditions

Setup and domain dimensions of the simulation are similar to those made use of in Chapter 5; with R_w, L_{w1} and L_{w2} being the parametric variables. Unless otherwise specified, the geometry of the thuster's throat is concentric to coil positioning. In other words, the center of the magnetic generator coincides with the center of the plasma source thruster, $C_w = C_t = 2, -2$. This condition implies that the MA topology arises (i.e. the centers of each of the thruster's throats are connected via magnetic streamtubes), either as fully-closed (*closed MA*) or semi-closed configurations (*open MA*). When fixing the center point of magnetic generators, a convenient variable describing the diameter of the coil arises, defined as $d_w = L_{w2} - L_{w1}$.

TABLE 6.1. SIMULATION CASES GEOMETRIC SETUP

	Magnetic Field Generators			**Thruster Outlet**		
	L_{w1}	L_{w2}	d_w	L_{t1}	L_{t2}	R_t
Case 1	x = 1.5,-1.5	x = 2.5, -2.5	1	x = 1.5, -1.5	x = 2.5, -2.5	0.5
Case 2	x = 0.5, -0.5	x = 3.5, -3.5	3	x = 1.5, -1.5	x = 2.5, -2.5	0.5

Table 6.1 displays the cases for which the simulation is performed, detailing the specific geometric characteristics. Case 1 corresponds to an open MA with separatrix falling between thruster edges, with open streamtubes rapidly diverging due to the low diameter d_w set of coils. Case 2 results in a closed MA, with separatrix positioned at $x = 2.5$, overlapped with the edge streamtube.

Regarding boundary conditions, density n, velocity vector $\mathbf{u_j}$ of each of the species, ion energy $\hat{E}_i$ (by defining a convenient T_i profile), and electric potential ϕ, shall be defined according to Eqs. 5.1-5.4. Specifically for ion temperature in Eq. 5.3, a factor

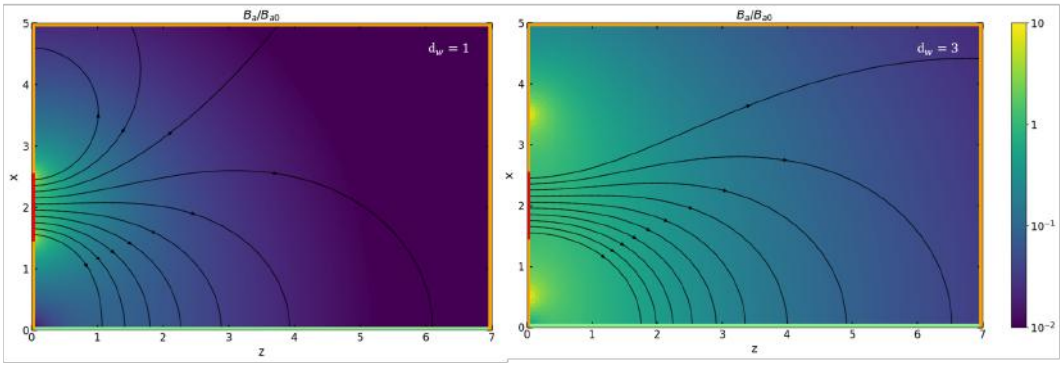

Fig. 6.1. Magnetic field distribution B/B_{a0} for $d_w = 1$ (open MA configuration) and $d_w = 3$ (closed MA configuration).

$F_{T0} = T_{i0} = 0.1$ is opted for. Thus, ion thermal energy is considered to be smaller than electron one by a factor of 10, falling under the cold-ion assumption, $T_i \ll T_e$.

6.2. Results and Discussion

To begin the study on magnetic generators configuration, a fundamental variable is the initial positioning of the magnetic field separatrix line, where $\psi_B = 0$, that is $x_{\psi=0}$. As commented, this determines whether the field topology is that of an open or closed MA. Fig. 6.2(a) depicts the separatrix line positioning for diverse d_w conditions, when maintaining the thruster's throat fixed at $C_t = 2$. It may be observed that $d_w = 3$ sets the limit for which the separatrix $x_{\psi=0}$ falls just above the magnetic thrusters upper edge, thus conforming the first possible closed MA. For $d_w \geq 3$, all configurations will be dominated by closed magnetic streamtubes, each with narrower curves connecting the coupled thrusters.

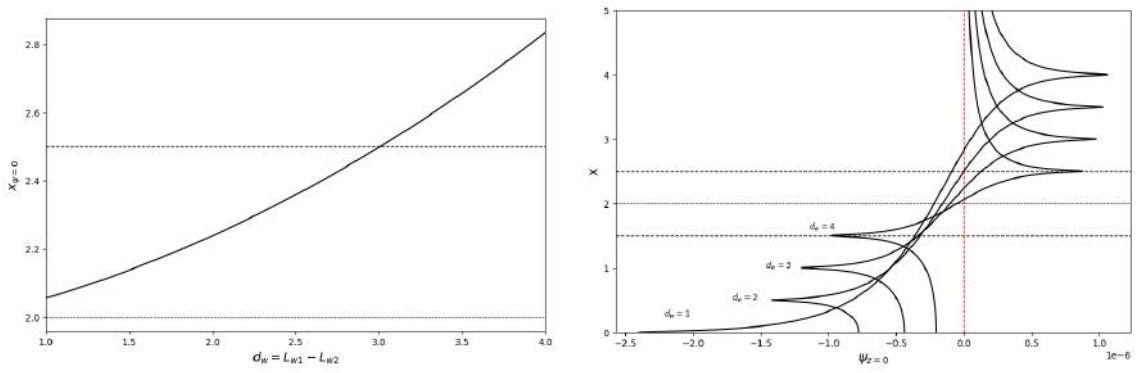

Fig. 6.2. Separatrix positioning ($x_{\psi=0}$) as a function of $d_w = L_{w1} - L_{w2}$ (a) and boundary magnetic streamfunction profile for selected $d_w = 1, 2, 3, 4$ (b). Black dashed lines represent center and edges of the plasma thruster. Red dashed line corresponds to the limit $\psi_B = 0$

Fig. 6.2(b) corroborates the commented phenomena for selected d_w cases, where

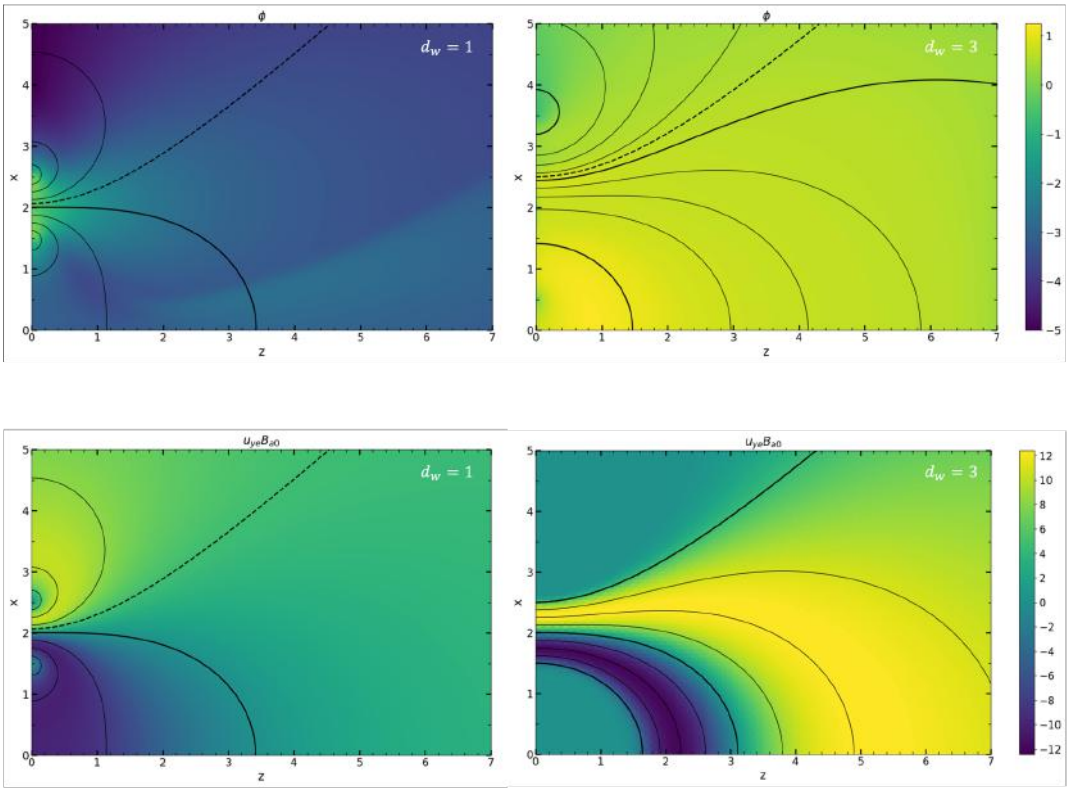

Fig. 6.3. Dimensionless ambipolar electric field ϕ (a) and out-of-plane electron velocity u_{ye} (b) for $d_w = 1$ and $d_w = 3$. Separatrix is represented by dashed streamtube and falls over the edge of the thruster magnetic line for $d_w = 3$.

boundary ψ_B profile is plotted. For $d_w = 1, 2$, $\psi_{z=0} = 0$ is found to fall inside the limits of the thruster edges, indicating that the separatrix falls within it and part of the magnetic streamtubes expand to infinity, as those in a MN.

Continuing with simulation results, Fig. 6.3 displays ϕ and u_{ye} for $d_w = 1$ and $d_w = 3$. Both properties give us an insight on plasma downstream acceleration and detachment. For the case in which $d_w = 1$ ϕ decays to lower negative values, both axially and radially, similarly to the conventional case in Chapter 5 for $T_{i0} = 0.1$, indicating a progressive jet acceleration as electronthermal energy is transferred to direct kinetic energy of the ions. However, on the other side, for a larger coil amplitude, ϕ appears to approximate a constant behavior, from which may be inferred that electrothermal energy is not sufficient to accelerate ions towards infinity, or at least not to attainable values in open MA models.

The map of u_{ye}, on the other hand, offers a good representation of confinement and detachment mechanisms. For $d_w = 1$, out-of-plane electron velocity and thus electromagnetic forces concentrate over the near expansion region, exerting higher forces over curved streamtubes to guide ions along these. This results in a delay on ion inward separation and, hence, an increase over the divergence of the plume. When the magnetic generators are separated and separatrix falls outside thruster limits, that is $d_w = 3$, stream-

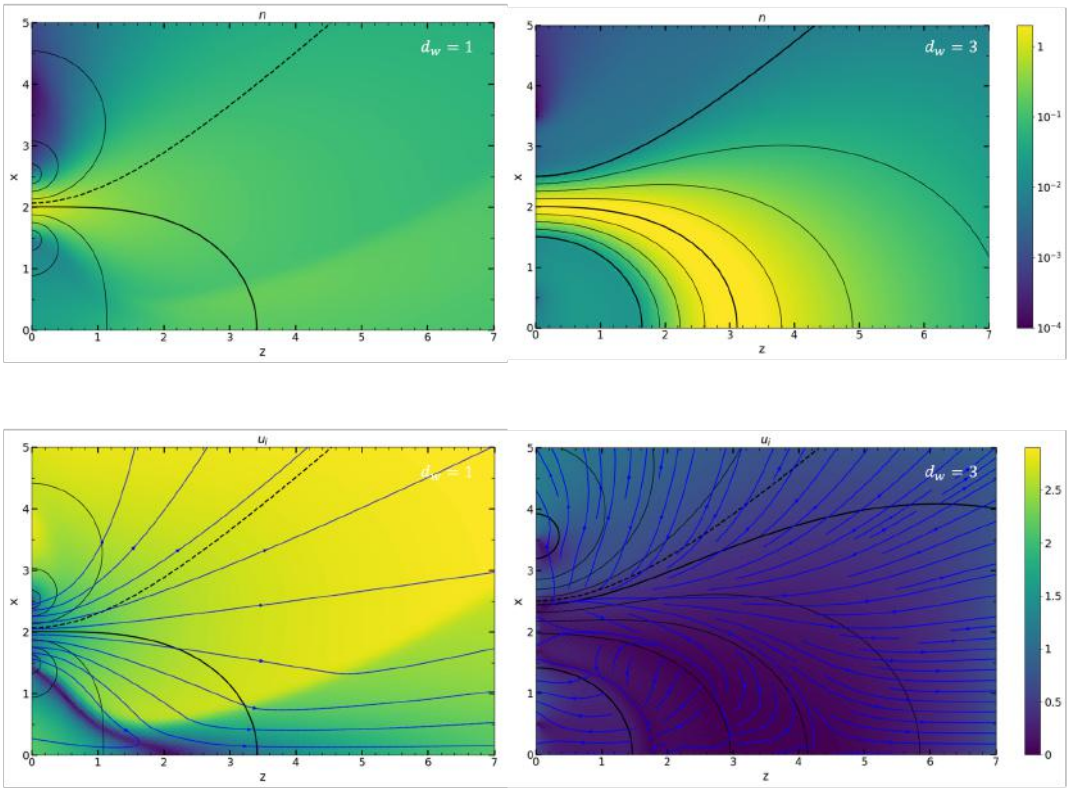

Fig. 6.4. Dimensionless plasma density n (a)-(b) and in-plane macroscopic flow ion velocity u_i (c)-(d) for $d_w = 1$ and $d_w = 3$. Ion streamlines are depicted in blue arrowed lines.

tubes close and guide electron trajectories on a more collimated beam. This implies that the electromagnetic forces increase and develop more concentrated over the inner closed streamlines of the field. This phenomena indicates that ion trajectories are expected to follow this lines, curving to the symmetry plane under the guidance of strongly concentrated magnetic forces.

Continuing with ion density n and in-plane velocity u_i, depicted in Fig. 6.4, the aforementioned phenomena is corroborated by downstream evolution. The case for which $d_w = 1$ constitutes a large-divergence plume expansion where electromagnetic forces manage to curve ion streamlines towards magnetic line direction. It may then be concluded that reduction in d_w, that is closing the current coil near the thruster, enlarges flow divergence.

Behavior of $d_w = 3$, however, develops a physically complex structure. Larger electromagnetic forces and collimated magnetic streamtubes manage to compensate the expanding pressure gradients downstream, confining the plasma jet to the direction of the magnetic lines. This phenomena directs the ejected jet perpendicularly against the symmetry plane. The encounter of the two clustered jets over this plane stagnates the plasma, generating a complex structure that advances towards the throat, guided by magnetic lines. This not only decelerates the plasma expansion but concentrates a larger plasma density

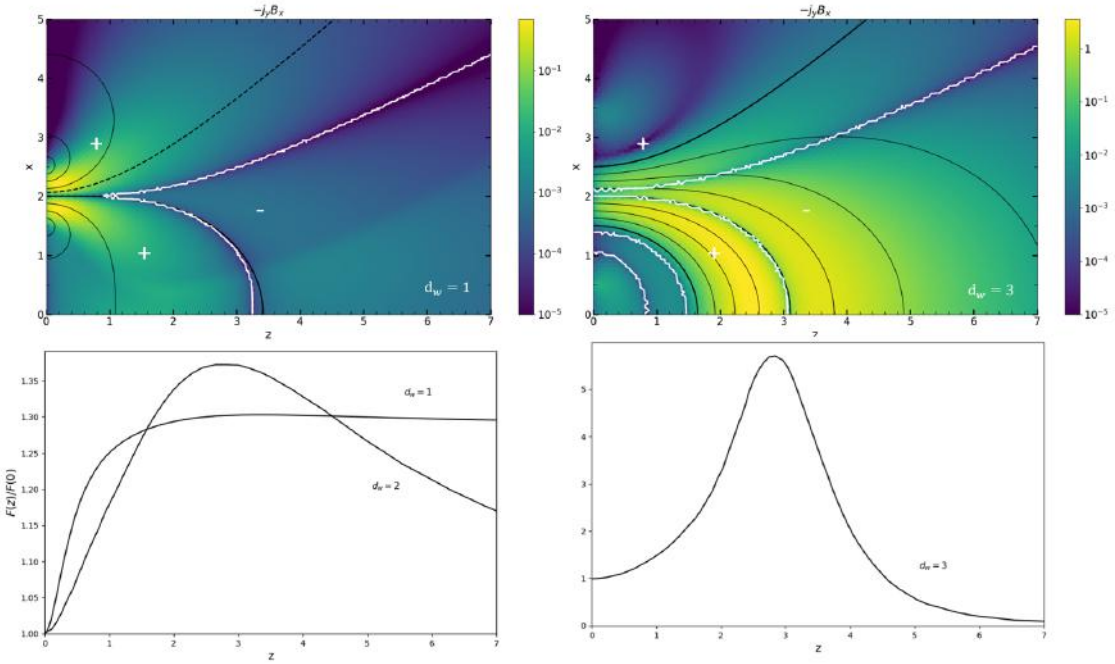

Fig. 6.5. Dimensionless z-directed electromagnetic force, $F_z = -j_y B_x$ for $d_w = 1$ and $d_w = 3$, (a) and (b). Thrust distribution $F(z)/F(0)$ for $d_w = 1$ and $d_w = 3$, (c) and (d).

along the closed magnetic tubes. A physical interpretation of this phenomena is that ion streamlines carrying the bulk of the plasma density do not manage to scape the closed MA, but instead stagnate. It is expected that for even wider current coils, plasma confinement would result even more effective, limiting plasma from expanding downstream.

Additionally, ions that do manage to scape the electromagnetic confinement show reduced flow velocity values when compared to lower d_w magnetic arch configurations.

An important note regarding $d_w = 3$ simulation for the closed MA is the impossibility of modeling in-plane electron current, $\mathbf{u}_{\|e}$. In previous simulations $\mathbf{u}_{\|e}$ was computed *a posteriori* from Eq. 2.25 to maintain global current free plasma over the domain, following the condition given in Eq. 4.6. Nevertheless, for the closed magnetic arch configuration, no magnetic streamtubes presenting $\psi_B > 0$ exist, thus current-free condition can not be imposed. As this is computed *a posteriori*, no alterations of the presented results are expected, but further sophistication in the model is required to model $\mathbf{u}_{\|e}$. A considered possibility is to introduce collisions, which would allow electron flows to encounter in the symmetry plane, allowing for physical interaction between particles and deflecting their trajectories from magnetic lines.

To end with the current analysis, z-directed force and normalized thrust are depicted in Fig. 6.5. It is noticeable that a larger F_z arises in the closed MA configuration, tough the major negative component negatively affects the performance of the thruster, originating adverse magnetic drag and making the device ineffective. The initial thrust concentration

in closed MA comes, mainly, from out-of-plane electron current development in the innermost region connecting the clustered throats. This then drops due to opposite directed electron currents developing along the closed magnetic streamlines as the flow advances downstream.

When comparing thrust levels of diverse open MA configurations, it appears that narrower magnetic generators, that is $< d_w$, result in higher effective thrust levels, minimizing magnetic drag formation.

7. FUTURE WORK AND CONCLUSION

7.1. Future Outlook

The presented study provides significant insights into ion thermodynamics and magnetic nozzle topology for a magnetic arch. Nevertheless, several key areas remain open for additional research and model sophistication.

1. **Actual 3D MA Model**. The 2D model applicability to describe the MA behavior requires confirmation from a fully dimensional simulation. While it is expected that a planar model accurately represents the physical evolution of the thruster, there are key variables or magnitudes that are being approximated or directly neglected. This is the case of an out of plane magnetic field strength B_y, which could have additional effects over dynamics due to the development of a new $E \times B$ drift contribution [6].

   The lateral B_y inclusion would also activate ion flux in the out-of-plane direction, which has been assumed to be negligible in the present work due to mild ion magnetization strength. This ion current j_{yi} could have a major impact in the expansion, resulting in a plume with rapidly decaying density and ambipolar electric potential [52].

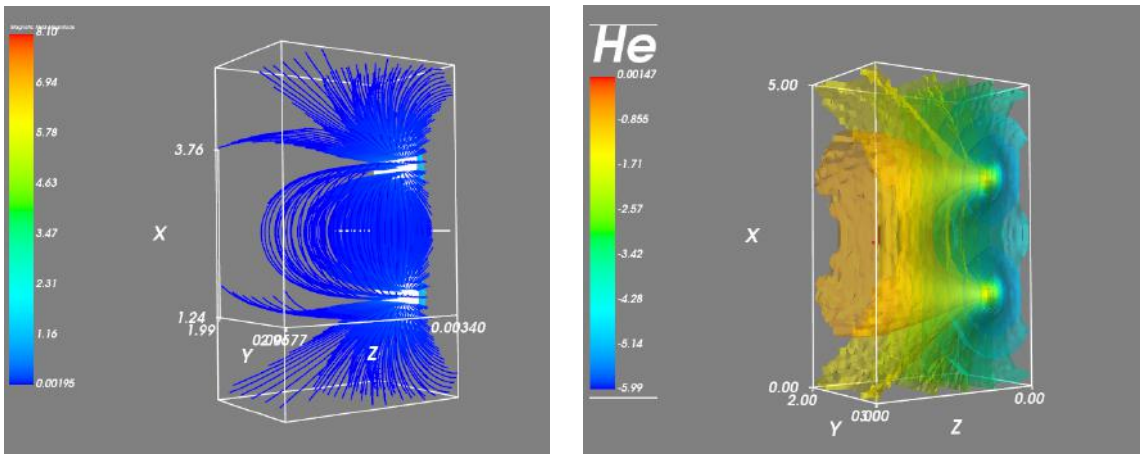

Fig. 7.1. Magnetic Field Strength B and Electron Thermal Function H_e in 3D Model for a MA from POSETS-v2.

   POSETS-v2 incorporates a 3D simulation functionality, which enables the computation and representation of the MA 3D magnetic field topology and the *apriori* computed parameters, particularly, the electron thermal function H_e and the azimuthal out-of-plane electron velocity u_ye. Results for density, ambipolar potential and velocity are yet under analysis, and further updates are yet to be expected.

2. **Ion and Electron Collisions**. Current simulation treats plasma as a two species collisionless fluid, neglecting neutral population. A proposed next step is to incorporate full ion-electron collision operators, together with neutral fluid components. By simulating charge-exchange, electron impact and ionization, a more accurate prediction of the downstream flow will be achieved.

   A fundamental result of non-zero collisions is the addition of a perpendicular in-plane electron flux $u_{\perp e}$, not present in 2D simulations where electrons where essentially guided by magnetic streamtubes. Collisions would make these species slightly deviate from the imposed trajectories and scape from magnetic confinement.

3. **Magnetic Arch Thruster Modeling**. The presented study models the expansion region under a MA applied magnetic field. This could be either generated by a clustered pair of EPTs or by a MAT. Further research projects should investigate the viability of the plasma flow advance inside a MAT, under the effect of an applied magnetic field curving parallel to the thruster's walls. Additionally, this would require of the implementation of a new boundary condition at the MAT walls. Fig. 7.2 displays the applied magnetic field inside a MAT and its expansion region.

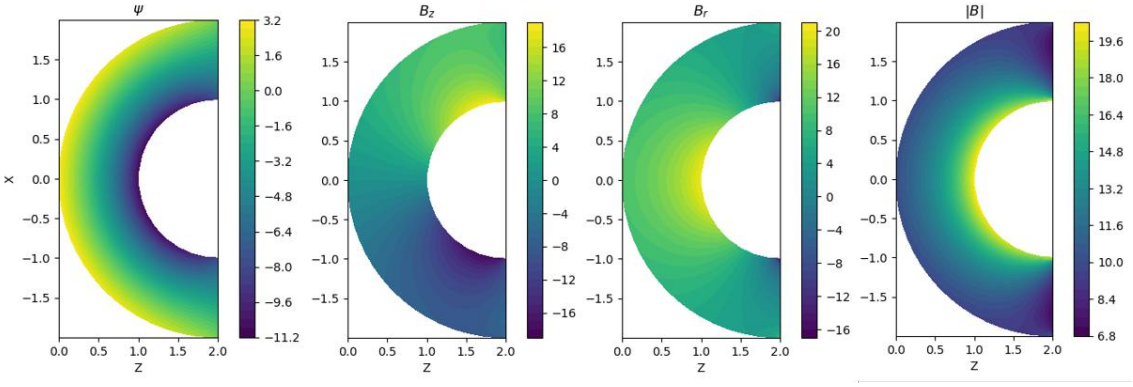

Fig. 7.2. Streamfunction ψ (a) and applied magnetic field in the internal section of the MAT (axial (b), radial (c) and total (d)).

4. **Electron Thermodynamics**. Finally, the validity of the electron quasi-Maxwellian distribution needs to be corroborated against experimental simulations for the case of MA. Although the assumption of the closure relation $T_e = T_{e0} n^{\gamma_e - 1}$ seems reasonable, this highly influences the map of H_e, $u_y e$ and ϕ, which are determinant for magnetic forces on both species of the plasma fluid and, hence, for the detachment and acceleration mechanisms.

   The electron model should also be revisited to include considerations that could be highly influential to the downstream expansion, among these: inertia effects, finite Larmor radius effect and the assumption of quasineutrality [6].

7.2. Conclusions

This project aims to deepen the theoretical comprehension of Electrodeless Plasma Thrusters (EPTs) operating under a Magnetic Arch (MA) magnetic field configuration, with special consideration of ion thermodynamics and magnetic generators geometry. The main conclusions and physical insight gathered is grouped in four main research areas: introduction of ion thermodynamics for cold-ion model approximation, analysis of electron cooling rate, non-negligible ion thermal energy conditions and magnetic coil variable radius study.

Firstly, by introducing direct conservation of ion total energy, governed by $\gamma_i = 5/3$ and $T_{i0} = 0.01$, the assumption under which ions are completely cold is eliminated, denoting a cooling process for this species. It is then proved that ions follow an isentropic cooling law $T_i \propto n^{\gamma_i - 1}$ along the downstream expansion, presenting discontinuities at regions where oblique shock structures originate. From ion thermodynamics, full discontinuity representation is achieved, and ion temperature experience sudden increase at at specific shock regions. This local energy transfer is simulated in this work, updating previous literature on the field [6]. With a global error <2% on energy conservation, POSETS-v2 is constituted as a viable tool to evaluate fluid evolution under thermodynamic considerations.

Secondly, the analysis for $\gamma_e = 1.01, 1.2, 5/3$ reveals that minor alterations in the polytropic electron index highly influence downstream evolution, altering axial acceleration and thrust profile. Under a nearly isothermal model, positive electromagnetic forces expand towards the far-expansion region, thus mitigating magnetic drag with a larger plume divergence. In contrast, for a nearly adiabatic model, magnetic drag is aggravated after the shock's formation, indicating the necessity of γ_e optimization under certain collimation and specific impulse conditions.

Thirdly, for non negligible initial temperature conditions, that is $T_{i0} = 0.1, 1, 3, 10$ a clear additional acceleration is experienced as thermal ion energy is transferred to direct kinetic energy. Under radial force balance at the throat via ambipolar electric potential imposition, the plasma beam experiences further collimation downstream, which reduces peak thrust levels up to a 7% and magnetic drag at $T_{i0} = 10$ invalidate thrust generation capabilities of the device.

Lastly, simulations with diverse coil diameter d_w indicate that for narrower magnetic generators divergence is accentuated but magnetic drag and the oblique's shock expansion is mitigated. Resulting in final effective thrust being larger than that achieved for wider coils in open-MA topologies. The case for closed-MA is characterized by the formation of a complex structure along the centerline connecting both EPTs. As the plasma flow clashes at the symmetry plane, the beam is decelerated and ions and electrons are accumulate, thus reducing velocity but increasing density. Little plasma flow is able to scape the confinement of the closed magnetic arch. This presents a major detrimental effect over

thrust generation capabilities.

In conclusion, this project overviews the physical mechanisms and complexity of electrodeless plasma thrusters, aiming to determine optimal thermodynamic and geometric configurations via numerical fluid analysis and the development of the POSETS-v2 framework. The presented results serve as a solid base for future experimental validation and industrial optimization of EPTs.

8. LEGAL FRAMEWORK AND SOCIO-ECONOMIC IMPACT

8.1. Legal Framework

The presented project includes diverse areas of research and industry: space propulsion, software development and potential industrial application. Thus, an analysis of standards and legal obligations needs to be performed, to asses the viability and validity of the research development.

As the project is theoretical, based on mathematical and physical models, indications on experiment and laboratory set-ups is not required. Hence, it is not restricted to the regulatory framework that prevents from hazards or risks in the EPTs test bench. For reference, RD 299/2016 regarding exposition to electromagnetic fields should be thoroughly examined if experimental procedures were to take place.

This work is also subject to ethical considerations. At the current state of the presented technologies, the model is not reproducible for warfare use and working prototype has not yet been designed. Nevertheless, future work may fall under the Ethical Code for Engineers.

Legal framework under which the project falls is that of intellectual and industrial property, mainly:

- **Article 32 of Law 1/1996, April 12 - Spanish Intellectual Property Law** [53]. According to the limitations and standards gathered in this article, all information included in the present work has been cited and credited adequately.
- **Law 38/2003, November 17 - General Subsidies** [54]. The project has been conducted with the financial support of the Collaboration Scholarship of the Ministry of Education. Thus, the regulatory framework of the scholarship directly influences that of the project. In conformity with what expressed in the law, the presented pr.0ºoject and work conducted has been carried out during the required Scholarship hours and those of the 12 ECTS of the Bachelor Thesis.

As an additional note, if the code was intended for industrial use, it complies with the ECSS-Q-ST-80C *Product Assurance Software*, which ensures adequate procedures for requirement management, V&V and configuration control of the POSETS-v2 code.

8.2. Socio-Economic Impact

The development of Electrodeless Plasma Thrusters (EPTs) could highly impact the space transportation and exploration sectors. Thus, the presented project serves as a model

prelude of what is to come. In order to design a working prototype for MA configuration, previous physical analysis needs to be performed. The updates included in POSETS-v2 provides the EP2 Research Group in UC3M with a powerful modeling tool that will result in major optimizations of magnetic nozzles.

From a research perspective, this project provides an unprecedented model with improvements that previous work did not include. The use of numerical solvers considerably reduces the economic impact of experimental procedures. The existence of POSETS-v2 reduces the necessary experimental iterations to attain optimal results, which can range up to 10k$-30k$ per session. And hence, it eases the accessibility of minor research groups or individuals that are willing to research on electromagnetic propulsion.

On a general basis, EPTs devices operate with noble gases (Xe or Ar) or virtually any gas, eliminating toxic components such as hydrazine and CO_2 associated to chemical rocket thrusters. This diminishes the carbon footprint being left behind by the space sector. It contributes to the Sustainable Development Goals ODS 9 and 13 [55], and towards mitigation of the space debris issue.

8.2.1. Project Budget

The estimated budget for the presented project is outlined in Table 8.1, specifying equipment and human resources costs, which sum up o a total of 12361.35€. An 15% overhead has been included to the final value, in agreement to the 2019 Governing Council Agreement of UC3M regarding research projects [56]

TABLE 8.1. PROJECT COSTS (VAT INCLUDED)

Software and Equipment	***Price per Unit (€)***	***Num. Units***	***Total Cost***
Software and GitHub Services	0	1	0
MSI GS 75 Stealth 95D (Computer)	1349.00	1	1349.00
Human Resources	***Salary (€/h)***	***Total Hours***	***Total Cost (€)***
Project Coordinator	35.00	40	1400.00
Undergraduate Researcher	10.00	800	8000.00[a]
Subtotal (VAT 21% included)			10749.00
Overhead (15% Total)			1612.35
TOTAL			**12361.35**

[a] Accounting for 300 hours corresponding to the 12 ECTS Bachelor Thesis and 500 hours corresponding to a Collaboration Scholarship [57] issued by the Spanish Ministry of Education at University Carlos III de Madrid

BIBLIOGRAPHY

[1] E. Ahedo, "Plasmas for space propulsion," *Plasma Phys. Control. Fusion*, vol. 53, 2011. DOI: 10.1088/0741-3335/53/12/124037.

[2] K. Takahashi, "Helicon-type radiofrequency plasma thrusters and magnetic plasma nozzles," *Reviews of Modern Plasma Physics*, vol. 3, no. 3, 2019. DOI: 10.1007/s41614-019-0024-2.

[3] S. Mazouffre, "Electric propulsion for satellites and spacecraft: Established technologies and novel approaches," *Plasma Sources Science and Technology*, vol. 25, 2016. DOI: 10.1088/0963-0252/25/3/033002.

[4] S. N. Bathgate, M. M. M. Bilek, and D. R. Mckenzie, "Electrodeless plasma thrusters for spacecraft: A review," *Plasma Science and Technology*, vol. 19, 2017. DOI: 10.1088/2058-6272/aa71fe.

[5] E. Ahedo and M. Merino, "Two-dimensional supersonic plasma acceleration in a magnetic nozzle," *Physics of Plasmas*, vol. 17, 2010. DOI: 10.1063/1.3442736.

[6] M. Merino, D. García-Lahuerta, and E. Ahedo, "Plasma acceleration in a magnetic arch," *Plasma Sources Science and Technology*, vol. 32, 2023. DOI: 10.1088/1361-6595/acd476.

[7] J. M. Little and E. Y. Choueiri, "Electron demagnetization in a magnetically expanding plasma," *Phys. Rev. Lett.*, vol. 123, 2019. DOI: 10.1103/PhysRevLett.123.145001.

[8] M. Merino and E. Ahedo, "Plasma detachment in a propulsive magnetic nozzle via ion demagnetization," *Plasma Sources Science and Technology*, vol. 23, no. 3, 2014. DOI: 10.1088/0963-0252/23/3/032001.

[9] M. Merino, "Analysis of magnetic nozzles for space plasma thrusters," PhD thesis, Universidad Politécnica de Madrid, Madrid, Jun. 2013.

[10] P. Jiménez, J. Zhou, J. Navarro, P. Fajardo, M. Merino, and E. Ahedo, "Analysis of a cusped helicon plasma thruster discharge," *Plasma Sources Science and Technology*, vol. 32, no. 10, 2023. DOI: 10.1088/1361-6595/ad01da.

[11] T. Ziemba, J. Carscadden, and J. Slough, "High power helicon thruster," *41st AIAA/ASME/SAE/ASEE Joint Propulsion Conference Exhibit*, 2005. DOI: 10.2514/6.2005-4119.

[12] J. Navarro-Cavallé, M. Wijnen, P. Fajardo, and E. Ahedo, "Experimental characterization of a 1 kw helicon plasma thruster," *Vacuum*, vol. 149, pp. 69–73, 2018. DOI: 10.1016/j.vacuum.2017.11.036.

[13] N. Souhair, M. Margarotto, F. Ponti, and D. Pavarin, "Analysis of the plasma transport in numerical simulations of helicon plasma thrusters," *AIP Advances*, vol. 11, 2021. DOI: 10.1063/5.0066221.

[14] F. Chang-Diaz, J. Squire, R. Bengtson, B. Breizman, M. Carter, and F. Baity, "The physics and engineering of the vasimr engine," *AIAA*, 2012. DOI: 10.2514/6.2000-3756.

[15] A. V. Arefiev and B. N. Breizman, "Theoretical components of the vasimr plasma propulsion concept," *Phys. Plasmas*, vol. 1, no. 5, 2004. DOI: 10.1063/1.1666328.

[16] T. W. Glover, F. R. C. Diaz, J. P. Squire, V. P. Jacobson, D. G. Chavers, and M. D. Carter, "Principal vasimr results and present objectives," *Space Technology and Applications International Forum*, vol. 746, no. 1, 2005. DOI: 10.1063/1.1867222.

[17] B. W. Longmier *et al.*, "Vx-200 magnetoplasma thruster performance results exceeding fifty-percent thruster efficiency," *Journal of Propulsion and Power*, vol. 27, no. 4, 2011. DOI: 10.2514/1.B34085.

[18] C. Boyé, J. Navarro-Cavallé, and M. Merino, "Ion current and energy in the magnetic arch of a cluster of two ecr plasma sources," *Journal of Electric Propulsion*, vol. 4, no. 10, 2025. DOI: 10.1007/s44205-025-00100-w.

[19] M. Merino, *Motor espacial de plasma sin electrodos con geometría en u*, pCT patent (Spanish Patent Office), Patent no. ES2733773, 2019.

[20] M. S. Alnaes *et al.*, "The fenics project version 1.5," *Archive of Numerical Software*, vol. 3, 2015. DOI: 10.11588/ans.2015.100.20553.

[21] M. Merino, J. Nuez, and E. Ahedo, "Fluid-kinetic model of a propulsive magnetic nozzle," *Plasma Sources Sci. Technol.*, vol. 30, 2021. DOI: 10.1088/1361-6595/ac2a0b.

[22] K. Takahashi, C. Charles, and R. W. Boswell, "Approaching the theoretical limit of diamagnetic-induced momentum in a rapidly diverging magnetic nozzle," *Phys. Rev. Lett.*, vol. 110, 2013. DOI: 10.1103/PhysRevLett.110.195003.

[23] M. Merino. "Erc zharathustra." (2021), [Online]. Available: https://erc-zarathustra.uc3m.es/.

[24] M. Merino, D. García-Lahuerta, C. Boyé, J. Navarro-Cavallé, and E. Ahedo, 37th Int. Electric Propulsion Conf. (Boston, MA:Electric Rocket Propulsion Society) p IEC-2022-423, 2022.

[25] M. Merino and E. Ahedo, "Effect of the plasma-induced magnetic field on a magnetic nozzle," *Plasma Sources Science and Technology*, vol. 25, no. 4, 2016. DOI: 10.1088/0963-0252/25/4/045012.

[26] M. Touati, R. Codur, F. Tsung, V. K. Decyk, W. B. Mori, and L. O. Silva, "Kinetic theory of particle-in-cell simulation plasma and the ensemble averaging technique," *Plasma Physics and Controlled Fusion*, vol. 64, 2022. DOI: 10.1088/1361-6587/ac9016.

[27] H. Takabe, *The Physics of Laser Plasmas and Applications - Volume 2* (Fluid Models and Atomic Physics of Plasmas). Springer, 2024.

[28] V. Rozhansky, *Plasma Theory* (An Advanced Guide for Graduate Students). Springer, 2023.

[29] F. Cichocki, M. Merino, and E. Ahedo, "Fluid vs pic modeling of a plasma plume expansion," *Joint Conference of 30th ISTS, 34th IEPC and 6th NSAT*, 2015.

[30] D. M. Goebel and I. Katz, *Fundamentals of Electric Propulsion: Ion and Hall Thrusters* (JPL Space Science and Technology Series). Jet Propulsion Laboratory, California Institute of Technology, 2008.

[31] E. Dennison, *Off-axis field of a current loop*, https://tiggerntatie.github.io/emagnet-py/offaxis/off_axis_loop.html, Accessed: 2025-05-23, 2018.

[32] M. J. Zucrow and J. D. Hoffman, *Gas Dynamics. Volume 2: Multidimensional Flow*. John Wiley and Sons, 1934.

[33] M. Merino and E. Ahedo, "Contactless steering of a plasma jet with a 3d magnetic nozzle," *Plasma Sources Science and Technology*, vol. 26, 2017. DOI: 10.1088/1361-6595/aa8061.

[34] B. W. Longmier *et al.*, "Ambipolar ion acceleration in an expanding magnetic nozzle," *Plasma Sources Science and Technology*, vol. 20, no. 1, 2010. DOI: 10.1088/0963-0252/20/1/015007.

[35] M. Merino and E. Ahedo, "Influence of electron and ion thermodynamics on the magnetic nozzle plasma expansion," *IEEE Transactions on Plasma Science*, vol. 43, no. 1, pp. 244–251, 2015. DOI: 10.1109/TPS.2014.2316020.

[36] A. E. Dubinov, "On a widespread inaccuracy in defining the mach number of solitons in a plasma," *Plasma Physics Reports*, vol. 35, no. 11, pp. 991–993, 2009. DOI: 10.1134/S1063780X09110105.

[37] E. Saberian, "The generalized ion-sound speed in space and astrophysical plasmas," *The Astrophysical Journal*, vol. 887, no. 2, 2019. DOI: 10.3847/1538-4357/ab5109.

[38] C. M. Dafermos, *Hyperbolic Conservation Laws in Continuum Physics* (A Series of Comprehensive Studies in Mathematics). Springer, 2016.

[39] R. Eymard, G. Thierry, and R. Herbin, "Finite volume method," *Scholarpedia*, vol. 5, Jan. 2010. DOI: 10.4249/scholarpedia.9835.

[40] R. Leveque, *Finite Volume Methods for Hyperbolic Problems*. Cambridge University Press, 2002.

[41] P. Houston and N. Sime, "Automatic symbolic computation for discontinuous galerkin finite element methods," *SIAM Journal on Scientific Computing*, vol. 40, no. 3, pp. C327–C357, 2018. DOI: 10.1137/17M1129751.

[42] R. Hartman and P. Houston, "Adaptive discontinuous galerkin finite element methods for the compressible euler equations," *Journal of Computational Physics*, vol. 183, no. 2, pp. 508–532, 2002. DOI: 10.1006/jcph.2002.7206.

[43] S. Markfelder, *Convex Integration Applied to the Multi-Dimensional Compressible Euler Equations* (Lecture Notes in Mathematics). Springer, 2021.

[44] M. Kronbichler and P. Persson, *Efficient High-Order Discretizations for Computational Fluid Dynamics*. Springer, 2021.

[45] B. Cockburn and C. Shu, "The runge–kutta discontinuous galerkin method for conservation laws v: Multidimensional systems," *Journal of Computational Physics*, vol. 141, no. 2, pp. 199–224, 1998. DOI: 10.1006/jcph.1998.5892.

[46] J. Y. Kim, K.-J. Chung, K. Takahashi, M. Merino, and E. Ahedo, "Kinetic electron cooling in magnetic nozzles: Experiments and modeling," *Plasma Sources Science and Technology*, vol. 32, 2023. DOI: 10.1088/1361-6595/acd71c.

[47] J. M. Little and E. Y. Choueiri, "Critical condition for plasma confinement in the source of a magnetic nozzle flow," *IEEE Transactions on Plasma Science*, vol. 43, no. 1, 2015. DOI: 10.1109/TPS.2014.2322522.

[48] C. S. Olsen, M. G. Ballenger, M. D. Carter, F. R. C. Díaz, M. Giambusso, and T. W. Glover, "Investigation of plasma detachment from a magnetic nozzle in the plume of the vx-200 magnetoplasma thruster," *IEEE Transactions on Plasma Science*, vol. 43, no. 1, pp. 252–268, 2015. DOI: 10.1109/TPS.2014.2321257.

[49] B. R. Roberson, R. Winglee, and J. Prager, "Enhanced diamagnetic perturbations and electric currents observed downstream of the high power helicon," *Phys. Plasmas*, vol. 18, no. 5, 2011. DOI: 10.1063/1.3574753.

[50] M. Martínez-Sánchez and E. Ahedo, "Magnetic mirror effects on a collisionless plasma in a convergent geometry," *Phys. Plasmas*, vol. 18, 2011. DOI: 10.1063/1.3554650.

[51] J. M. Little and E. Y. Choueiri, "Electron cooling in a magnetically expanding plasma," *Phys. Rev. Lett.*, vol. 117, 2016. DOI: 10.1103/PhysRevLett.117.225003.

[52] H. G. Kosmahl, "Three-dimensional plasma acceleration through axisymmetric diverging magnetic fields based on dipole moment approximation," *NASA Technical Note (TN)*, 1967.

[53] M. de Cultura. “Real decreto legislativo 1/1996, de 12 de abril, por el que se aprueba el texto refundido de la ley de propiedad intelectual, regularizando, aclarando y armonizando las disposiciones legales vigentes sobre la materia.” (1996), [Online]. Available: https://www.boe.es/eli/es/rdlg/1996/04/12/1/con.

[54] J. del Estado. “Ley 38/2003, de 17 de noviembre, general de subvenciones.” (2004), [Online]. Available: https://www.boe.es/eli/es/l/2003/11/17/38/con.

[55] D. of Economic and U. N. Social Affairs. “Sustainable development.” (2016), [Online]. Available: https://sdgs.un.org/goals.

[56] U. C. I. de Madrid. Consejo de Gobierno. “Publication: Acuerdo del consejo de gobierno sobre la distribución de las retenciones de los proyectos de investigación, aprobado por el consejo de gobierno en sesión de 24 de enero de 2019.” (2019), [Online]. Available: https://hdl.handle.net/10016/27961.

[57] F. P. y. D. Ministerio de Educación. “Becas de colaboración.” (2024), [Online]. Available: https://www.educacionfpydeportes.gob.es/servicios-al-ciudadano/catalogo/estudiantes/becas-ayudas/para-estudiar/universidad/grado/becas-colaboracion.html.

uc3m | Universidad Carlos III de Madrid

DECLARATION OF USE OF GENERATIVE IA IN BACHELOR THESIS (TFG)

I have used Generative AI in this work

Part 1: Reflection on ethical and responsible behaviour

Please be aware that the use of Generative AI carries some risks and may generate a series of consequences that affect the moral integrity of your performance with it. Therefore, we ask you to answer the following questions honestly (*please tick all that apply*):

Question		
1. In my interaction with Generative AI tools, I have submitted **sensitive data** with the consent of the data subjects.		
YES, I have used this data with permission	NO, I have used this data without authorisation	NO, I have not used sensitive data
2. In my interaction with Generative AI tools, I have submitted **copyrighted materials** with the permission of those concerned.		
YES, I have used these materials with permission	NO, I have used these materials without permission	NO, I have not used protected materials
3. In my interaction with Generative AI tools, I have submitted **personal data** with the consent of the data subjects.		
YES, I have used this data with permission	NO, I have used this data without authorisation	NO, I have not used personal data

4. My use of the Generative AI tool has **respected its terms of use**, as well as the essential ethical principles, not being maliciously oriented to obtain an inappropriate result for the work presented, that is to say, one that produces an impression or knowledge contrary to the reality of the results obtained, that supplants my own work or that could harm people.	
YES	NO

Part 2: Declaration of technical use

Use the following model statement as many times as necessary, in order to reflect all types of iteration you have had with Generative AI tools. Include one example for each type of use where indicated.

I declare that I have made use of the Generative AI system Copilot for Bibliography search.

Generative AI has been used as a support tool for the development of the specific content of the dissertation, including assistance in the development of lines of code (programming). Example: used for iterative and automatic procedures such as labeling plots or adding tick labels to graphs.

Part 3: Declaration of technical use

Please provide a personal assessment (free format) of the strengths and weaknesses you have identified in the use of Generative AI tools in the development of your work. Mention if it has helped you in the learning process, or in the development or drawing conclusions from your work.

It has eased some iterative or automatic procedures for code development. Additionally, it provides a powerful tool for reference lookout and bibliography gathering.